UNIVERSIDADE DE BRASÍLIA – UnB
INSTITUTO DE GEOCIÊNCIAS – IG
CURSO DE PÓS-GRADUAÇÃO EM GEOLOGIA

RELAÇÕES PETROGENÉTICAS ENTRE A SUÍTE GRANÍTICA AURUMINA E SUA ENCAIXANTE, A FORMAÇÃO TICUNZAL, NO SETOR SETENTRIONAL DA ZONA EXTERNA DA FAIXA BRASÍLIA

TESE DE DOUTORADO Nº136

FEDERICO ALBERTO CUADROS JIMÉNEZ

Brasília, DF, maio de 2017

UNIVERSIDADE DE BRASÍLIA – UnB
INSTITUTO DE GEOCIÊNCIAS – IG
CURSO DE PÓS-GRADUAÇÃO EM GEOLOGIA

RELAÇÕES PETROGENÉTICAS ENTRE A SUÍTE GRANÍTICA AURUMINA E SUA ENCAIXANTE, A FORMAÇÃO TICUNZAL, NO SETOR SETENTRIONAL DA ZONA EXTERNA DA FAIXA BRASÍLIA

Federico Alberto Cuadros Jiménez

Orientador:

Prof. Dr. Nilson Francisquini Botelho

Banca Examinadora:

Prof. Dr. Claudio de Morisson Valeriano (UERJ)

Prof. Dr. Johildo Salomão Figueirêdo Barbosa (UFBA)

Profa. Dra. Maria Emilia Schutesky Della Giustina (UnB)

Prof. Dr. Claudinei Gouveia de Oliveira (UnB)
(Suplente)

Brasília, DF, maio de 2017

RESUMO

Os granitos e tonalitos/granodioritos peraluminosos da Suíte Aurumina que afloram na zona externa da Faixa Brasília, na margem oeste do Cráton São Francisco, se encontram em contato intrusivo com xistos e paragnaisses da Formação Ticunzal. As rochas da suíte apresentam uma assembleia magmática constitutida por muscovita±biotita±granada, além de lamelas discretas de grafita. A suíte é dividida em cinco membros, denominados Au1, Au2, Au3, Au4 e Au6. Neste trabalho, as rochas pertencentes ao membro Au5, definido em trabalhos anteriores, não são consideradas como representantes de um evento magmático distinto e interpretam-se como relacionadas ao membro Au1 da suíte. As rochas da Suíte Aurumina possuem um caráter que varia entre sin-cinemático (com geração local de milonitos) e pós-cinemático, com idades de cristalização magmática entre 2.11 e 2.16 Ga inferidas mediante o método U-Pb em zircão usando a técnica MC-LA-ICP-MS. As feições composicionais da Suíte Aurumina e um grupo associado de rochas metaluminosas máficas a intermediárias contemporâneas sugerem uma origem por processos de hibridização de fonte caracterizados pela reação entre rochas metassedimentares e fundidos basálticos a pressões menores do que 5 kbar. Isto é apoiado por um intervalo restrito de valores de ε_{NdT} entre -4.2 e +0.4 obtidos tanto de amostras da Suíte Aurumina quanto das unidades metaluminosas associadas.

A Formação Ticunzal corresponde a uma sequência de rochas localmente milonitizadas constituida por biotita-granada paragneisses e mica-grafita xistos com assembleias minerais compostas por epidoto, clorita e mica branca que indicam um retrometamorfismo em fácies xisto verde. Idades de zircão detrítico obtidas mediante MC-LA-ICP-MS, idades modelo de Nd entre 2.23 e 2.88 Ga e dados de litogeoquímica sugerem uma proveniência para a Formação Ticunzal representada principalmente pelas rochas tonalíticas/granodioríticas com idades de 2.20 e 2.46 Ga do terreno Almas-Dianópolis, no sudeste do Tocantins. Tanto as idades obtidas em zircão detrítico quanto a relação intrusiva observada entre a Formação Ticunzal e a Suíte Aurumina permitem sugerir um intervalo de idade compreendido entre 2.16 e 2.19 Ga para a deposição dos sedimentos que deram origem à Formação Ticunzal. Análises de espectroscopia Raman em grafita indicam um alto grau de cristalinidade do mineral, consistente com temperaturas de pico metamórfico entre 620 e 630ºC.

As características geoquímicas e isotópicas mostradas pelas rochas peraluminosas da Suíte Aurumina sugerem que a Formação Ticunzal não atuou como fonte para seus magmas, embora as rochas da formação possam ter influenciado a suíte mediante processos de assimilação. Em seu lugar, uma das possíveis fontes para os magmas da Suíte Aurumina poderia corresponder à crosta antiga e retrabalhada que também deu origem às rochas magmáticas peraluminosas de 2.20 Ga do terreno Almas-Dianópolis, sendo também factível a participação de outras fontes desconhecidas.

Várias semelhanças composicionais, litologicas e de contexto tectonometamórfico são observadas entre o magmatismo peraluminoso da Suíte Aurumina e aquele da faixa granítica peraluminosa Jurássica-Paleôgena do interior cordilheirano da América do Norte, o que sugere um ambiente tectônico semelhante para a Suíte Aurumina em lugar do ambiente colisional sugerido em trabalhos anteriores. Adicionalmente, dados litogeoquímicos de elementos traço de amostras da Formação Ticunzal sugerem que seus sedimentos precursores foram depositados em uma bacia relacionada a um ambiente de arco continental, sendo isto consistente com o ambiente relacionado a arco inferido para a Suíte Aurumina neste trabalho, e o ambiente de arco proposto em outros trabalhos para as rochas tonalíticas-granodioríticas do terreno Almas-Dianópolis. Estes resultados evidenciam a existência de uma importante faixa móvel na borda oeste do Cráton São Francisco durante boa parte do Paleoproterozóico, a par das já conhecidas províncias Arqueanas-Paleoproterozóicas do cráton nos seus setores sul (região do Quadrilátero Ferrífero) e leste (região da Faixa Itabuna-Salvador-Curaçá e os blocos Gavião, Jequié e Serrinha).

Palavras chave: Cráton São Francisco; Faixa Brasília; Suíte Aurumina; Formação Ticunzal; magmatismo peraluminoso; interior cordilheirano; hibridização de fonte; proveniência sedimentar; termometria de grafita; evento isotópico Lomagundi-Jatuli.

ABSTRACT

The Aurumina Suite peraluminous granites and tonalites/granodiorites that are exposed in the external zone of the Brasília Fold Belt, western margin of the São Francisco Craton, intrude Ticunzal Formation schists and paragneisses. Rocks of this suite display magmatic muscovite±biotite±garnet assemblages and discrete graphite lamellae. The Aurumina Suite is divided into five members referred to as Au1, Au2, Au3, Au4 and Au6. In this work, rocks belonging to the Au5 member, which was defined in previous studies, are not considered representative of a distinct magmatic event and, instead, are considered as related to the Au1 member. The rocks of the Aurumina Suite vary from syn-kinematic (with local formation of mylonites) to post-kinematic in character, and yield zircon U-Pb MC-LA-ICP-MS magmatic crystallization ages between 2.11 and 2.16 Ga. Compositional features of the Aurumina Suite and associated metaluminous mafic to intermediate coeval rocks suggest a generation by source hybridization processes characterized by reaction between metasedimentary rocks and basaltic melts at pressures lower than 5 kbar. This is supported by ε_{NdT} values varying within a narrow interval between -4.2 and +0.4 for the Aurumina Suite and the metaluminous rock samples.

The Ticunzal Formation consists of a sequence of locally mylonitic biotite-garnet paragneisses and mica-graphite schists displaying epidote, chlorite and white mica assemblages indicative of retrograde metamorphism under greenschist facies conditions. Detrital zircon MC-LA-ICP-MS ages, Nd model ages between 2.23 and 2.88 Ga and geochemical data point out a Ticunzal Formation provenance consisting mainly of the 2.20 and 2.46 Ga tonalitic/granodioritic rocks exposed in the Almas-Dianópolis terrane, southeastern Tocantins. The detrital zircon ages and the intrusive relation with the Aurumina Suite lead to suggest a depositional age interval between 2.16 and 2.19 Ga for the Ticunzal Formation. Graphite Raman spectroscopy analyses point out a high degree of crystallinity for this mineral, which was attained upon metamorphic peak temperatures between 620 and 630ºC.

The geochemical and isotopic characteristics displayed by the Aurumina Suite peraluminous rocks suggest that the Ticunzal Formation was not the source of the magmas, although this formation might have actually been responsible for some modifications via assimilation processes. Instead, a possible source of the Aurumina Suite magmas would correspond to old reworked crust that could have also generated the 2.20

Ga peraluminous magmatic rocks found in the Almas-Dianópolis terrane, although participation of other unknown sources should not be ruled out.

A number of compositional, lithological and tectonometamorphic context similarities exist between the Aurumina Suite peraluminous magmatism and the Jurassic-Paleogene peraluminous granite belt from the North American cordilleran hinterland, which suggests a similar tectonic setting for the Aurumine Suite instead of the collisional setting proposed in previous works. Furthermore, Ticunzal Formation trace element geochemical data suggest that their precursor sediments were deposited in a continental arc-related basin, which is consistent with the arc-related setting inferred for the Aurumina Suite in this work, and the arc setting proposed in other works for the tonalitic-granodioritic rocks of the Almas-Dianópolis terrane. These results put in evidence the existence of an important mobile belt located at the western margin of the São Francisco Craton during a significative part of the Paleoproterozoic, adding to the already known Archean-Paleoproterozoic provinces in the southern (Quadrilátero Ferrífero region) and eastern (Itabuna-Salvador-Curaçá Belt and Gavião, Jequié and Serrinha blocks region) sectors of the craton.

Keywords: São Francisco Craton; Brasília Fold Belt; Aurumina Suite; Ticunzal Formation; peraluminous magmatism; cordilleran hinterland; source hybridization; sediment provenance; graphite thermometry; Lomagundi-Jatuli isotopic event.

RESUMEN

Los granitos y tonalitas/granodioritas peraluminosas de la Suite Aurumina que afloran en la zona externa de la Franja Brasília, sobre la margen occidental del Cratón São Francisco, se encuentran en contacto intrusivo con esquistos y paragneises de la Formación Ticunzal. Las rocas de la Suite Aurumina presentan una asamblea magmática constituída por moscovita±biotita±granate, además de láminas discretas de grafito. La suite se divide en cinco miembros, denominados Au1, Au2, Au3, Au4 y Au6. En este trabajo, las rocas pertenecientes al miembro Au5, definido en trabajos anteriores, no son consideradas como representantes de un evento magmático separado y son interpretadas como relacionadas al miembro Au1 de la suite. Las rocas de la Suite Aurumina poseen un carácter que varía entre sincinemático (con generación local de milonitas) e postcinemático, con edades de cristalización magmática entre 2.11 y 2.16 Ga obtenidas mediante el método U-Pb en circón, usando la técnica MC-LA-ICP-MS. Los aspectos composicionales de la Suite Aurumina y un grupo asociado de rocas metaluminosas máficas a intermedias contemporáneas sugieren un origen por procesos de hibridización de fuente caracterizados por la reacción entre rocas sedimentarias y fundidos basálticos a presiones menores de 5 kbar. Esto es apoyado por un estrecho intervalo de valores de ε_{NdT} entre -4.2 y +0.4 obtenidos tanto de muestras de la Suite Aurumina como de las unidades metaluminosas asociadas.

La Formación Ticunzal corresponde a una secuencia de rocas localmente milonitizadas constituída por paragneises de biotita y granate, y esquistos de mica y grafito con asambleas minerales compuestas por epidota, clorita y mica blanca que indican un metamorfismo retrógrado en facies esquisto verde. Edades de circón detrítico obtenidas mediante MC-LA-ICP-MS, edades modelo de Nd entre 2.23 y 2.88 Ga y datos de litogeoquímica indican una proveniencia para la Formación Ticunzal representada principalmente por las rocas tonalíticas/granodioríticas con edades de 2.20 y 2.46 Ga del terreno Almas-Dianópolis, sudeste de Tocantins. Tanto las edades obtenidas en circón detrítico como la relación intrusiva observada entre la Formación Ticunzal y la Suite Aurumina permiten sugerir un intervalo de edad comprendido entre 2.16 y 2.19 Ga para la depositación de los sedimentos que dieron origen a la Formación Ticunzal. Análisis de espectroscopia Raman en grafito indican un alto grado de cristalinidad del mineral, consistente con temperaturas de pico metamórfico entre 620 y 630ºC.

Las características geoquímicas e isotópicas mostradas por las rocas peraluminosas de la Suite Aurumina sugieren que la Formación Ticunzal no actuó como fuente para sus magmas, aunque las rocas de la formación sí podrían haber influenciado a la suite mediante procesos de asimilación. En lugar de eso, una de las posibles fuentes para los magmas de la Suite Aurumina podría corresponder a la corteza antigua y retrabajada que también dió origen a las rocas magmáticas peraluminosas de 2.20 Ga del terreno Almas-Dianópolis, siendo también factible la participación de otras fuentes desconocidas.

Varias semejanzas composicionales, litológicas y de contexto tectonometamórfico son observadas entre el magmatismo peraluminoso de la Suite Aurumina y aquel de la franja granítica peraluminosa Jurásica-Paleógena del interior cordillerano de Norteamérica, lo que sugiere un ambiente tectónico semejante al de este último para la Suite Aurumina en lugar del ambiente colisional sugerido en trabajos anteriores. Adicionalmente, datos litogeoquímicos de elementos traza de muestras de la Formación Ticunzal sugieren que sus sedimentos precursores fueron depositados en una cuenca relacionada a un ambiente de arco continental, siendo esto consistente con el ambiente relacionado a arco inferido para la Suite Aurumina en este trabajo, y el ambiente de arco propuesto en otros trabajos para las rocas tonalíticas/granodioríticas del terreno Almas-Dianópolis. Estos resultados evidencian la existencia de un importante cinturón móvil en la margen occidental del Cratón São Francisco durante buena parte del Paleoproterozoico, a la par de las ya conocidas provincias Arcaicas-Paleoproterozoicas del cratón en sus sectores sur (región del Cuadrilátero Ferrífero) y este (región de la franja Itabuna-Salvador-Curaçá y los bloques Gavião, Jequié y Serrinha).

Palabras clave: Cratón São Francisco; Franja Brasília; Suite Aurumina; Formación Ticunzal; magmatismo peraluminoso; interior cordillerano; hibridización de fuente; proveniencia sedimentaria; termometría de grafito; evento isotópico Lomagundi-Jatuli.

SUMÁRIO

ÍNDICE DE FIGURAS

ÍNDICE DE TABELAS

CAPÍTULO 1 - INTRODUÇÃO

1.1. JUSTIFICATIVA E OBJETIVOS DO TRABALHO

O presente trabalho tem como objetivo aprofundar o conhecimento geológico da parte setentrional da zona externa da Faixa Brasília, especificamente da porção sul do bloco de embassamento Paleoproterozóico localizado entre os municípios de Colinas do Sul (GO), Monte Alegre de Goiás (GO) e Natividade (TO). Esta região é conhecida pelas boas exposições das rochas graníticas e tonalitos agrupados na Suíte Aurumina (Botelho *et al.*, 1999; 2006a) e das suas rochas encaixantes metassedimentares pertencentes à Formação Ticunzal (Marini *et al.*, 1978; 1984b; Fernandes *et al.*, 1982). As dissertações e teses já existentes sobre estas unidades, embora realizadas com um bom nível de detalhe, foram restritas geográficamente ou têm se limitado a caracterizar alguns dos seus prospectos minerais associados (*e.g.*, Pereira, 2001; Cunha, 2006; Menez e Botelho, 2016; Bogossian, 2012). A abordagem adotada neste trabalho é geograficamente mais ampla e essencialmente geoquímica, geocronológica e isotópica, visando conseguir um melhor detalhamento do significado geológico e das relações entre as duas unidades mencionadas. Este conhecimento é vital não só para o entendimento da evolução geológica da região e a identificação do seu potencial em termos de recursos minerais, mas também para o refinamento e discussão dos modelos de evolução paleocontinental existentes, como apontado por Fuck *et al.* (2014).

Especificamente, os objetivos abordados neste trabalho foram:

- Determinar as possíveis rochas fonte que deram origem aos magmas da Suíte Aurumina, sendo que um dos aspectos mais importantes a ser considerado é a presença de um grande volume de tonalitos peraluminosos na suíte.

- Determinar a idade da Suíte Aurumina e o ambiente tectônico em que ela foi gerada.

- Determinar a idade e proveniência da Formação Ticunzal, e o ambiente tectônico da bacia em que ela foi depositada.

Os resultados obtidos em relação a estes objetivos são posteriormente discutidos em função do seu significado dentro do contexto das características da margem oeste do Cráton São Francisco durante o Paleoproterozóico.

1.2. LOCALIZAÇÃO E ACESSO

A área de estudo encontra-se localizada no planalto central brasileiro, nos setores nordeste do estado de Goiás e sudeste do estado de Tocantins (Fig. 1.1). O acesso desde Brasília pode ser conseguido inicialmente pela rodovia BR-020, para continuar posteriormente pela rodovia BR-010 até a cidade de Teresina de Goiás. A partir desta cidade, o acesso ao setor oeste da área de estudo é feito por meio da rodovia GO-241 até a cidade de Cavalcante e, posteriormente, pela estrada Cavalcante-Colinas do Sul. Alternativamente, o acesso na cidade de Colinas do Sul pode ser feito por meio da rodovia GO-239 desde a cidade de Alto Paraíso de Goiás, sobre a rodovia BR-010. Desde Teresina de Goiás, os setores centrais e norte da área de estudo podem ser acessados pela rodovia GO-118, passando pelas cidades de Monte Alegre de Goiás e Campos Belos, e posteriormente pela rodovia TO-050 passando pelas cidades de Arraias, Conceição do Tocantins e Natividade.

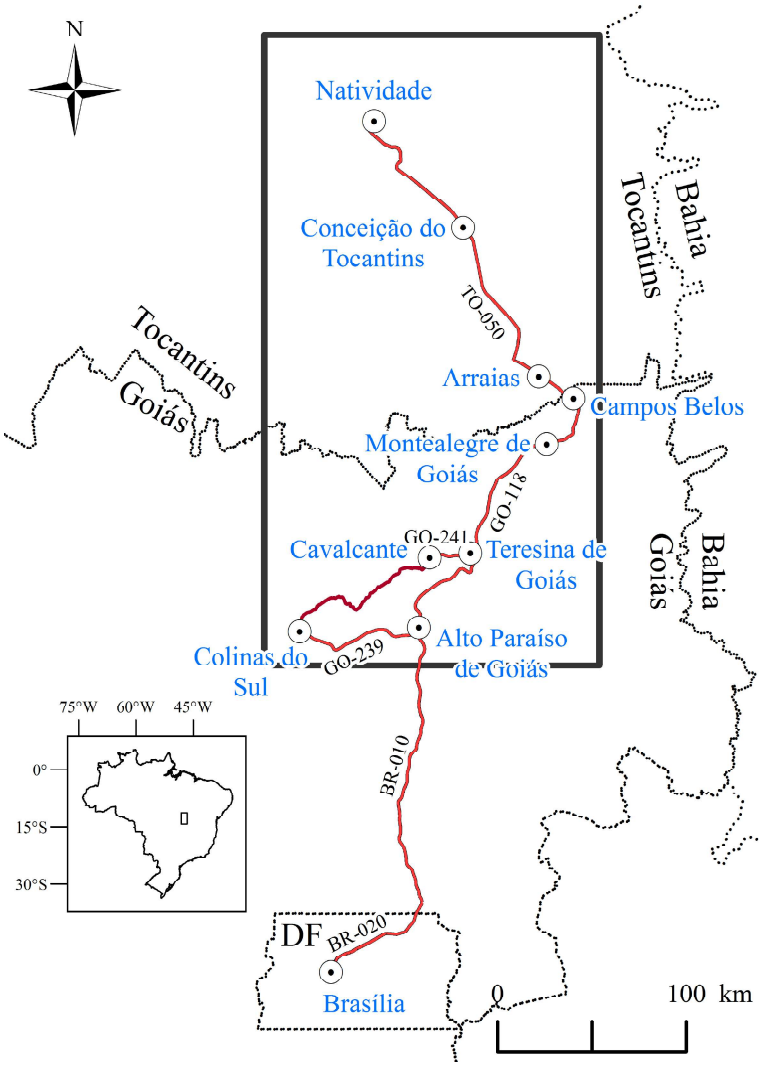

Fig. 1.1. Localização e vias de acesso à área de estudo (retângulo preto).

CAPÍTULO 2 - CONTEXTO GEOLÓGICO REGIONAL

A Província Tocantins localiza-se na parte central do território brasileiro e representa essencialmente uma zona orogênica Neoproterozóica (Brasiliana-Panafricana) que marca a colisão entre três blocos continentais principais: o Cráton Amazônico a oeste, o Cráton São Francisco a leste e o bloco Paranapanema no sul (Almeida *et al.*, 1981; Pimentel e Fuck, 1992; Strieder e Suita, 1999). A Província Tocantins é por sua vez composta por três faixas dobradas principais, sendo estas as Faixas Paraguai e Araguaia que bordejam os setores sudeste e leste do Cráton Amazônico, respectivamente, e a Faixa Brasília que bordeja a margem oeste do Cráton São Francisco (Fig. 2.1).

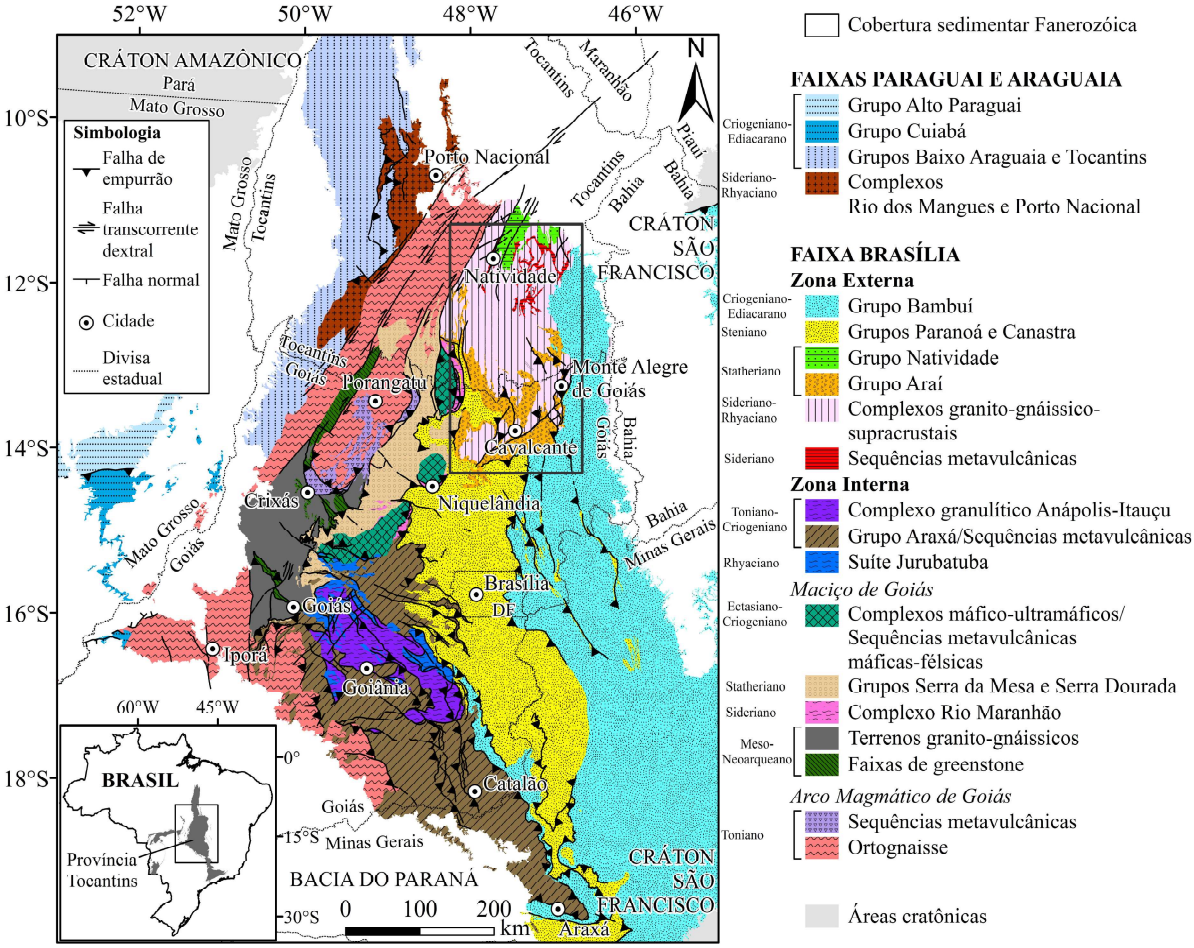

Fig. 2.1. Mapa geológico simplificado da Faixa Brasília. Modificado de Pimentel *et al.* (2004) com ajuda das cartas geológicas ao milionésimo do Serviço Geológico Brasileiro (CPRM: http://geobank.cprm.gov.br/). A área do presente estudo é indicada pelo retângulo localizado na porção NE da faixa.

A Faixa Brasília extende-se por mais de 1000 km entre as latitudes 10°S e 20°S seguindo uma direção geral N-S (Fig. 2.1). Geologicamente, a faixa é dividida em vários

setores (Fuck *et al.*, 1994; Dardenne, 2000; Pimentel *et al.*, 2004; Valeriano *et al.*, 2008) os quais consistem, de leste para oeste, em:

(i) Uma região de antepaís na borda oeste do Cráton São Francisco onde predominam camadas sedimentares subhorizontais do Neoproterozóico com leve metamorfismo e deformação (Grupo Bambuí) cobrindo um embassamento cristalino Arqueano-Paleoproterozóico.

(ii) Uma zona externa composta na parte setentrional por um bloco crustal de embassamento Paleoproterozóico coberto parcialmente por sequências de rift levemente dobradas (Grupo Araí; ~ 1.77 Ga), as quais são por sua vez cobertas por rochas sedimentares Neoproterozóicas do Grupo Paranoá que na parte leste são empurradas sobre o Grupo Bambuí. Na parte meridional da zona externa é apreciável um caráter tectônico mais complexo nas sequências supracrustais (grupos Paranoá, Canastra, Vazante e Ibiá) as quais são dobradas e empurradas sobre rochas pelíticas e carbonáticas do Grupo Bambuí formando estruturas vergentes para SE.

(iii) Uma zona interna caracterizada por sistemas de nappes com gradientes metamórficos invertidos que cavalgam as faixas de dobramento e empurrão da zona externa. Estes nappes são compostos na base por intercalações de metapelitos, quartzitos, paragnaisses, rochas calcisilicáticas e metamáficas com características indicativas de ambientes plataformais distais e fundo oceânico, pertencentes aos grupos Araxá e Andrelândia (Neoproterozóico). No topo, os nappes são constituídos por rochas metamáficas e metassedimentares aluminosas em fácies anfibolito-granulito do Complexo Anápolis-Itauçu (Neoproterozóico), que localmente atingiram condições metamórficas de ultra-alta temperatura.

(iv) Um bloco denominado de Maciço de Goiás, em cujo setor SW afloram complexos TTG bordejados e separados por sequências metavulcanossedimentares de faixas greenstone contendo metakomatiitos e metabasaltos. Estes complexos granito-greenstone possuem idades de até 3.0 Ga e adicionalmente sofreram eventos termais posteriores a 2.0-2.2 Ga e ~0.63 Ga. No setor NE do Maciço de Goiás localizam-se três complexos máficos acamadados Neoproterozóicos (de norte para sul, Cana Brava, Niquelândia e Barro Alto) dispostos ao longo de um trend NNE por ~300 km, e que foram empurrados para o Leste sobre um embassamento gnáissico. Estes complexos sofreram metamorfismo em fácies granulito logo depois de cristalizados e são tectônicamente justapostos por

sequências metavulcanossedimentares que atingiram fácies anfibolito (de norte para sul, Palmeirópolis, Indaianópolis/Coitezeiro e Juscelândia).

(v) uma faixa NE-SW denominada de Arco Magmático de Goiás composta por rochas intrusivas variando em composição desde gabro até granito, além de tonalitos, granodioritos e dioritos deformados, e rochas supracrustais. As rochas cristalinas desta região possuem idades distribuídas em duas faixas distintivas entre 0.80-0.89 Ga e 0.60-0.66 Ga, e apresentam assinaturas isotópicas de Nd e Sr que indicam um caráter juvenil (*e.g.*, Pimentel e Fuck, 1992; Pimentel *et al.*, 2000; 2004; Laux *et al.*, 2005).

CAPÍTULO 3 - MÉTODOS ANALÍTICOS

3.1. GEOQUÍMICA DE ELEMENTOS MAIORES E TRAÇO

As análises em rocha total foram realizadas pela AcmeLabs Ltd. seguindo as rotinas analíticas 4A e 4B. A primeira delas consistiu na determinação de elementos maiores e menores por meio de ICP-AES de 0.2 g de amostra moída e homogeneizada após fusão com metaborato/tetraborato de lítio e digestão em HNO_3 diluído. As perdas por ignição foram medidas por diferença em peso após combustão a 1000ºC, enquanto que as análises de carbono e enxofre totais foram feitas por meio da rotina 2A em forno Leco. Na rotina 4B, as concentrações dos ETR e elementos refratários foram determinadas com ICP-MS aplicando a mesma preparação usada na rotina 4A. Adicionalmente, uma fração separada de 0.5 g foi dissolvida em água régia e analisada por ICP-MS. Os resultados dos elementos maiores e menores foram reportados como porcentagens em peso dos óxidos com limites médios de detecção (LMD) de 0.01 % em peso (exceto para o Cr_2O_3 e o Fe_2O_3 que tiveram LMD de 0.002 e 0.04 % em peso, respectivamente). Todo o ferro nas amostras foi reportado como Fe_2O_3. O LMD para as análises 2A Leco foi 0.02 % em peso. Para os elementos traço, os LMD obtidos foram 0.01 ppm (Tb, Tm e Lu), 0.02 ppm (Pr, Eu e Ho), 0.03 ppm (Er), 0.05 ppm (Sm, Gd, Dy e Yb), 0.1 ppm (La, Ce, Cs, Hf, Nb, Rb, Ta, U, Y, Zr e Cu), 0.2 ppm (Th), 0.3 ppm (Nd), 0.5 ppm (Ga e Sr) e 1 ppm (Ba, Sn e Zn).

3.2. GEOCRONOLOGIA DE U-Pb EM ZIRCÃO

O método e arranjo dos equipamentos usados nas análises isotópicas de U-Pb foram baseados no procedimento apresentado por Bühn *et al*. (2009). As análises foram realizadas no laboratório de geocronologia da Universidade de Brasília usando um espectrômetro de massa Thermo Finnigan Neptune Multicollector ICP-MS. A entrada da substância mineral no espectrômetro foi conseguida por meio de ablação com um laser de estado sólido New Wave 213 μm Nd-YAG. O diâmetro do feixe foi de 30 μm com uma energia próxima de 3.1 J/cm^2 e frequência de 10 Hz.

Os grãos de zircão que foram concentrados com ajuda de uma bateia a partir de amostras de rocha britada, foram posteriormente catados manualmente e montados em tubos plásticos de 9 mm de diâmetro preenchidos com resina. Os grãos foram posteriormente polidos usando pasta de diamante de 3 e 1 μm de diâmetro e limpados

com ultrassom em HNO_3 a 3% e água purificada. Posteriormente, imagens de catodoluminiscência (CL) foram adquiridas para ajudar a posicionar corretamente o feixe do laser de acordo com a estrutura interna dos minerais durante a fase de ablação.

O preparado com os grãos foi inserido em uma câmara com um fluxo de He entre 0.35 e 0.45 l/min. A remoção do ^{204}Hg no fluxo de He foi conseguida passando o gás através de tubos de vidro contendo partículas de quartzo cobertas com ouro; isto foi feito para minimizar a interferência isobárica com o ^{204}Pb e permitir a aplicação das correções do Pb comum.

Depois de passar no plasma de argônio, o material vaporizado foi transportado até a zona do detector que consistiu em três contadores de íons multicanal (MICs) e quatro copos de Faraday. Para a análise do padrão e as amostras, os sinais foram coletados em um bloco único com 40 ciclos, cada um deles com duração de 1.049 s, e começando as leituras dos sinais só após os últimos terem atingindo a máxima intensidade depois do início da ablação.

A técnica de *standard bracketing* foi aplicada por meio das leituras da análise de um ponto no padrão e um "branco" a cada oito pontos analisados nas amostras, com o objetivo de considerar o erro causado pela deriva instrumental do espectrômetro. O padrão internacional usado foi o zircão GJ-1, fornecido pelo ARC National Key Centre for Geochemical Evolution and Metallogeny of Continents (GEMOC) na Austrália. As suas idades de referência segundo Jackson *et al*. (2004) são: 608.6 ± 1.1 Ma (idade $^{207}Pb/^{206}Pb$), 600.4 ± 1.8 Ma (idade $^{206}Pb/^{238}U$) e 602.1 ± 3.0 Ma (idade $^{207}Pb/^{235}U$). Quando disponível, foram realizadas análises do zircão de referência 91500 (Wiedenbeck *et al*., 1995; 2004) durante as mesmas sessões analíticas das amostras, com o objetivo de testar a reproducibilidade dos dados obtidos.

A redução dos dados foi conseguida usando uma planilha elaborada no mesmo laboratório de geocronologia, avaliando as razões isotópicas dos 40 ciclos com um critério de rejeição baseado em um nível de confiança 2σ. As razões isotópicas corrigidas junto com suas idades calculadas associadas foram plotadas usando a rotina ISOPLOT 3.75 (Ludwig, 2012).

3.3. GEOQUÍMICA ISOTÓPICA DE Sm-Nd

As análises de Sm-Nd foram realizadas no laboratório de geocronologia da Universidade de Brasília seguindo os procedimentos descritos por Gioia & Pimentel

(2000). As amostras de rocha foram moídas e homogeneizadas para separar 50-100 mg de material que foi dosado com soluções ^{149}Sm e ^{150}Nd, e posteriormente atacado com 1 ml de HNO_3 e 4 ml de HF em bombas de teflon com revestimento de aço. Após dissolução, as amostras foram secadas e atacadas de novo com a mesma mistura ácida durante quatro dias a 190ºC, continuando posteriormente com uma nova fase de secagem e dissolução com 2 ml de HNO_3 concentrado. Depois de secado, o resíduo foi dissolvido mais uma vez com 6 ml de HCl (6N) para ser novamente secado e, por fim, dissolvido em 2 ml de HCl (2.5N).

A separação dos ETR foi feita em uma coluna primária de quartzo de 15 cm altura contendo 12 cm de resina catiônica Bio-Rad AG 50W-X8 200-400 *mesh* em solução aquosa. A amostra em solução foi eluida através da coluna usando HCl. Os ETR foram coletados na fração entre 1 e 15 ml do HCl 6N após eluição com 32 ml de HCl 2.5 N. A coluna foi regenerada com 15 ml de HCl 6N e armazenada em solução com ácido diluído. O HCl 2.5N foi padronizado mediante titrimetria usando $NaCO_3$ (anidro) como base e alaranjado de metila como indicador.

Para conseguir separar o Sm do Nd, a solução de ETR em 200 µl de HCl 0.18N foi passada através de uma coluna secundária de Savillex® de 10 cm de altura contendo 6.5 cm de resina LN-Spec (resina liquida HDEHP 270-150 *mesh* em teflon coberto com di-etilexil ácido fosfórico). A fração de Nd foi coletada em 4 ml de HCl 0.3N após 10 ml iniciais de HCl 0.18N. Com a coleta do Nd completada, 2 ml de HCl 0.3N foram descartados para depois obter o Sm em 4 ml de HCl 0.4N com uma velocidade de fluxo de ~1 ml/30 min. A regeneração da resina foi feita usando 6 ml de HCl 6N, e a coluna foi condicionada novamente com 3 ml de água purificada seguida de duas passadas com 3 ml de HCl 0.18N.

A fração coletada na coluna secundária foi evaporada junto com duas gotas de H_3PO_4 0.025N. O resíduo foi dissolvido em 1 µl de HNO_3 destilado a 5% e colocado em um filamento duplo de Re. O espectrômetro de massa usado foi um Finnigan MAT 262 com sete coletores em modo estático.

As incertezas nas razões $^{147}Sm/^{144}Nd$ e $^{143}Nd/^{144}Nd$ foram menores do que 0.2% (2σ) e 0.0064% (2σ), respectivamente, com base na análise do padrão internacional BHVO-1. A razão $^{143}Nd/^{144}Nd$ foi normalizada usando $^{146}Nd/^{144}Nd = 0.7219$. A constante de decaimento radioativo usada foi 6.54×10^{-12} a^{-1} (Lugmair & Marti, 1978).

3.4. ESPECTROSCOPIA RAMAN

As análises Raman em grafita foram realizadas seguindo a metodologia apresentada por Beyssac *et al*. (2002). Lâminas polidas de amostras de rocha com material grafitoso foram estudadas petrograficamente para escolher lamelas de grafita completamente contidas dentro de minerais incolores como quartzo e muscovita. Entre 20 e 30 lamelas de grafita foram escolhidas por amostra. Os espectros Raman foram obtidos no centro de nanociências e nanobiotecnologia do Instituto de Física da Universidade de Brasília, usando um espectrômetro triplo Jobin-Yvon modelo T64000 acoplado a um microscópio óptico com objetiva de 50X que permitiu a transmissão de um feixe de laser de ~5 μm de diâmetro. O sinal foi gerado mediante excitação com laser de íon Argônio Coherent CW na linha de 514.5 nm à temperatura ambiente, e lido mediante um detector tipo CCD refrigerado com nitrogênio líquido.

Os espectros Raman resultantes no intervalo entre 1200 e 1800 cm^{-1} foram tratados inicialmente usando o algoritmo proposto por Cadusch *et al*. (2013) para remoção do ruído causado por fluorescência, aplicando um modelo de segunda ordem e peso simples com parâmetro de atenuação $\gamma=10^6$. Posteriormente, o software PeakFit v.4.12 foi utilizado para o cálculo das áreas dos picos modelados com função Voight.

CAPÍTULO 4 - "THE PERALUMINOUS AURUMINA GRANITE SUITE IN CENTRAL BRAZIL: AN EXAMPLE OF MANTLE-CONTINENTAL CRUST INTERACTION IN A PALEOPROTEROZOIC CORDILLERAN HINTERLAND SETTING?"

ABSTRACT

The Peraluminous granites and tonalites/granodiorites of the Aurumina Suite crop out in the external zone of the Brasília Fold Belt on the western margin of the São Francisco Craton. Rocks of this suite intrude retrograde medium-grade schists and paragneisses of the Ticunzal Formation and display a magmatic muscovite±biotite± garnet assemblage and discrete graphite lamellae. The suite is divided into six members (Au1 through Au6), which grade from synkinematic to post-kinematic in character with ages spanning from 2.11 to 2.16 Ga according to zircon U-Pb data. Compositional features of the Aurumina Suite and associated coeval metaluminous mafic to intermediate plutons suggest an origin by source hybridization processes characterized by reaction between metasedimentary rocks and basaltic melts that would have taken place at shallow depths (pressure < 5 kbar). This is supported by a narrow range of ε_{NdT} values between -4.2 and +0.4 for samples from both peraluminous and metaluminous units. Possible sources could correspond to old reworked crust that might also be related to the origin of ~2.2 Ga peraluminous magmatic rocks in the Almas-Dianópolis domain, although participation of unknown sources is also feasible. Similarities exist between the peraluminous magmatism of the Aurumina Suite and the Jurassic-Paleogene peraluminous granitic belt of the cordilleran interior of North America in terms of composition, rock association and tectonometamorphic context, which suggest a similar tectonic setting for the Aurumina Suite instead of the collisional setting suggested in previous works.

Keywords: São Francisco Craton; Brasília Fold Belt; Aurumina Suite; peraluminous magmatism; cordilleran hinterland; source hybridization.

4.1. INTRODUCTION

Peraluminous magmatism is commonly understood to be a prime expression of crustal reworking and differentiation that results from partial melting of metasedimentary

rocks (Chappell and White, 2001; Brown and Rushmer, 2005; Brown, 2013). It has been shown, however, that this is not always the case: not all peraluminous granites are derived from metasedimentary sources, and they might, in fact, originate from mantle-derived precursors (*e.g.*, White *et al*., 1986; Chappell and White, 2001; Chappell *et al*., 2012). Among the best-known examples of peraluminous granites around the world are the well-studied ones from the Lachlan Fold Belt in eastern Australia (Chappell and White, 1992; 2001, Chappell *et al*., 2000) and the typical leucogranites of the Himalayan-Karakoram range (*e.g.*, Searle *et al*., 2009; Searle, 2013). The geodynamic setting of the former has been regarded as related to a succession of crustal thickening and extension events following several episodes of orogen accretion in a subduction zone (Collins and Richards, 2008), whereas the Himalayan leucogranites are widely attributed to a classical continent-continent collisional setting.

Another setting that hosts a conspicuous belt of peraluminous granites is that of the hinterland of the North American cordillera, between northern Sonora and southeastern British Columbia (Miller and Bradfish, 1980; Miller and Barton, 1990; Miller *et al*., 2003). This region features remarkable examples of two-mica and, in some instances, garnet-bearing granitic rocks that have both geochemical and isotopic evidence of either derivation from crustal sources or contribution of evolved crustal materials (*e.g.*, Tilling, 1973; Anderson and Rowley, 1981; Hyndman, 1983; Hyndman and Foster, 1988; Asmerom *et al*., 1988; Sevigny *et al*., 1989; Miller *et al*., 1990; Barton, 1990; Brandon and Lambert, 1994; Driver *et al*, 2000; Kapp *et al*., 2002; Lee *et al*., 2003). Among the main features of these rocks are their inward position within the continent in relation to a coeval magmatic arc, indirect association with subduction-zone magmatism, common association and mingling/mixing with more mafic mantle-derived magmas and occurrence during a major period of compressional deformation and metamorphism. Recent models note subduction-induced flow of the asthenosphere, delamination of lithospheric mantle in a thickened lithosphere, and subsequent ascent of hot asthenosphere as the mechanisms that allowed both the heat flux necessary to melt the crust and the generation of the mafic components during the Late Jurassic-early Paleogene period in the North American hinterland (Elison, 1995; Leventhal *et al*., 1995; Wells and Hoisch, 2008), although models invoking thermal blanketing by the thickened crust without involving the mantle have also been proposed (*e.g.*, Patiño-Douce *et al*., 1990). The locus of this magmatism coincided with the edge of old continental crust of

cratonic affinity, where late Precambrian-early Paleozoic passive margin sequences were deposited before the onset of a convergent margin to the west (*e.g.*, Stewart, 1972; 1976; Bond *et al*., 1985). It is likely that this old crust is responsible for the characteristic isotopic signature inherited by the peraluminous magmas occurring in the hinterland (Miller and Barton, 1990).

The Aurumina Suite crops out over more than 15,200 km^2 in central Brazil, representing a voluminous peraluminous magmatic event of Rhyacian age on the western border of the São Francisco Craton, with rocks varying from tonalite/granodiorite to granite in composition (Botelho *et al*., 1999). Since the definition of the suite, two main questions have remained unanswered: i) what process/source could account for such a large volume of peraluminous tonalitic rocks, and ii) in what tectonic context was the Aurumina Suite formed because no evidence for a classical collisional setting has been found in the region. In this work, we present new geochemical, geochronological and isotopic data to address these questions. As a result, a comparison with the peraluminous granites of the North American hinterland is established, and a similar tectonic setting is inferred for this Paleoproterozoic province in the external zone of the Brasília Fold Belt.

4.2. GEOLOGICAL SETTING

4.2.1. Regional framework

The Tocantins Province in central Brazil is commonly regarded as a Neoproterozoic orogenic feature marking amalgamation of three main continental blocks: the Amazonian Craton, the São Francisco Craton, and the Paranapanema block (Almeida *et al*., 1981; Pimentel and Fuck, 1992; Strieder and Suita, 1999). Three main fold belts make up the Tocantins Province: the Paraguay and Araguaia fold belts on the southeastern and eastern margins of the Amazonian Craton, respectively, and the Brasília Fold Belt (BFB) on the western margin of the São Francisco Craton. The BFB extends for more than 1000 km between latitudes 10ºS and 20ºS and follows a general N-S trend (Fig. 4.1).

The BFB is divided into a number of sectors (Fuck *et al*., 1994; 2017; Dardenne, 2000; Pimentel *et al*., 2004; Valeriano *et al*., 2008), one of them corresponding to an external zone composed in its northern part of 2.45-2.0 Ga basement (Fig. 4.2) referred to as the Cavalcante-Natividade block (Fuck *et al*., 2014). According to Cruz (2001) and Cruz *et al*. (2003), in the northern part of this block, known as the Almas-Conceição do Tocantins domain, the Almas-Dianópolis granite-gneiss terrane encompasses the

Ribeirão das Areias Complex (2.45 Ga) and a suite of peraluminous rocks (2.2 Ga), both of which contain tonalite, granodiorite, trondhjemite, and minor monzogranite. A suite of 2.2 Ga metaluminous tonalite, granodiorite, trondhjemite, quartz diorite and quartz monzodiorite is also present. The above-mentioned units intrude a greenstone sequence known as the Riachão do Ouro Group, which is composed of mafic to ultramafic volcanic rocks and a sequence of metasedimentary and felsic volcanic rocks (Costa, 1985; Cruz and Kujumjian, 1996; 1998).

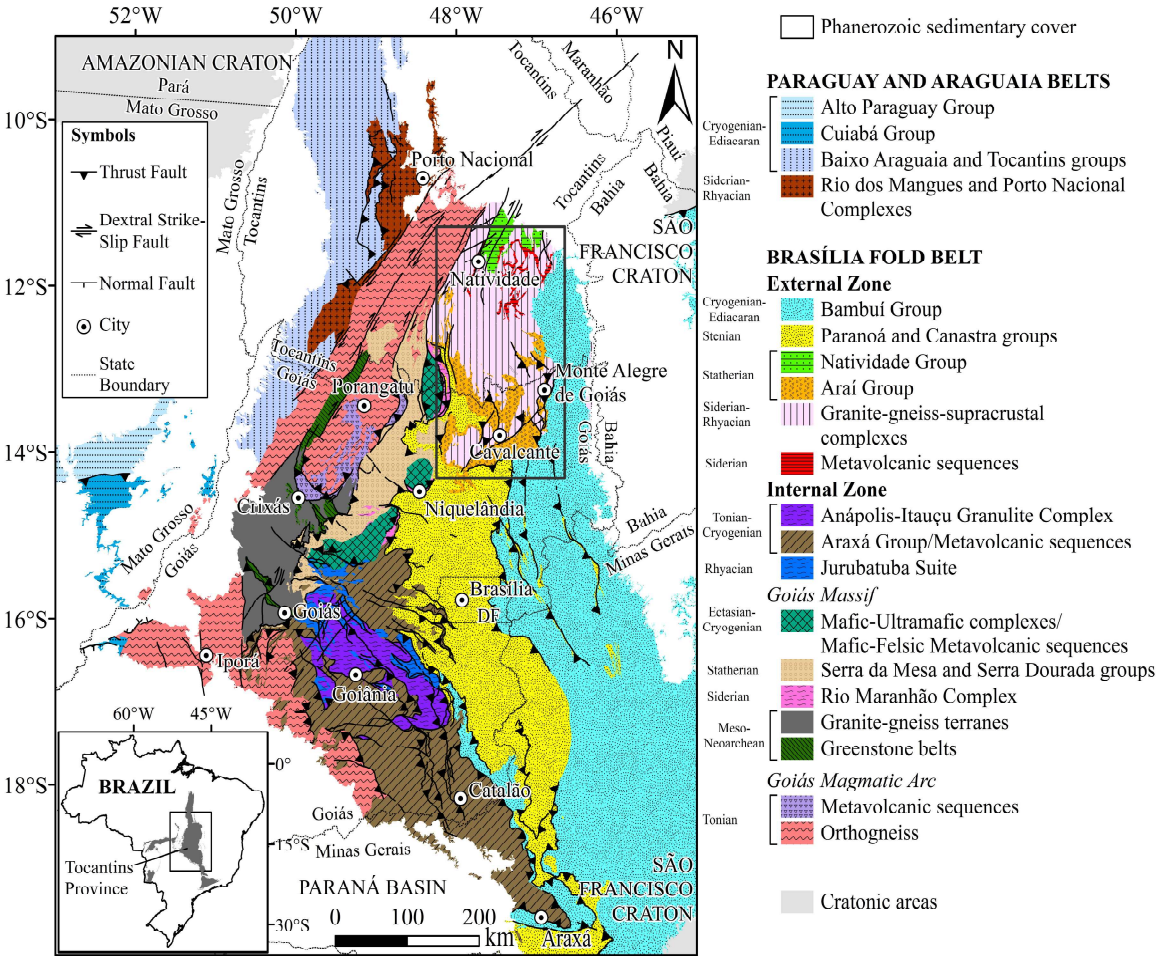

Fig. 4.1. Geological sketch of the Brasília Fold Belt. Modified after Pimentel *et al.* (2004). Studied area indicated by rectangle in the central-top right portion of the image.

The southern portion of the Cavalcante-Natividade block, namely the Cavalcante-Arraias domain (Fig. 4.2), is intruded by tin-bearing A-type granites of the Pedra Branca Suite and partially covered by the slightly deformed volcanic-sedimentary sequences of the Araí Group, with the latter two units representing a rifting event that took place at ~1.77 Ga. A later anorogenic magmatic event at ~1.58 Ga is represented by the tin-

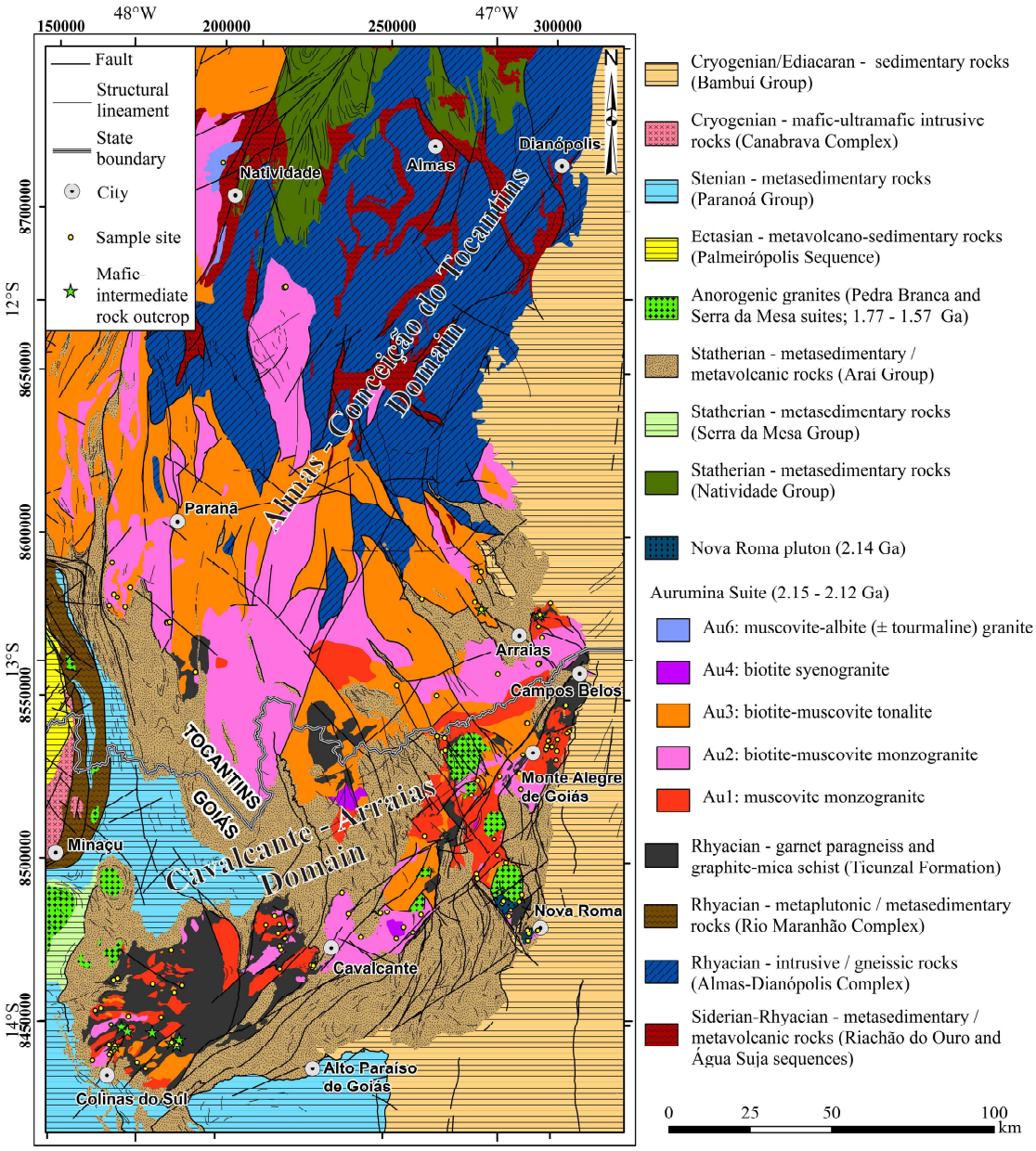

Fig. 4.2. Geological map of the studied area (see Fig. 4.1 for reference). Based on geological charts SC.23, SD.22, SD.23, SC.22-Z-D, SD.22-X-D, SD.23-V-A, SC.23-Y-C, SD.23-V-C-III, SD.23-V-C-V and SD.23-V-C-VI by the Brazilian Geological Survey (CPRM; http://geobank.cprm.gov.br/). Unit Au5 is not shown due to its small outcrop area. The location of outcrops of mafic to intermediate rocks close to Colinas do Sul and Arraias is indicated with star symbols.

bearing granites of the Serra da Mesa Suite (Pimentel *et al.*, 1991; 1999). Meso- to Neoproterozoic sedimentation in this domain is represented by the Paranoá and Bambuí groups in the southern and eastern portions, respectively. The basement of the Cavalcante-Arraias domain is essentially sialic crust comprising medium-grade paragneisses and schists, and peraluminous granites and tonalites. Due to poor mapping and a lack of geochemical data, the paragneisses, peraluminous granites and tonalites were formerly grouped into a granite-gneiss complex that extended through a large

portion of the northern and western sectors of the BFB (*e.g.*, Marini *et al*., 1984a, 1984b). Through detailed mapping campaigns and geochemical work, Botelho (1992) started separating distinctive units based on compositional contrasts. Thus, units such as the Nova Roma pluton, the "gray granites" that host younger tin-bearing anorogenic granites, and the peraluminous granite cropping out in the Aurumina village were recognized for the first time. Later mapping campaigns carried out by undergraduate geology students of the University of Brasília led to a better geological understanding of the region, allowing Botelho *et al*. (1999) to define the Aurumina Suite as a group of peraluminous granites and tonalites that concordantly intruded schists and paragneisses of the retrograde medium-grade Ticunzal Formation (Marini *et al*., 1978; 1984b; Fernandes *et al*., 1982).

4.2.2. Local geology

4.2.2.1.Ticunzal Formation

According to Marini *et al*. (1984b), schists that crop out in the Ticunzal Range (the type area of this formation located west of Cavalcante) are up to 300 m in thickness in the upper portion of the sequence, while paragneisses of the lower portion are up to 200 m thick. The main rock types of the formation include paragneisses with varying amounts of biotite, muscovite, garnet and graphite, as well as quartz-muscovite schists, muscovite-garnet schists, tourmaline schists, chlorite-muscovite-quartz schists and graphite schists, the latter being the most representative lithology. Although rare, metaconglomerate and quartzite are also found in some sections of the formation.

The rocks of the Ticunzal Formation display a mineral assemblage consisting of chlorite, epidote, carbonate and fine muscovite, which suggests retrograde metamorphism from amphibolite to greenschist facies. The presence of relict garnet and high-crystallinity carbonaceous matter (*i.e.*, graphite) also points to this. Chiastolite can also be found close to contacts with Aurumina Suite intrusions.

The Ticunzal Formation constitutes the oldest unit so far found within the Cavalcante-Arraias domain with no older units found in outcrop to date. In thin section, paragneisses commonly display lepidoblastic foliation that is sometimes enhanced by parallel arrangements of quartz ribbons. This foliation, however, is not always evident, leading in some cases to confusion with granites of the Aurumina Suite. Garnet is useful in dismissing this confusion, as this mineral is common in the paragneisses but rare within

the granitic rocks, except for a discrete body of garnet tonalite and some muscovite granites. The same applies to graphite, which often occurs as relatively abundant discrete fine lamellae in the paragneisses. The paragneisses are mainly composed of quartz (the most abundant mineral at >50%), plagioclase and microcline, the latter two commonly occurring in sub-equal amounts. Mica contents are seldom greater than 10%, and garnet is usually present as subhedral grains in amounts no greater than 5%. Accessory minerals include zircon, monazite, apatite, magnetite, ilmenite and graphite. Quartz and feldspars are anhedral, with the former typically displaying polygonization, sub-grain formation and sutured boundaries. Biotite and muscovite are mostly subhedral, with bands rich in these minerals commonly being finer grained than the quartz-feldspar layers (Fig. 4.3a). Granoblastic textures with characteristic triple junctions are sometimes found in quartz-rich layers, while garnet displays poikiloblastic textures with inclusions of quartz and biotite.

The schists are fine grained and display a well-developed lepidoblastic foliation that is sometimes accompanied by compositional banding defined by alternating mica-, quartz- or graphite-rich layers. Muscovite and chlorite constitute > 50% of most schist varieties, with subordinate biotite locally attaining up to 10%. The remainder is usually composed of quartz, feldspar, iron oxides and graphite, the latter mineral varying from absent to dominant in graphite-schist samples. Quartz and muscovite porphyroblasts are sometimes observed, as well as rounded to sub-angular grains of accessory garnet and apatite. Quartz-rich bands commonly have a granoblastic texture, with individual grains displaying polygonization, sub-grain formation and sutured boundaries. In some cases, mylonitic features, such as S-C structures and sigmoidal porphyroclasts, are observed. At least two deformational phases can be recognized in the Ticunzal Formation, as inferred from the crenulation foliation and truncated relict lepidoblastic foliations found in some mica-schist samples.

Geochemically, the rocks display rather variable K_2O/Na_2O and TiO_2/Zr ratios coupled with high MgO values, suggesting a mainly pelitic protolith with variable contributions from graywackes and arkosic psammites. The age of the Ticunzal Formation is not well constrained, but it is regarded as likely lower Paleoproterozoic (Rhyacian) in age, as suggested by T_{DM} ages between 2.0 and 2.8 Ga (Pimentel *et al.*, 2004; Botelho *et al.*, 2006a; Fuck *et al.*, 2014).

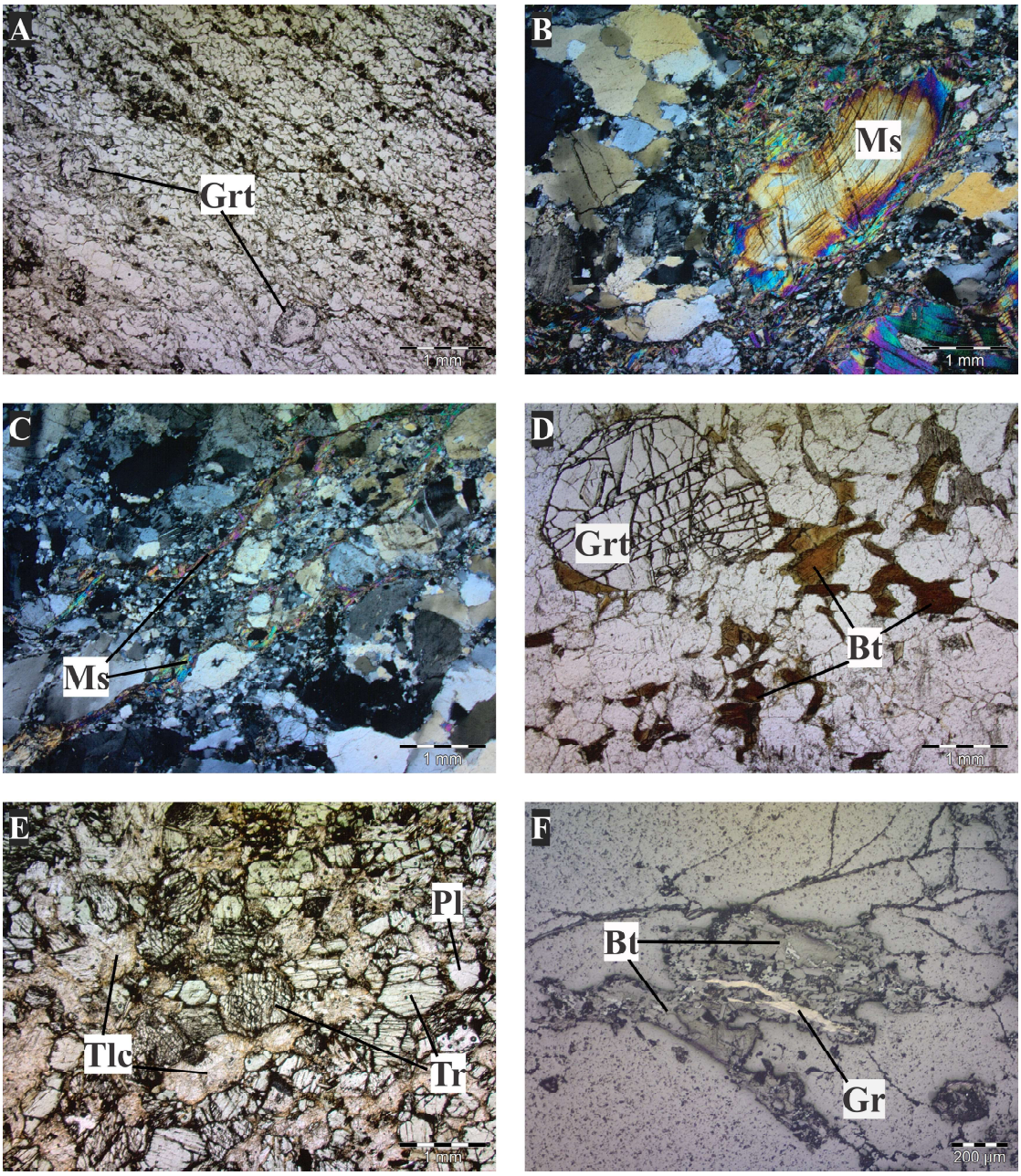

Fig. 4.3. Photomicrographs of some rock types found within the studied area. **A**: Garnet (Grt)-biotite paragneiss of the Ticunzal Formation. Note foliation in the SE-NW direction of the photograph and garnet porphyroblasts at both the bottom and left portions of the image. Parallel-polarized light. **B**: Muscovite granite displaying a large magmatic muscovite (Ms) crystal (center) surrounded by secondary, fine-grained muscovite, quartz and feldspars. Crossed-polarized light. **C**: Muscovite (Ms) granite displaying mylonitic deformation as evidenced by muscovite-defined foliation (SW-NE direction of the image) and mortar texture. Crossed-polarized light. **D**: Garnet (Grt)-biotite (Bt) tonalite. Note large subhedral garnet crystals displaying equilibrium contacts with biotite in the upper-left portion of the image. Parallel-polarized light. **E**: Metamafic rock displaying tremolite (Tr)-talc (Tlc)-plagioclase (Pl) paragenesis. Parallel-polarized light. **F**: Graphite (Gr) lamellae associated with a biotite (Bt) cluster in biotite granodiorite. Reflected parallel light.

4.2.2.2.Aurumina Suite

Botelho *et al*. (1999) originally described the rocks of this suite as medium- to coarse-grained foliated granites and granodiorites/tonalites composed of quartz, perthitic

microcline, plagioclase, biotite and muscovite, with zircon, apatite, monazite, thorite, ilmenite, garnet and fluorite as accessory minerals. The aluminum saturation index is greater than 1, and the TiO_2 content is rather high in muscovite (0.5-1.7 wt.%: Botelho *et al*., 1999; Pereira, 2001), both of which suggest an origin from peraluminous magmas. In addition, these rocks locally host Au, U, Pd, Pt, Sn and Ta mineralizations (Marini e Botelho, 1986; Botelho *et al*., 1999; 2006b; Menez, 2016).

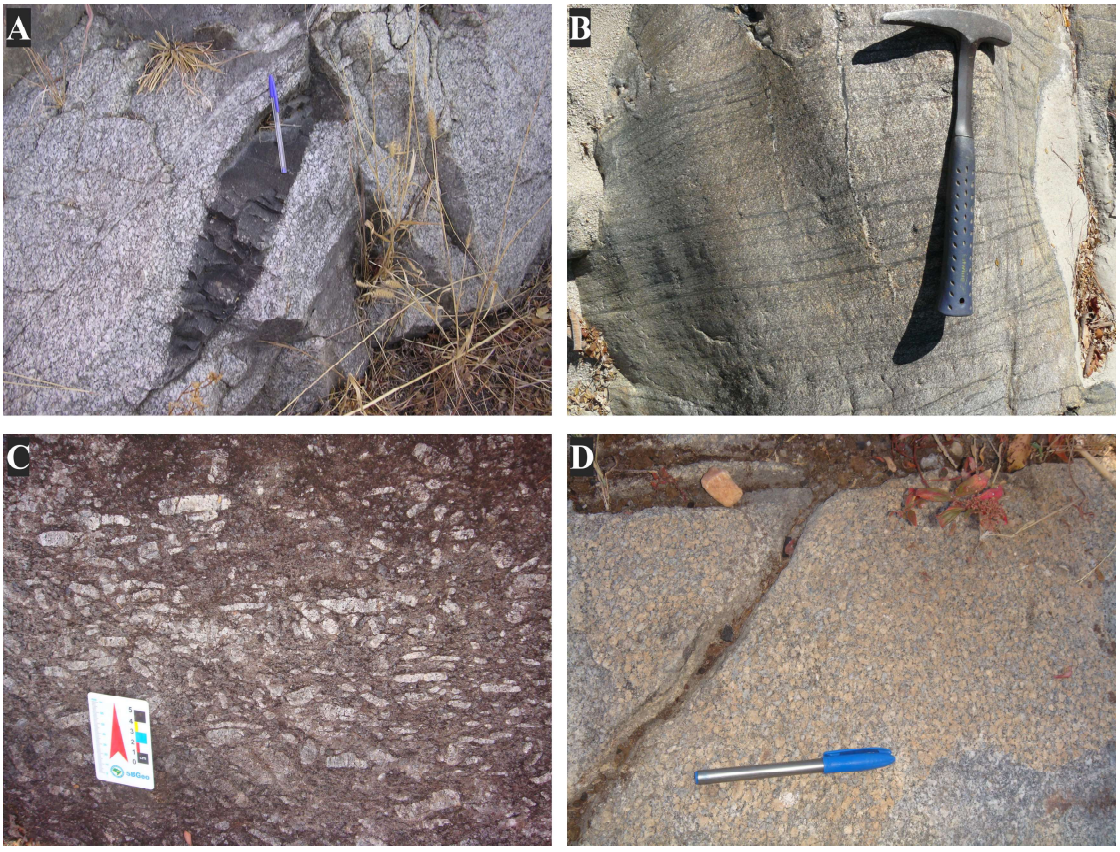

Fig. 4.4. Macroscopic features of Aurumina Suite rocks. **A**: Muscovite-biotite granite (Au1) displaying a lens-shaped paragneiss xenolith at the central portion of the picture. **B**: Biotite-muscovite granite (Au2) with igneous layering defined by the parallel arrangement of dark, millimeter-thick biotite bands. **C**: Porphyritic biotite-muscovite granite (Au4) with subparallel arrangement of microcline phenocrysts. **D**: Equigranular biotite-muscovite granite (Au2).

The rock types of the Aurumina Suite comprise, from oldest to youngest, muscovite monzogranite, muscovite-biotite monzogranite, biotite tonalite, biotite syenogranite, tourmaline leucogranite and tourmaline pegmatite (Fig. 4.4). These facies have been labeled as Au1, Au2, Au3, Au4 and Au6, respectively (Alvarenga *et al*., 2007). Facies Au5 is recorded in just one outcrop and corresponds to migmatitic granites intimately associated with the Ticunzal Formation.

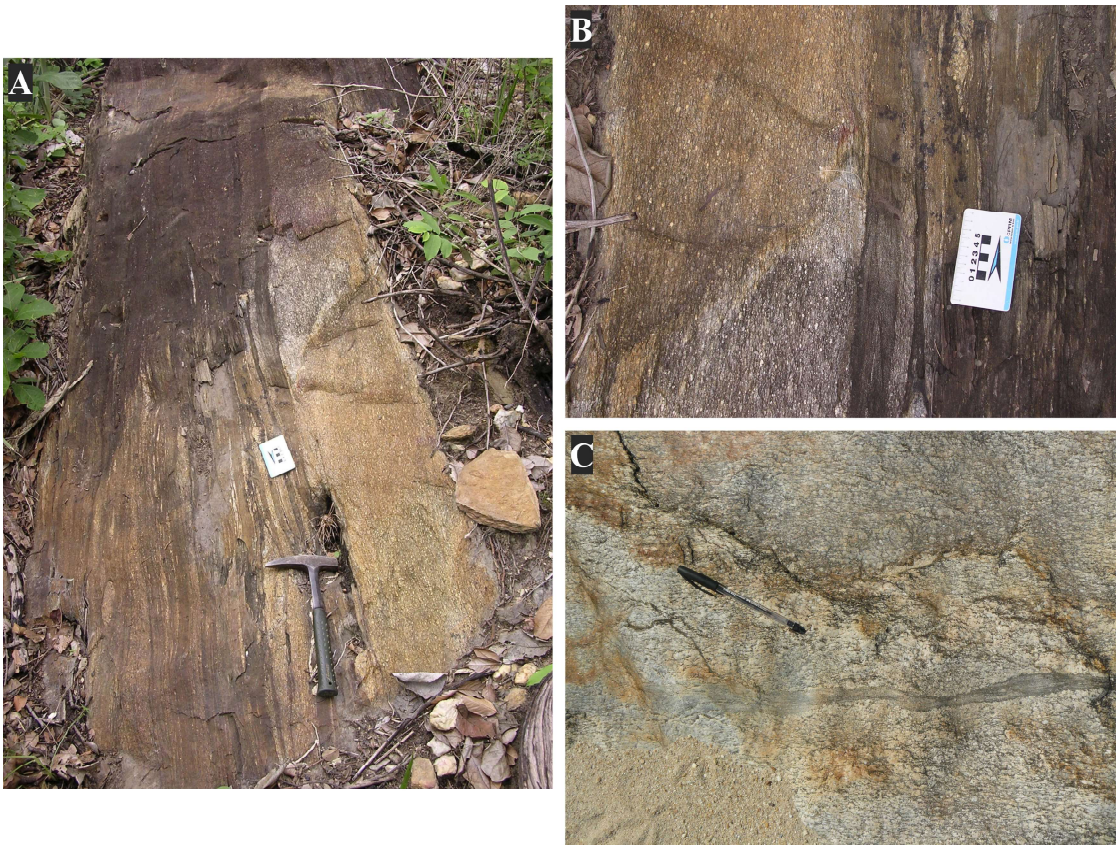

Fig. 4.5. Field relations between the Aurumina Suite and the Ticunzal Formation. **A**: Lit-par-lit intrusion of biotite-muscovite granite (light-colored rock) along foliation planes of Ticunzal Formation paragneiss (dark-colored rock). **B**: Detail of relation shown in A. **C**: Biotite-rich paragneiss enclave (center) in Aurumina Suite biotite tonalite (Au3). Note the progressive assimilation of the enclave as it gradually fades from right to left.

Intrusions vary from syn- to post-kinematic in character as evidenced by *lit-par-lit* structures in which members Au1 and Au2 intrude the Ticunzal Formation along foliation planes (Figs. 4.5a and 4.5b), as well as the existence of a N10-30E trending mylonitic foliation affecting both the granites and their metamorphic host rocks. Discordant styles of intrusion have also been observed, sometimes yielding irregular contact zones. Facies Au3, Au4, Au5 and Au6 typically show little to no deformation at all. Biotite-rich and/or graphite-bearing enclaves ranging from 0.5 to 30 cm in size are commonly found within rocks of this suite. Biotite-rich facies usually display rather strong gamma-ray spectrometric anomalies associated with high contents of monazite and/or thorite. Enrichments in P, Th, Rb, Li and Ta characterize granites of the Aurumina Suite along with highly fractionated REE patterns as illustrated by $(La/Yb)_N$ ratios commonly greater than 50 (Botelho *et al*., 2006a).

Granites belonging to the facies Au1, Au2, Au4 and Au5 are composed of quartz (~25-30%), microcline (30-35%), plagioclase (10-15%) and variable proportions of

muscovite and biotite (together up to 20%), with the syenogranites of facies Au4 having the largest amounts of biotite. Opaque minerals occur in small amounts (<1%) and are represented almost exclusively by ilmenite, although in some cases small lamellae of graphite occur randomly in interstices between quartz and feldspar grains, or along cleavage planes in micas (Fig. 4.3f). Accessory minerals commonly include rounded apatite, monazite and zircon, and alteration minerals, such as sphene and leucoxene, are observed as overgrowths on ilmenite. Epidote occurs either in association with altered biotite masses or as rims on monazite. The latter mineral is conspicuously abundant in facies Au4, where it can represent up to 1% of the rock. Tonalites and granodiorites of facies Au3 display a mineralogy similar to that of granites but with higher contents of plagioclase at the expense of microcline. Phosphate accessory minerals, like apatite and monazite, are less common in these rock types and biotite is typically reddish in color while displaying, in some cases, a sagenitic texture due to rutile exsolution. Locally, garnet is an abundant phase (up to 10%) and occurs as small poikilitic grains (Fig. 4.3d). Au6 phases represent strongly differentiated residual liquids that are, in some instances, composed of albite as the dominant feldspar, along with tourmaline, cassiterite and tantalite. Muscovite is the only mica in these rocks, which are typically zircon-poor while having conspicuous amounts of manganese-rich fluorapatite and garnet.

In members Au1 and Au2, most of the original magmatic texture has been obliterated by recrystallization processes, yielding proto- to meso-mylonitic textures in which preserved porphyroclasts of quartz, feldspars and muscovite are surrounded by a fine-grained, mortar-textured matrix (Figs. 4.3b and 4.3c). Within the matrix, a lepidoblastic foliation defined by fine-grained muscovite and/or biotite is usually observed. Other recrystallization features include granoblastic texture, undulose extinction and sutured boundaries in quartz as well as a poikiloblastic texture involving microcline engulfing smaller grains of plagioclase and quartz. Members Au3, Au4, Au5 and Au6 are commonly undeformed and show only minor recrystallization features in quartz and plagioclase.

Zircon U-Pb ages of Aurumina Suite samples vary between 2.12 and 2.18 Ga (Botelho *et al*., 2006a; Fuck *et al*., 2014; Corrêa *et al*., 2015; Sousa *et al*., 2016). These data are consistent with muscovite K-Ar ages (2.129 ±26 Ma and 2.006 ±26 Ma) and cassiterite U-Pb ages (2.277-2.023 Ma) obtained by Sparrenberger and Tassinari (1999) in peraluminous pegmatite samples from Monte Alegre de Goiás. $\varepsilon_{Nd(T)}$ values typically

vary between -1 and -3 (but with a full range between 0 and -7), and T_{DM} ages between 2.3 and 3.0 have been previously reported for the Aurumina Suite (Pereira, 2001; Botelho *et al*., 2006a; Fuck *et al*., 2014).

4.2.2.3.Mafic to intermediate rocks

Despite being far less abundant than the rocks of either the Aurumina Suite or Ticunzal Formation, some igneous units of mafic to intermediate composition crop out in the southern portion of the studied area, between Colinas do Sul and Arraias. Except for the Nova Roma plutons, these units occur as stocks or dykes too small to be shown in Fig. 4.2.

The Nova Roma pluton is an undeformed composite body that intruded mica-graphite schists of the Ticunzal Formation and Au2 muscovite-biotite granites of the Aurumina Suite. In some instances, a progressive assimilation of the host rocks can be observed in outcrop, yielding a hybrid rock type between metaluminous and peraluminous. In thin section, this unit consists of plagioclase (50%), quartz (20-25%), biotite (0-15%) and hornblende (0-10%). Some biotite-bearing samples even display discrete graphite lamellae occurring along cleavage planes of biotite. Accessory minerals include zircon, apatite, allanite and ilmenite, while epidote, muscovite and chlorite occur as alteration products. Plagioclase appears as strongly altered coarse anhedral grains, while biotite is subhedral and has small apatite and zircon inclusions. Alvarenga *et al*. (2007) reported a U-Pb zircon age of 2140 ± 7 Ma with a T_{DM} of 2.48 Ga and an ε_{NdT} value of -3.9 for this unit.

Close to the town of Arraias, small plutons and dykes of quartz diorite and tonalite intrude Au2 biotite-muscovite granites and Au3 biotite tonalites. These melanocratic rocks are composed of cummingtonite (30%), biotite (25%), plagioclase (40%) and quartz (5%). Ilmenite, chalcopyrite and zircon appear as accessory minerals, with hematite formed as alteration product of ilmenite. Cummingtonite appears as subhedral columnar crystals that in some instances have small inclusions of plagioclase. Biotite is typically anhedral and displays a characteristic compositional zoning in which the cores possess a stronger reddish color than the rims. Plagioclase occurs as anhedral altered grains displaying lobate borders.

Small plutons and dykes of meta-gabbro and meta-peridotite intrude the Ticunzal Formation close to Colinas do Sul. In general, these rocks display strong retrograde

metamorphism, rendering it difficult to recognize their primary mineralogy. Variable amounts of tremolite/actinolite, plagioclase, talc and biotite are found in these rocks, with epidote, leucoxene, titanite and zoisite as typical alteration phases (Fig. 4.3e). In some instances, quartz appears as an alteration phase (5-10%), but it is also possible that this mineral was part of the primary mineral assemblage. The original textures of these mafic/ultramafic rocks are pervasively transformed, but in some cases, it is possible to recognize relicts of cumulate textures where plagioclase is more abundant, as well as triple junctions in amphibole aggregates.

In addition to the latter mafic units, small intrusions of metaluminous tonalite are also found in the region of Colinas do Sul. These rocks are very similar to those of the Nova Roma pluton, and are composed mainly of biotite and uralitized clinopyroxene (20-30%) as the Fe-Mg phases, as well as plagioclase (45-50%), quartz (25-35%) and muscovite (<10%). Clinozoisite is an abundant phase in some samples (10-15%), and accessory minerals, such as zircon and Fe-Ti oxides, and alteration minerals such as chlorite and epidote, are common. Biotite with sagenitic texture is observed in the most melanocratic samples, and quartz distribution varies from homogeneous to interstitial between plagioclase and mica/amphibole crystals.

4.3. ANALYTICAL METHODS

4.3.1. Major and trace element geochemistry

Chemical analyses of rock powder were performed by AcmeLabs Ltd. following 4A and 4B routines. The 4A routine involved ICP-AES analysis of major and minor elements after lithium metaborate/tetraborate fusion and dilute HNO_3 digestion. In 4B routine, trace elements of selected samples were analyzed by ICP-MS following the same preparation as in 4A with digestion in aqua regia of an additional separate split. Several samples were analyzed by equivalent methods during previous projects in which only concentrations of a select group of trace elements were determined (Table 4.1).

4.3.2. Zircon U-Pb geochronology

The methodology and equipment set-up used for the U-Pb geochronology closely followed that presented by Bühn *et al*. (2009), to whom the reader is referred for further details. Geochronological U-Pb analyses were carried out at the geochronology laboratory of the University of Brasília using a Thermo Finnigan Neptune multicollector inductively coupled plasma mass spectrometer. The input of mineral substance into the

spectrometer was achieved by means of the laser ablation technique using a New Wave 213 µm Nd-YAG solid-state laser. A beam diameter of 30 µm and a laser energy of ~3.1 J/cm^2 at a frequency of 10 Hz were used. Samples were inserted into a He-flushed laser chamber with a gas flux between 0.35 and 0.45 l/min. The removal of ^{204}Hg from the He flux was achieved by passing the gas through glass tubes containing gold-coated quartz particles intended to minimize the isobaric interference with ^{204}Pb, thus allowing calculation of common lead corrections. For standard and sample analysis, the signals were collected in a single block with 40 cycles of 1.049 s each, with reading of the signals starting after they had attained their maximum following the onset of ablation.

The standard-sample bracketing technique was applied by analyzing one standard spot and one blank every eight sample spots, thus accounting for instrumental drift. The GJ-1 zircon provided by the ARC National Key Centre for Geochemical Evolution and Metallogeny of Continents (GEMOC) of Australia was used as standard. The reference ages of the standard are as follows: ^{207}Pb/^{206}Pb age = 608.6 ± 1.1 Ma, ^{206}Pb/^{238}U age = 600.4 ± 1.8 Ma, and ^{207}Pb/^{235}U age = 602.1 ± 3.0 Ma (Jackson *et al*., 2004). To test the reproducibility of the obtained age data, some analyses of the 91500 reference zircon (Wiedenbeck *et al*., 1995; 2004) were performed during the analytical sessions (Table 4.2). Data reduction was achieved using a spreadsheet developed at the geochronology laboratory of the Brasília University. This spreadsheet allowed evaluation of isotope ratios for every cycle on a 2σ rejection basis. The corrected ratios and associated calculated ages were displayed using Isoplot 3.75 (Ludwig, 2012).

4.3.3. Nd isotope geochemistry

All the whole-rock Sm and Nd isotope analyses were performed at the geochronology laboratory of the Brasília University. The analytical procedures applied in this study to measure the ^{147}Sm/^{144}Nd and ^{143}Nd/^{144}Nd isotope ratios were those described by Gioia and Pimentel (2000). Rock samples were ground to a powder and dosed with ^{149}Sm and ^{150}Nd spike solutions. The separation of Sm from Nd was accomplished using cation exchange columns followed by evaporation of the obtained fractions with two drops of 0.025 N H_3PO_4. The residue was dissolved in 1 µl of 5% distilled HNO_3 and loaded onto a double Re filament assembly. The mass spectrometer used was a Finnigan MAT 262 with 7 collectors in static mode. The uncertainties for ^{147}Sm/^{144}Nd and ^{143}Nd/^{144}Nd ratios were better than ±0.2% (2σ) and ±0.0064% (2σ), respectively, based on an analysis of the BHVO-1 international rock standard. The ^{143}Nd/^{144}Nd ratio was

normalized using $^{146}Nd/^{144}Nd=0.7219$, and the employed decay constant was 6.54×10^{-12} y^{-1} (Lugmair and Marti, 1978).

4.4. RESULTS

4.4.1. Geochemistry

The results of geochemical analyses are summarized in Table 4.1. The Aurumina Suite rocks vary widely in composition, previously noted in petrographic study. Based on the cationic parameter criteria of Debon and Le Fort (1982), a compositional range from granite to tonalite is evident for samples with SiO_2 contents varying between 59 and 77 wt.% (Fig. 4.6a). In spite of this variation, the whole suite is consistently peraluminous, as evidenced by values of Al-(K+Na+2Ca) greater than 0 (Fig. 4.6b). This is also consistent with the A/NK-A/CNK criteria of Maniar and Piccoli (1989) and with petrographic observations that show muscovite ± biotite ± garnet assemblages without amphibole or primary titanite. A number of samples have a leucocratic character due to low Fe+Mg+Ti values (Fig. 4.6b), and according to the modified alkali-lime index (MALI) of Frost and Frost (2008), the tonalites and granodiorites are mainly calcic to calc-alkalic in character, while the granites vary from calc-alkalic to alkalic (Fig. 4.6d). Owing to these compositions, most of the tonalites and granodiorites tend to plot within the I-type field of the modified ACF diagram, while the granites plot within the S-type field (Fig. 4.6c).

The REE patterns of granites are characterized by relatively high contents of LREEs and conspicuous negative Eu anomalies (Eu/Eu* ratios between 0.1 and 0.8), although some samples with rather low REE contents tend to lack these anomalies (Eu/Eu* >0.8). Fractionation is moderate to high, as inferred from rather flat HREE patterns and $(La/Yb)_N$ ratios between 10 and 200 (Fig. 4.7a). Two samples of muscovite-albite pegmatite representing the most differentiated phases of the Aurumina Suite, display the lowest amounts of REEs (less than 10 times the amount of reference chondrite) along with a poorly fractionated pattern ($[La/Yb]_N$ ratios between 3 and 5) and a negative Eu anomaly (Fig. 4.7a). The tonalites and granodiorites tend to be less enriched in LREEs compared to the granites and show small negative Eu anomalies, with some positive anomalies in some samples (Eu/Eu* ratios between 0.5 and 2). As in the case of the granites, fractionation is rather moderate with flat HREE patterns and $(La/Yb)_N$ ratios between 6 and 77, with one sample having a value as high as 172 (Fig. 4.7b).

Table 4.1. Whole-rock major and trace element data. Empty entries correspond either to values below detection limits, or unanalyzed elements. Major oxides in wt.% and trace elements in ppm.
AS Gr: Aurumina Suite Granite; **AS T/G**: Aurumina Suite Tonalite-Granodiorite; **NR P**: Nova Roma Plutons; **Arr P**: Arraias Plutons; **CdS M.T**: Colinas do Sul Metaluminous Tonalitic Rocks; **CdS M**: Colinas do Sul Mafic Rocks.

* Samples of muscovite-albite pegmatites representing the most evolved phases of granites, and therefore included in the latter group despite being chemically equivalent to tonalites.

Sample	Rock Type	Location Lat. (S)	Location Long. (W)	SiO_2	TiO_2	Al_2O_3	Fe_2O_3	MnO	MgO	CaO	Na_2O	K_2O	P_2O_5	LOI	TOT/C	TOT/S	Sum	La	Ce	Pr	Nd	Sm	Eu	Gd	Tb	Dy	Ho	Er	Tm	Yb	Lu	Ba	Nb	Rb	Sn	Sr	Ta	Th	U	Y	Zr	Cr	Ni
95-II-111	AS Gr	13°42'20.2"	47°12'36.6"	75.07	0.34	14.25	1.21		0.49	0.35	2.04	5.18	0.25	1.7			100.86															492	15.0			107.0				9.0	167.0			
98-II-17	AS Gr	13°46'5.5"	47°22'35.7"	64.89	1.06	15.23	3.77		2.66	1.86	2.65	4.03	0.50	3.2			99.83															615	8.0	283.0		10.0				11.0	562.0	10.26		
98-II-187	AS Gr	13°42'5.9"	47°19'21.4"	69.19	0.61	16.08	2.51	0.02	1.54	1.03	3.28	4.14	0.57	1.2			100.14															561	11.0	280.0		80.0				10.0	400.0	2.74		
98-III-40	AS Gr	13°42'13.3"	47°24'38.0"	72.57	0.22	14.89	2.24	0.02	1.24	0.47	2.97	3.25	0.24	1.8			99.93															199	9.0	186.0		34.0				4.0	99.0	7.53		
98-V-58	AS Gr	13°51'6.8"	47°30'39.0"	70.54	0.94	15.63	2.49	0.02	0.98	0.28	1.93	4.25	0.39	2.7			100.11															333	10.0	268.0		49.0				19.0	381.0	1.37		
98-VII-6b	AS Gr	13°46'20.4"	47°35'12.7"	69.21	0.66	16.17	2.89	0.03	1.37	0.76	3.49	3.28	0.57	1.5			99.97															213	20.0	280.0		9.0				9.0	48.0	10.95		
99-V-81	AS Gr	13°21'26.8"	46°56'4.7"	72.20	0.45	15.04	2.35	0.02	0.59	0.72	1.89	4.62	0.44	1.0			99.36															528				89.0				13.0	374.0	2.05		
99-VII-139	AS Gr	13°14'45.1"	46°51'53.6"	70.80	0.20	17.57	1.58	0.01	0.53	1.03	4.03	4.13	0.15	0.5			100.51															314				91.0				4.0	183.0	3.42		
99-VIII-18a	AS Gr	13°10'25.4"	46°55'3.2"	73.00	0.31	15.16	2.57	0.02	0.81	1.30	3.52	2.99	0.15	0.5			100.36															693				211.0				7.0	126.0	9.58		
99-VIII-52	AS Gr	13°14'21.8"	46°50'59.5"	73.00	0.12	16.00	1.12	0.01	0.35	1.03	3.99	3.60	0.17	0.8			100.15															280				78.0				3.0	182.0	2.05		
99-VIII-56	AS Gr	13°13'18.4"	46°51'24.0"	73.68	0.12	14.62	1.14	0.02	0.27	0.90	3.79	4.09	0.15	0.8			99.57	13.0	22.0			2.30	2.00		0.50																		
PB-199a	AS Gr	13°41'35.2"	46°57'44.4"	73.57	0.28	14.54	1.84	0.01	0.33	0.27	2.87	5.20	0.16	0.6	0.04		99.71	50.9	106.2	13.04	50.0	8.80	0.55	4.45	0.46	1.92	0.35	0.85	0.14	0.91	0.12	481	9.2	368.2	5	86.3	1.1	40.7	4.1	12.9	163.6		2.3
AU10	AS Gr	13°35'55.5"	47°03'26.7"	66.80	0.82	15.85	3.53	0.03	0.96	1.54	3.35	4.78	0.58	1.4			99.59	153.0	341.0				1.00									622	11.0	280.0	4	180.0		116.0	6.0	17.0	428.0			
CAV-2	AS Gr	13°48'7.6"	47°35'49.8"	75.18	0.10	14.78	0.96	0.03	0.25	0.69	4.20	2.72	0.24	0.9	0.03		100.08	10.3	18.5	2.30	8.7	1.90	0.42	2.06	0.30	1.31	0.21	0.61	0.10	0.64	0.16	124	6.3	218.4	6	79.2	1.7	2.9	10.6	8.8	39.9		1.3
TEREZZI 2	AS Gr	13°46'19.1"	47°16'43.7"	70.16	0.25	16.03	1.51	0.01	0.34	0.45	2.31	6.66	0.40	1.2	0.05		99.37	70.2	130.3	17.62	67.5	12.50	0.62	6.56	0.68	2.62	0.31	0.91	0.13	0.85	0.14	467	9.4	414.8	6	137.3	0.8	36.6	18.4	15.9	145.2	6.84	1.5
01-IV-217	AS Gr	12°54'23.2"	46°53'8.0"	70.46	0.45	14.94	1.98	0.01	0.64	0.67	1.87	6.52	0.45	1.8			99.79	67.6	154.4	20.35	73.8	13.60	0.60	5.60	0.53	1.65	0.13	0.31	0.05	0.43	0.03	378	4.6	315.8		102.9	0.3	54.7	9.1	6.3	200.6		2.0
TF05-I-03b	AS Gr	13°15'9.9"	47°09'5.5"	71.97	0.23	15.31	1.63	0.01	0.40	0.29	2.85	5.59	0.13	1.1			99.51	21.4	45.3	4.85	17.1	3.20	0.76	2.46	0.23	0.72	0.10	0.47	0.08	0.51	0.13	560	2.8	147.3	2	278.6	0.5	8.1	2.9	4.1	59.9		4.2
TF05-IX-145b	AS Gr	13°35'32.4"	47°03'25.6"	73.39	0.11	14.94	1.24	0.01	0.30	0.49	3.06	4.85	0.27	1.2			99.86	9.4	22.2	2.41	8.2	2.30	0.37	1.84	0.23	1.17	0.11	0.24		0.38	0.04	292	7.7	201.0	2	62.6	1.7	3.6	3.1	4.4	41.0		0.5
TF05XIII146A	AS Gr	13°42'35.3"	46°58'3.0"	73.77	0.21	14.54	1.21	0.03	0.24	0.33	3.21	5.25	0.17	1.0			99.96	34.7	85.8	9.93	35.8	6.60	0.44	4.15	0.47	2.45	0.35	0.85	0.16	0.97	0.12	382	10.5	365.6	8	61.6	2.3	29.0	6.4	10.5	117.3		2.2
TF05-IX-142	AS Gr	13°35'55.5"	47°03'26.7"	73.63	0.54	13.20	2.49	0.01	0.49	0.39	1.93	5.62	0.32	1.2			99.82	132.3	346.9	36.53	126.9	16.90	0.99	6.66	0.76	2.14	0.30	0.88	0.13	0.56	0.09	947	8.3	320.2	1	67.4	0.8	101.7	7.3	12.3	413.8		2.0
TF05-IX-145a	AS Gr	13°35'32.4"	47°03'25.6"	70.56	0.51	15.19	2.41	0.03	0.57	0.74	2.35	5.27	0.44	1.3			99.37	95.1	181.7	27.33	100.9	18.30	0.79	7.79	0.64	2.53	0.30	0.60	0.10	0.64	0.10	479	6.9	339.0	1	98.9	0.7	79.9	12.9	11.8	262.1		4.8
TF05-VIII-004	AS Gr	13°29'48.3"	47°00'30.6"	70.56	0.49	14.24	3.15	0.02	0.39	1.00	2.61	5.67	0.15	1.3			99.58	335.2	652.3	65.33	213.0	25.30	1.60	11.92	1.45	4.90	0.73	1.83	0.25	1.13	0.21	1226	20.5	250.2	1	111.8	1.5	97.1	4.4	30.6	480.6		2.0
01-I-36	AS Gr	13°00'32.9"	46°52'58.2"	71.87	0.19	15.38	1.23	0.02	0.32	0.74	3.41	5.33	0.28	1.1			99.87	19.6	41.4	4.92	16.9	3.60	0.67	2.66	0.32	1.11	0.14	0.29	0.03	0.18	0.02	466	5.9	251.6	4	133.6	0.7	6.2	8.9	4.6	61.1		3.0
01-I-37	AS Gr	13°00'40.0"	46°53'10.6"	68.60	0.36	16.59	1.86	0.02	0.57	0.93	3.14	5.97	0.33	1.4			99.77	46.5	103.8	12.63	44.2	9.20	0.97	5.35	0.53	1.83	0.20	0.42	0.08	0.42	0.04	686	5.3	251.9	3	162.9	0.8	31.3	6.4	7.4	163.9	4.79	4.0
AB-9A	AS Gr	13°13'21.7"	46°51'32.1"	72.65	0.14	15.34	1.15	0.02	0.29	0.95	4.07	4.54	0.18	0.7			100.03	13.5	26.8	3.13	11.3	2.67	0.52		0.35	1.20	0.16	0.43	0.06	0.29		278	7.2	268.6	18	113.0	2.7	3.6		5.7	60.0		
AB-2B	AS Gr	13°14'15.4"	46°51'43.9"	70.55	0.19	16.19	1.44	0.01	0.45	0.93	3.81	5.15	0.18	1.2			100.06	24.8	50.1	5.91	20.9	4.83	0.67		0.51	1.64	0.20	0.48	0.06	0.32		398	8.6	216.9	12	132.0	2.9	7.4		6.5	85.0		
CAV-8A	AS Gr	13°50'43.1"	47°30'50.8"	68.21	0.89	15.76	4.74	0.06	1.20	0.48	1.51	4.62	0.17	1.9	0.08	0.01	99.63															713										13.68		
95-II-139	AS Gr	13°44'23.9"	47°15'32.4"	75.96	0.13	13.09	0.99		0.80	0.52	3.42	4.67	0.11	1.0			100.65															239	10.0			35.0				10.0	65.0			
AU9B	AS Gr	13°36'18.6"	47°03'17.8"	68.82	0.59	15.63	2.35	0.01	0.83	1.34	2.02	6.21	0.54	2.1			100.40	107.0	244.0													518	8.0	310.0	3	144.0		106.0	11.0	9.0	274.0		
AU9A	AS Gr	13°36'18.6"	47°03'17.8"	71.60	0.29	13.70	1.59	0.01	0.57	1.42	2.41	5.88	0.32	1.9			99.64	55.0	100.0													446	4.0	253.0		140.0		27.0	9.0	4.0	177.0	3.42	2.0
RE 01-AR22c	AS Gr	12°49'52.0"	47°12'29.2"	72.25	0.32	14.86	1.89	0.01	0.47	0.41	1.92	5.66	0.26	1.8			99.85	35.0	74.0		40.0	7.00		5.00		2.00						555	11.0	199.0	2	148.0		23.0	7.0	9.0	126.0		2.0
NR32	AS Gr	13°44'58.0"	46°53'14.7"	67.80	0.42	15.00	3.32	0.04	1.30	2.11	3.09	4.98	0.38	1.4			99.79		67.2				1.22							1.01		1922	11.4	150.0		411.0				15.3	102.0	26.00	17.8
AUFC-14-1	AS Gr*	13°07'38.0"	46°48'34.3"	74.70	0.02	15.44	0.70	0.04	0.07	0.41	5.54	1.92	0.38	0.7			99.92	1.4	2.4	0.23	0.7	0.29	0.04	0.25	0.05	0.35	0.05	0.18	0.04	0.21	0.02	62	13.0	253.4	29	53.5	3.6	1.0	3.2	2.1	15.4		0.4
AUFC-26-1	AS Gr*	11°37'5.8"	47°45'26.8"	74.65		15.03	0.55	0.04	0.03	0.18	4.96	3.44	0.13	1.0			100.01	1.7	3.5	0.37	1.3	0.47	0.03	0.44	0.13	0.75	0.11	0.31	0.06	0.32	0.05	16	9.2	275.0	7	15.8	1.9	1.9	11.2	4.0	23.4		0.3
AUFC-1-1	AS Gr	13°22'25.1"	47°04'17.4"	76.42	0.03	13.84	0.40	0.01	0.11	0.71	3.25	4.36	0.17	0.6			99.90	4.8	8.7	1.01	3.8	0.80	0.28	1.00	0.17	0.81	0.14	0.33	0.04	0.24	0.03	340	6.0	176.9	6	93.2	0.9	1.9	7.9	4.6	24.9		0.5
AUFC-1-2	AS Gr	13°22'25.1"	47°04'17.4"	74.14	0.06	14.80	1.00	0.02	0.18	0.76	3.47	4.45	0.16	0.8			99.84	10.2	19.6	1.99	6.7	1.63	0.35	1.44	0.29	1.40	0.23	0.56	0.09	0.42	0.06	201	10.0	235.9	9	72.2	1.4	3.3	39.4	7.4	38.0		0.6
AUFC-1-5	AS Gr	13°22'25.1"	47°04'17.4"	72.62	0.20	15.01	1.71	0.02	0.43	0.97	3.79	4.29	0.15	0.7			99.89	18.2	38.0	4.09	14.3	3.12	0.42	2.51	0.30	1.07	0.18	0.47	0.06	0.38	0.06	279	5.5	231.9	2	97.6	0.7	6.3	4.9	5.3	90.1		3.5
AUFC-2-1	AS Gr	13°02'17.2"	46°59'53.3"	68.38	0.65	16.46	2.86	0.02	0.65	0.21	1.39	6.47	0.26	2.4	0.04		99.79	105.8	244.5	35.39	143.9	20.79	0.91	9.21	0.82	2.85	0.39	0.92	0.13	0.83	0.10	764	6.2	358.9	2	133.6	0.3	99.3	18.6	16.1	411.4		2.4
AUFC-11-2	AS Gr	13°22'58.6"	46°55'41.9"	66.03	0.37	18.64	1.71	0.01	0.45	0.92	2.88	7.09	0.37	1.4			99.87	40.8	98.3	11.77	46.1	9.19	0.52	5.79	0.56	1.85	0.18	0.37	0.06	0.39	0.04	325	9.1	346.1	2	103.1	0.4	25.2	11.4	7.4	102.2		0.6
AUFC-13-3	AS Gr	13°14'22.1"	46°50'58.0"	74.59	0.11	14.69	0.91	0.01	0.20	0.55	3.50	4.55	0.27	0.6			99.98	9.8	21.1	2.36	9.6	2.43	0.28	1.77	0.24	0.94	0.08	0.22	0.02	0.13	0.02	166	7.1	307.6	17	56.9	1.8	3.6	5.3	3.0	43.1	13.68	0.4
AUFC-18-1	AS Gr	13°19'22.5"	46°59'35.5"	73.81	0.12	14.71	1.04	0.02	0.31	0.49	3.53	4.81	0.15	0.9			99.89	16.2	34.2	4.13	15.7	3.98	0.46	3.20	0.35	1.35	0.16	0.40	0.06	0.34	0.04	259	2.2	180.7	1	127.7	0.1	5.6	3.6	5.1	42.1		3.0
AUFC-22-1	AS Gr	13°41'54.0"	47°18'15.2"	69.12	0.62	15.61	2.19	0.03	0.60	0.82	2.95	6.01	0.53	1.2			99.68	120.8	331.2	42.52	165.0	21.98	0.72	8.51	0.73	2.64	0.24	0.69	0.09	0.58	0.07	471	6.7	324.6	8	130.6	0.4	156.7	11.3	10.2	419.9		2.0
AUFC 24-1	AS Gr	11°57'59.1"	47°35'16.9"	72.92	0.24	14.57	1.67	0.02	0.43	0.45	3.02	5.22	0.19	1.1			99.83	72.0	191.9	21.49	81.8	13.49	0.75	7.82	0.84	3.57	0.57	1.57	0.22	1.48	0.19	409	10.9	407.9	6	51.9	1.3	51.7	16.6	19.1	162.6		1.2
AUFC 32-1	AS Gr	13°59'23.6"	47°55'43.8"	65.56	0.64	18.95	2.57	0.04	0.73	1.37	2.98	4.79	0.48	1.7	0.09		99.90	131.2	324.5	43.05	167.5	24.80	1.75	11.72	1.14	5.12	0.76	2.29	0.33	2.10	0.25	434	11.6	304.2	11	62.6	2.2	130.2	20.5	27.4	362.9		2.5
AUFC 34-1	AS Gr	14°04'0.4"	48°04'24.4"	69.67	0.56	15.14	2.24	0.02	0.71	0.95	3.25	5.70	0.21	1.3	0.08		99.83	101.2	257.5	31.73	122.7	19.29	0.77	8.87	0.73	2.42	0.20	0.57	0.09	0.61	0.09	732	7.0	289.0	2	154.9	0.4	106.7	8.6	7.9	329.0	13.68	4.4
AUFC 40-1	AS Gr	13°29'48.3"	47°00'30.3"	66.28	1.08	15.58	3.84	0.04	0.89	1.76	3.31	4.94	0.38	1.4	0.08		99.58	230.5	542.6	65.13	236.3	28.21	1.64	11.99	0.98	3.81	0.44	1.16	0.16	0.99	0.14	1401	12.3	281.3	1	197.4	0.4	149.9	8.1	16.4	876.7	20.52	5.8
09-VII-5	AS Gr	13°52'59.5"	48°02'57.8"	70.72	0.23	15.81	2.02	0.04	0.89	1.07	3.55	4.10	0.14	1.3			99.87	22.0	48.6	5.16	18.4	3.73	0.83	2.78	0.37	1.44	0.22	0.56	0.09	0.47	0.08	389	5.8	201.9	3	139.0	0.5	5.7	6.4	7.0	69.3	34.21	18.0
09-IX-50	AS Gr	14°00'37.2"	48°04'1.9"	74.12	0.06	14.62	0.47	0.01	0.14	0.32	2.34	5.60	0.13	2.1	0.04		99.95	7.7	20.1	2.04	8.2	1.46	0.16	0.98	0.14	0.72	0.11	0.36	0.05	0.39	0.04	258	4.2	178.4	1	141.6	0.1	2.2	2.5	4.8	9.6		0.5
09-IX-62	AS Gr	14°03'54.1"	48°04'23.5"	67.80	0.63	15.08	4.09	0.05	1.09	1.64	3.06	5.10	0.51	0.7	0.05		99.80	96.6	160.3	22.62	86.4	14.39	1.57	11.41	1.53	6.91	1.11	2.62	0.31	1.68	0.23	920	15.0	187.0	1	195.8	0.8	29.2	3.1	37.5	322.0	34.21	8.4

Table 4.1. (Continued).

Sample	Rock Type	Location		SiO_2	TiO_2	Al_2O_3	Fe_2O_3	MnO	MgO	CaO	Na_2O	K_2O	P_2O_5	LOI	TOT/C	TOT/S	Sum	La	Ce	Pr	Nd	Sm	Eu	Gd	Tb	Dy	Ho	Er	Tm	Yb	Lu	Ba	Nb	Rb	Sn	Sr	Ta	Th	U	Y	Zr	Cr	Ni
		Lat. (S)	Long. (W)																																							
09-X-61 A	AS Gr	14°06'31.2"	48°07'7.0"	74.58	0.13	14.26	0.87	0.01	0.27	0.74	3.43	4.56	0.13	0.9			99.88	24.2	49.2	5.47	18.7	3.74	0.57	2.77	0.38	1.50	0.22	0.58	0.08	0.44	0.08	473	6.3	225.0	6	149.9	0.9	8.4	5.3	9.5	86.8	13.68	1.0
09-X-122 A	AS Gr	14°05'15.8"	48°04'4.2"	69.27	0.59	15.08	2.57	0.04	0.80	1.17	3.16	5.70	0.18	1.2	0.09		99.85	105.7	283.4	34.38	132.0	21.24	0.87	9.15	0.88	2.69	0.26	0.55	0.09	0.54	0.09	845	8.8	214.8	2	337.9	1.0	102.9	7.7	9.4	341.2	27.37	8.6
09-XII-53	AS Gr	13°53'53.7"	47°57'7.4"	73.31	0.16	14.91	0.94		0.29	0.65	2.74	5.59	0.24	1.1	0.06		99.99	15.5	35.3	4.20	15.7	3.86	0.68	3.22	0.40	1.34	0.17	0.44	0.06	0.35	0.05	395	5.8	258.2	4	111.6	0.4	6.7	6.7	8.1	72.0		1.1
09-VIII-96 A	AS Gr	13°59'13.9"	48°01'6.8"	72.39	0.13	15.29	1.08	0.02	0.32	0.99	3.72	3.59	0.07	2.2	0.04		99.84	44.8	73.4	7.98	25.9	4.20	0.86	3.27	0.52	2.51	0.42	1.04	0.16	0.98	0.13	666	7.9	136.9	2	186.0	0.7	12.9	18.9	12.7	87.1		1.9
09-XIII-59	AS Gr	13°54'6.4"	47°52'17.2"	76.24	0.07	13.12	0.74		0.17	0.72	3.20	4.51	0.18	1.0	0.06		100.01	4.4	9.3	1.02	3.7	0.95	0.23	0.77	0.11	0.35	0.05	0.14	0.02	0.10	0.02	347	4.7	150.8	2	261.4	0.2	2.1	3.2	1.7	29.1		0.5
TF10-IV.52	AS Gr	12°41'47.3"	47°55'33.0"	75.57	0.13	13.32	0.96	0.02	0.36	0.86	3.36	4.47	0.03	0.8			99.88	17.0	41.9	4.22	15.2	2.38	0.73	1.52	0.23	1.12	0.21	0.56	0.09	0.65	0.09	974	3.3	118.0	1	196.7	0.4	10.3	1.6	6.2	68.8	20.52	1.6
TF10-IV.130	AS Gr	12°43'26.4"	48°03'37.1"	73.27	0.31	13.98	2.46	0.03	0.73	0.82	2.93	4.10	0.09	1.2			99.92	19.8	79.6	6.04	22.8	4.68	0.61	3.26	0.48	2.22	0.43	1.17	0.18	1.32	0.18	423	8.5	198.2		127.4	0.4	17.3	3.0	11.4	140.9	34.20	9.0
TF10-V.52	AS Gr	12°44'17.6"	48°04'18.8"	72.87	0.16	14.85	1.63	0.05	0.34	0.71	3.20	4.89	0.17	1.1	0.07		100.04	7.9	23.3	2.22	7.6	1.74	0.27	1.45	0.27	1.71	0.36	1.16	0.19	1.38	0.19	258	7.1	243.3	3	106.8	0.8	8.5	5.4	10.9	65.8	34.20	4.6
TF10VII.153C	AS Gr	12°49'0.3"	48°03'32.1"	73.26	0.23	14.15	1.58	0.02	0.40	1.16	3.23	5.09	0.12	0.7	0.02		99.96	27.0	58.5	6.89	24.8	4.92	0.47	4.04	0.60	2.80	0.45	1.09	0.15	0.96	0.14	418	8.5	193.2	1	124.5	0.3	19.3	2.5	14.1	100.5	27.36	2.6
TF10-X.74A	AS Gr	12°53'44.7"	47°54'48.5"	74.18	0.17	13.74	1.91	0.03	0.23	1.16	2.75	4.73	0.07	0.9			99.87	38.4	88.4	10.26	36.7	6.91	0.70	5.28	0.84	4.55	0.85	2.38	0.35	2.18	0.32	1081	8.4	166.5	3	112.0	0.5	17.2	2.9	22.9	126.0		2.8
TF10XIV.80A	AS Gr	13°01'58.1"	47°50'1.3"	73.12	0.18	15.81	1.30	0.03	0.34	0.18	3.50	2.97	0.22	2.3	0.05		100.00	18.0	41.4	4.83	18.5	4.40	0.90	3.79	0.48	1.90	0.25	0.57	0.07	0.47	0.06	416	3.1	87.9	2	114.3	0.2	7.8	3.4	8.6	88.3	34.20	2.3
98-III-38	AS T/G	13°38'42.6"	47°25'44.1"	68.79	0.27	16.91	2.31	0.04	0.96	1.71	4.16	3.05	0.60	1.5			100.31															582	7.0	180.0		186.0				10.0	158.0	14.37	10.0
98-VII-121	AS T/G	13°45'29.3"	47°36'19.2"	71.33	0.79	15.64	1.18	0.02	0.41	0.54	3.79	2.88	0.17	2.5			99.27															309	5.0	162.0		104.0				8.0	72.0		
98-VIII-11	AS T/G	13°43'56.1"	47°36'6.1"	71.19	0.42	15.47	2.34	0.03	1.08	1.14	5.50	1.59	0.17	1.0			99.96															339	4.0	78.0		298.0				6.0	96.0	3.42	
98-VIII-103	AS T/G	13°42'33.8"	47°36'55.5"	76.98	0.81	12.06	2.08	0.04	0.62	0.83	4.83	1.67	0.05	0.0			100.00															394	17.0	20.0		28.0				130.	125.0		
98-VI-7	AS T/G	13°51'21.3"	47°36'2.3"	69.88	0.24	17.30	1.36		1.54	2.05	5.16	1.13	0.10	1.0			99.73															234	2.0	24.0		549.0				2.0	57.0	2.74	
99-VII-41	AS T/G	13°15'2.9"	46°50'5.7"	72.30	0.13	15.64	1.45	0.02	0.60	2.20	5.25	0.56	0.06	1.0			99.19															235	0.0	0.0		377.0				2.0	161.0	3.42	
99-VIII-208	AS T/G	13°12'10.4"	46°48'27.9"	63.00	0.80	16.69	5.40	0.07	1.68	3.16	3.32	3.57	0.25	1.6			99.53	45.0	81.0		41.0	5.90	1.00	0.50								1061	14.0	130.0		349.0	2.1	8.0	2.0	15.0	312.0	17.79	
01-AR22	AS T/G	12°49'52.0"	47°12'29.2"	71.76	0.31	14.39	2.51	0.05	0.82	2.83	3.98	1.75	0.07	1.3			99.77	23.0	52.0		22.0	4.00		3.00		2.00		1.00				653	4.0	52.0	2	351.0		5.0	2.0	13.0	105.0		4.0
MALEG 2	AS T/G	13°12'8.2"	46°48'24.4"	62.48	0.85	16.73	5.68	0.06	1.76	4.00	3.31	3.14	0.29	1.3	0.15		99.75	36.3	47.2	5.91	25.1	4.10	1.75	4.18	0.58	3.03	0.63	1.61	0.23	1.33	0.21	860	15.1	152.7	3	319.1	1.4	3.6	1.1	20.2	284.8	13.68	33.8
99-VII-15	AS T/G	13°16'38.1"	46°50'13.3"	66.10	0.64	15.69	4.72	0.05	1.35	2.25	3.48	3.33	0.22	2.0	0.16	0.01	100.00	63.1	113.2	13.32	51.3	9.40	1.41	5.90	0.78	3.89	0.70	1.87	0.27	1.45	0.22	645	14.3	216.0	2	249.3	2.2	19.6	4.3	21.2	246.6	13.68	24.3
MALEG 6A	AS T/G	13°18'46.1"	46°56'20.6"	69.48	0.22	16.33	2.01	0.04	0.64	3.29	4.98	1.01	0.08	1.7	0.02		99.80	23.9	46.2	5.52	23.9	5.00	1.36	4.36	0.68	4.01	0.75	2.36	0.32	2.36	0.37	278	6.3	41.4		267.6	0.6	3.2	0.7	25.4	131.6		5.7
MENDES 2	AS T/G	13°20'0.2"	47°03'13.4"	73.29	0.11	14.68	1.00	0.02	0.23	0.57	3.97	4.17	0.15	1.5		0.02	99.71	17.6	33.9	3.59	14.3	3.40	0.84	3.55	0.51	2.00	0.28	0.50	0.08	0.44	0.05	335	11.7	279.8	6	129.2	2.1	3.5	4.4	10.1	47.0		1.7
CAV-6B	AS T/G	13°44'2.1"	47°38'20.7"	72.71	0.10	15.80	0.87	0.02	0.23	1.36	5.06	2.37	0.12	1.3	0.05		99.99	9.4	13.3	2.09	7.4	1.80	1.15	1.75	0.21	0.75	0.08	0.12		0.12	0.03	539	5.5	93.6	3	229.8	1.2	3.2	2.4	2.8	26.7		1.9
AB-04A	AS T/G	13°07'46.9"	46°48'47.4"	72.68	0.10	15.65	1.11		0.33	1.77	6.33	0.85	0.03	0.7			99.53	4.0	5.0			0.80	1.00									343	8.0	36.0		405.0	0.9		0.6	8.0	70.0	3.42	
01-VII-05	AS T/G	12°46'54.1"	47°02'54.8"	69.29	0.34	15.25	3.01	0.06	0.83	2.02	3.66	3.62	0.04	1.4			99.52	17.6	38.5	4.56	16.0	3.30	0.93	2.80	0.41	2.22	0.42	1.15	0.14	0.90	0.12	1393	6.6	89.0	1	429.0	1.0	7.6	0.9	13.0	94.0	28.05	11.0
01-VII-26	AS T/G	12°50'19.7"	47°03'41.4"	65.25	0.64	16.43	4.48	0.06	1.60	4.10	3.35	2.01	0.13	1.6			99.65	23.4	43.5	5.07	18.2	2.30	1.06	2.30	0.24	1.34	0.26	0.81	0.09	0.78	0.11	452	6.1	83.0		473.0	0.6	3.0	0.1	7.8	180.0	23.26	7.0
01-VIII-001	AS T/G	12°45'20.0"	47°02'39.3"	70.44	0.34	15.49	2.70	0.04	0.76	3.04	4.40	1.34	0.06	1.1			99.71	32.0	58.8	6.68	27.5	5.00	0.84	3.65	0.49	2.40	0.42	1.24	0.17	1.04	0.15	180	6.6	57.0	2	429.0	0.6	8.8	0.7	13.0	131.0	8.89	3.0
01-VIII-126	AS T/G	12°44'36.4"	47°03'30.2"	71.17	0.29	15.21	2.45	0.04	0.58	2.77	4.34	1.48	0.06	1.2			99.59	26.8	50.8	5.74	22.1	3.70	0.91	2.69	0.29	1.30	0.20	0.49	0.07	0.44	0.06	485	5.7	50.0		408.0	0.5	8.8	2.3	6.0	130.0	8.89	3.0
01-III-85	AS T/G	12°56'9.3"	46°52'33.0"	61.58	1.17	17.28	5.56	0.05	1.69	4.80	3.75	1.47	0.43	1.9			99.68	35.0	71.6	8.74	32.4	4.90	1.91	3.38	0.35	1.36	0.22	0.47	0.05	0.40	0.05	866	14.6	72.5		735.0	0.5	2.1	0.6	6.8	431.3	9.58	8.0
01-II-62	AS T/G	12°58'15.7"	46°52'39.1"	72.73	0.19	15.54	1.60	0.03	0.51	1.84	5.09	1.21	0.05	1.1			99.89	5.9	12.8	1.37	5.6	1.60	0.45	1.78	0.34	2.02	0.34	0.96	0.12	0.70	0.10	83	9.9	70.9	1	245.6	1.4	0.8	1.5	12.1	61.9	20.53	5.0
01-V-153	AS T/G	12°50'30.4"	46°51'9.1"	64.87	0.52	16.47	4.78	0.10	2.30	4.25	2.87	2.10	0.13	1.3			99.69	37.0	72.9	8.37	29.6	5.70	1.21	4.14	0.57	3.60	0.78	2.25	0.35	2.10	0.31	581	5.9	104.0	2	436.0	0.6	11.1	2.6	23.0	150.0	46.53	19.0
TF05-I-043	AS T/G	13°12'39.3"	47°09'57.5"	71.23	0.18	16.33	1.47	0.02	0.65	2.03	5.78	1.22	0.06	1.0			99.97	4.4	9.1	0.99	4.1	0.70	0.29	0.75	0.07	0.29	0.07			0.22	0.02	168	2.0	50.1		585.1	0.3	0.9	0.3	1.7	79.7		7.4
TF05-I-220	AS T/G	13°12'56.4"	47°08'42.6"	70.77	0.47	15.39	2.69	0.03	0.68	1.68	4.57	2.33	0.21	1.1			99.92	55.9	107.0	11.24	34.5	4.50	1.05	2.50	0.29	1.11	0.22	0.34	0.07	0.22	0.04	459	9.2	138.2	2	264.8	0.8	16.8	3.9	5.9	238.8		3.0
TF05-XI-064	AS T/G	13°33'39.4"	46°58'31.7"	73.96	0.19	14.23	2.52	0.04	0.43	0.80	5.31	1.64	0.07	0.8			99.99	22.8	47.4	5.03	19.4	3.40	0.32	3.18	0.54	2.37	0.51	1.69	0.29	1.76	0.24	193	9.6	153.0	2	148.5	0.8	4.3	0.7	19.9	103.0		4.4
TF05-XIV-326	AS T/G	13°44'59.7"	46°54'39.1"	62.58	0.66	16.91	5.23	0.08	2.37	3.84	3.52	2.83	0.17	1.5			99.69	52.1	109.9	12.08	41.2	6.90	1.38	4.74	0.70	4.32	0.69	1.71	0.27	1.69	0.21	861	10.1	105.7	2	415.0	1.0	12.6	1.8	20.8	204.3		32.7
TF05-XIV-076	AS T/G	13°44'54.8"	46°54'57.9"	66.85	0.57	16.10	4.05	0.07	1.51	2.37	3.92	2.85	0.15	1.3			99.74	32.9	64.4	6.59	26.2	4.60	1.17	3.84	0.62	3.26	0.58	1.93	0.27	1.55	0.25	740	5.8	95.1	2	413.5	1.1	8.6	1.7	19.1	140.0		5.1
AUFC-4-1	AS T/G	13°05'53.1"	47°10'2.3"	72.97	0.16	15.10	1.99	0.04	0.43	2.11	4.42	1.75	0.07	0.9			99.94	21.7	41.3	4.47	16.8	2.53	0.70	2.15	0.25	1.18	0.27	0.82	0.13	0.84	0.12	140	4.1	85.1	1	287.6	0.4	7.2	3.2	7.4	123.1		1.0
PR-77C	AS T/G	13°04'15.3"	47°16'37.7"	59.42	1.16	16.37	7.79	0.11	2.91	4.29	3.11	2.83	0.37	1.4	0.05		99.81	47.3	93.1	9.51	32.6	5.20	1.27	4.41	0.56	2.69	0.53	1.33	0.21	1.22	0.21	907	16.6	128.2	2	426.5	0.6	8.9	2.2	13.8	279.4	41.04	16.8
AUFC 29-1	AS T/G	13°53'17.1"	48°03'37.0"	70.05	0.24	16.14	2.97	0.03	0.96	1.12	3.80	3.23	0.19	1.2			99.93	22.8	53.2	5.45	20.2	4.32	0.75	3.38	0.46	1.86	0.25	0.53	0.06	0.36	0.06	239	15.5	204.7	4	144.3	1.2	10.3	26.6	8.0	105.8	34.20	16.5
AUFC 41-1	AS T/G	13°14'55.2"	47°08'35.7"	74.01	0.34	14.07	2.01	0.03	0.67	0.79	3.33	2.84	0.19	1.6	0.04		99.92	48.1	100.9	11.04	39.2	7.12	1.09	4.52	0.38	1.55	0.17	0.44	0.06	0.42	0.04	437	3.0	107.4	1	197.9	0.2	19.8	3.3	6.6	192.6	20.52	8.6
AUFC 42-1	AS T/G	13°18'46.4"	46°56'20.2"	71.45	0.21	15.99	1.95	0.03	0.63	3.20	4.95	1.02	0.05	0.4			99.88	5.5	11.2	1.23	5.1	1.02	0.36	0.97	0.14	0.81	0.16	0.42	0.07	0.39	0.07	276	1.4	44.6		512.8	0.2	1.4	0.6	3.8	93.9	13.68	4.2
09-VIII-110	AS T/G	13°58'17.0"	48°06'39.4"	72.69	0.24	14.81	1.64	0.03	0.54	1.14	4.18	3.38	0.09	1.1	0.10		99.94	45.8	71.5	7.67	26.2	3.65	0.77	2.33	0.30	1.25	0.22	0.58	0.09	0.52	0.08	582	6.1	179.2	2	176.5	0.6	15.5	3.3	7.7	136.9	20.53	2.0
09-XIV-51	AS T/G	14°06'53.1"	47°59'42.7"	72.70	0.20	14.69	1.74	0.04	0.58	2.66	4.20	1.71	0.14	1.2	0.03		99.89	24.8	51.1	5.69	21.6	3.89	1.00	2.58	0.37	1.80	0.32	0.91	0.14	0.77	0.12	378	3.2	59.8	2	445.4	0.3	6.5	1.6	9.2	88.8	13.68	2.5
09-XIII-137	AS T/G	13°48'12.1"	47°54'1.9"	72.16	0.20	15.80	1.71	0.02	0.68	2.46	5.37	0.94	0.06	0.5			99.90	7.6	16.0	1.84	7.7	1.42	0.38	1.15	0.18	1.03	0.20	0.53	0.08	0.55	0.08	273	2.4	43.6	1	605.1	0.2	1.4	0.2	5.7	74.0	27.37	8.5
09-X-122 B	AS T/G	14°05'15.8"	48°04'4.2"	59.44	1.00	17.22	6.42	0.10	2.43	4.06	2.77	3.86	0.33	2.1	0.02		99.75	45.4	95.1	10.26	37.7	6.05	1.40	4.61	0.72	3.74	0.70	1.96	0.29	1.75	0.27	785	14.4	245.8	2	466.4	0.6	8.5	2.8	19.6	251.0	34.21	15.8
09-XIII-02	AS T/G	13°55'17.3"	47°53'31.8"	72.72	0.11	15.87	0.98	0.02	0.34	2.17	6.06	0.99	0.03	0.6			99.89	2.9	6.5	0.77	3.4	0.65	0.21	0.53	0.06	0.18	0.02	0.08		0.09	0.02	250	1.1	28.7		561.5	0.1		0.1	0.9	77.4	27.37	2.6
TF10-IX.167B	AS T/G	12°50'53.5"	48°04'20.2"	73.18	0.22	14.72	2.09	0.04	0.45	1.56	4.62	2.61	0.09	0.4	0.03		100.01	14.8	32.7	3.67	13.4	2.53	0.47	1.98	0.32	1.63	0.32	1.01	0.15	1.07	0.15	230	8.5	112.0	2	161.1	0.5	8.9	1.9	9.4	103.1	20.52	1.5
TF10-IX.163A	AS T/G	12°51'4.8"	48°01'41.3"	63.30	0.57	15.35	6.09	0.19	3.09	4.39	2.54	3.03	0.15	1.1	0.23		100.03	27.6	58.7	6.71	25.2	4.54	1.09	3.81	0.60	3.26	0.69	2.01	0.31	1.95	0.31	606	8.3	149.2	5	211.6	0.5	4.7	0.9	18.9	176.3	164.1	53.9
TF10-V.182A	AS T/G	12°43'41.3"	48°03'48.8"	64.15	0.81	16.14	6.07	0.05	1.87	2.53	3.37	3.30	0.18	1.4	0.12		99.99	41.0	84.6	9.80	35.5	5.69	1.02	3.59	0.47	2.16	0.40	1.10	0.17	1.12	0.16	337	10.6	182.1	17	242.6	0.6	16.0	2.7	11.4	222.6	75.24	28.6
TF10-III.117	AS T/G	12°44'6.4"	48°04'35.0"	68.14	0.54	15.39	4.36	0.05	1.30	2.13	3.37	3.25	0.13	1.2	0.14		100.00	46.1	99.5	11.13	42.4	6.74	1.03	4.00	0.51	2.28	0.40	1.00	0.16	1.02	0.15	386	10.6	201.5		189.1	0.6	20.7	2.5	11.5	223.7	75.24	15.0
TF10-VIII.123	AS T/G	12°47'49.6"	48°00'49.7"	71.05	0.27	14.82	2.92	0.09	0.44	2.51	3.71	2.98	0.11	1.0	0.03		99.93	30.4	75.2	7.31	26.1	3.86	0.82	2.53	0.42	2.56	0.57	1.93	0.32	2.22	0.34	598	8.2	127.7	2	224.2	0.5	18.9	2.2	17.1	223.8	20.52	4.4

Table 4.1. (Continued).

Sample	Rock Type	Location		SiO_2	TiO_2	Al_2O_3	Fe_2O_3	MnO	MgO	CaO	Na_2O	K_2O	P_2O_5	LOI	TOT/C	TOT/S	Sum	La	Ce	Pr	Nd	Sm	Eu	Gd	Tb	Dy	Ho	Er	Tm	Yb	Lu	Ba	Nb	Rb	Sn	Sr	Ta	Th	U	Y	Zr	Cr	Ni
		Lat. (S)	Long. (W)																																								
TF10-VIII.185	AS T/G	12°49'29.0"	48°02'58.2"	69.85	0.36	15.90	2.99	0.03	0.79	2.69	4.84	1.72	0.10	0.7	0.04		100.01	30.2	61.5	6.66	23.2	3.67	0.54	2.80	0.45	2.44	0.45	1.21	0.16	0.90	0.13	91	9.8	148.0	1	206.6	1.2	11.7	4.0	13.7	140.7	13.68	4.7
TF10-X.12	AS T/G	12°53'48.3"	47°54'38.1"	64.48	0.43	17.78	4.77	0.09	0.47	4.09	3.33	3.03	0.13	1.2		0.09	99.89	62.8	125.5	13.67	50.8	7.03	1.85	4.54	0.67	3.20	0.62	1.90	0.28	1.95	0.32	754	11.1	130.7	2	305.6	0.7	15.1	2.3	17.5	363.3	20.52	5.3
TF10-X.45A	AS T/G	12°53'40.0"	47°54'17.6"	64.74	0.43	17.69	4.79	0.10	0.46	4.13	3.31	3.03	0.13	1.0		0.08	99.89	60.0	119.4	13.03	47.3	6.68	1.88	4.61	0.67	3.45	0.68	1.98	0.31	2.13	0.35	750	11.0	127.3	2	301.2	0.7	14.4	2.3	18.7	380.3		5.4
TF10-V.139	AS T/G	12°47'2.0"	48°03'43.5"	69.02	0.55	15.16	4.01	0.02	1.28	2.84	3.56	2.06	0.22	1.2	0.29		100.21	10.7	21.3	2.55	10.3	1.84	0.78	1.74	0.26	1.32	0.24	0.52	0.07	0.43	0.06	223	12.1	118.0	1	276.2	1.0	0.6	1.1	6.6	166.5	34.20	8.6
09-VIII-63	CdS M.T	13°57'54.2"	48°05'41.1"	66.64	0.41	15.73	3.69	0.06	2.33	4.07	4.64	1.60	0.14	0.4			99.71	22.4	43.1	5.13	19.2	3.15	0.98	2.15	0.31	1.61	0.29	0.83	0.12	0.73	0.11	502	3.2	60.8		888.0	0.2	2.1	0.4	8.4	91.9	88.95	32.0
09-X-17	CdS M.T	14°05'36.2"	48°04'20.0"	62.29	1.23	16.88	4.92	0.09	1.84	5.45	4.15	1.88	0.37	0.7	0.03		99.83	36.0	81.8	8.51	31.3	5.20	1.77	4.05	0.65	3.10	0.61	1.70	0.24	1.42	0.22	502	12.4	78.7		670.2	1.0	4.2	0.6	16.4	196.3	13.68	4.7
09-XIV-72	CdS M.T	14°07'58.5"	47°58'18.3"	56.06	1.48	15.25	8.13	0.13	3.68	6.77	2.36	3.07	0.42	2.3	0.27		99.92	42.0	93.9	10.98	43.4	8.27	1.98	6.91	1.13	6.10	1.15	3.23	0.43	2.75	0.41	771	25.4	129.0	2	597.3	1.3	4.3	1.2	31.7	327.5	68.42	66.3
TF05-XII-152	NR P	13°40'25.7"	46°59'9.1"	61.43	0.65	16.81	5.65	0.08	2.95	5.15	3.83	1.59	0.21	1.5			99.85	34.4	71.7	7.87	31.0	5.20	1.36	3.73	0.65	2.95	0.43	1.46	0.24	1.28	0.21	549	5.1	56.0	1	788.0	0.7	5.0	1.2	15.9	135.7		22.5
TF05-XIV-152	NR P	13°46'41.8"	46°54'53.1"	55.55	0.77	13.54	7.44	0.12	9.09	7.44	1.94	2.05	0.27	1.6			99.81	21.4	68.2	10.11	42.9	9.20	1.77	6.65	0.97	4.56	0.81	1.97	0.28	1.75	0.25	574	8.6	80.1		451.7	0.8	0.5	0.8	24.1	77.0		77.1
TF05XV125A	NR P	13°45'2.6"	46°53'21.4"	55.06	1.15	17.80	7.56	0.10	3.96	6.66	3.09	1.89	0.46	2.1			99.83	50.9	108.2	13.13	48.9	9.10	2.33	6.98	0.98	5.03	0.77	1.91	0.25	1.55	0.26	702	9.2	65.5	1	825.4	1.0	7.8	1.9	23.3	109.1		21.2
TF05-VIII-105	NR P	13°32'23.8"	46°59'58.5"	62.07	0.65	16.73	5.21	0.08	2.50	5.18	4.26	1.38	0.24	1.4			99.70	27.4	51.4	6.92	27.2	5.50	1.59	4.47	0.65	2.95				1.42		568	6.9	43.9	3	816.5	0.8	2.1	0.5	18.0	155.8		21.6
AUFC 37-1	NR P	13°45'31.1"	46°54'45.3"	64.06	0.65	15.85	4.99	0.08	2.23	3.74	2.86	3.21	0.17	1.9			99.74	56.2	95.2	10.21	38.5	6.07	1.23	4.60	0.66	3.60	0.71	1.87	0.28	1.79	0.29	900	10.6	114.7	3	422.8	0.7	11.5	1.9	18.6	187.3	68.40	25.1
PB43B	NR P	13°39'1.9"	46°55'54.4"	56.59	0.98	16.92	8.52	0.13	3.99	4.93	2.90	1.40	0.40	2.5			99.28	20.4	47.2													355	10.2	100.8	8	673.9		5.6		17.0	54.5	65.00	36.8
PB16	NR P	13°40'3.8"	46°58'56.4"	60.81	0.69	16.20	5.74	0.09	2.89	4.94	3.99	1.68	0.27	1.7			98.98	32.7	67.9		32.7	3.85	1.37			2.92				1.79		802	6.2	73.5	3	890.0		5.0		18.7	142.7	80.30	31.7
PB54C	NR P	13°40'8.3"	46°56'19.8"	64.53	0.52	16.90	4.18	0.07	2.17	3.32	4.97	2.13	0.18	1.5			100.43	31.5	55.1		24.9	3.51	1.18			1.99				1.30		558	4.8	125.8	20	767.0		3.9		11.6	106.7	38.10	23.6
TF01V74	Arr P	12°51'28.6"	47°02'36.1"	54.76	1.19	18.73	7.67	0.15	2.99	5.83	2.94	2.52	0.36	2.7			99.84	16.3	33.7	4.12	17.2	3.30	1.78	3.13	0.44	2.47	0.51	1.35	0.21	1.43	0.22	260	9.4	116.6	1	497.2	0.6	0.8	1.0	14.8	232.0	28.05	12.0
TF01IV180	Arr P	12°52'30.3"	46°53'12.4"	52.49	0.65	15.46	9.82	0.16	8.50	7.13	1.88	1.19	0.15	2.3			99.73	12.7	26.8	3.36	13.2	2.80	0.89	2.75	0.46	3.49	0.75	2.27	0.35	2.57	0.37	244	2.8	62.8		538.8	0.1	2.2	0.9	22.6	64.4	248.3	64.0
AUFC 43-1	Arr P	12°52'30.3"	46°53'12.4"	52.09	0.74	13.72	11.75	0.19	10.07	5.72	1.89	1.32	0.09	2.0	0.02	0.36	99.96	17.1	36.4	4.00	15.6	3.13	1.01	2.92	0.53	3.42	0.84	2.51	0.38	2.42	0.35	205	2.2	63.9		434.1		4.8	0.5	21.3	51.3	704.5	111.3
01-V-27	Arr P	12°52'21.9"	46°52'52.8"	56.88	0.68	17.18	7.05	0.11	4.38	7.37	2.36	1.47	0.15	2.2			99.83	23.0	45.0	5.19	18.3	4.00	1.14	3.15	0.46	2.72	0.56	1.64	0.26	1.79	0.21	350	5.0	64.0	2	498.0	0.4	5.5	3.0	18.0	74.0	32.16	16.0
TF09XVI063	CdS M	14°03'59.7"	47°53'7.6"	50.20	0.68	15.52	12.22	0.19	7.02	9.84	2.19	0.56	0.11	1.2		0.09	99.82	10.1	22.3	2.46	10.1	2.34	0.80	2.55	0.48	3.04	0.70	2.16	0.34	2.24	0.35	158	3.2	16.1		237.9	0.2	2.6	0.4	19.2	54.2	112.2	49.8
TF09XVI064	CdS M	14°03'34.7"	47°53'58.2"	49.40	1.99	15.50	13.81	0.18	4.50	8.67	2.77	1.16	0.26	1.5			99.74	24.6	54.5	6.52	27.9	5.97	1.76	5.89	1.03	5.65	1.17	3.38	0.51	3.11	0.49	335	12.4	40.4	2	319.4	0.7	5.4	1.2	32.7	170.5	37.63	47.5
TF09IX066	CdS M	14°04'3.3"	48°03'22.5"	48.23	0.40	16.79	10.38	0.18	9.69	11.15	1.16	0.37	0.06	1.3	0.06	0.09	99.86	4.9	11.6	1.53	7.3	1.43	0.89	1.51	0.26	1.47	0.31	0.94	0.13	0.84	0.13	43	1.6	8.6		331.3	0.2			8.7	42.2	149.8	14.0

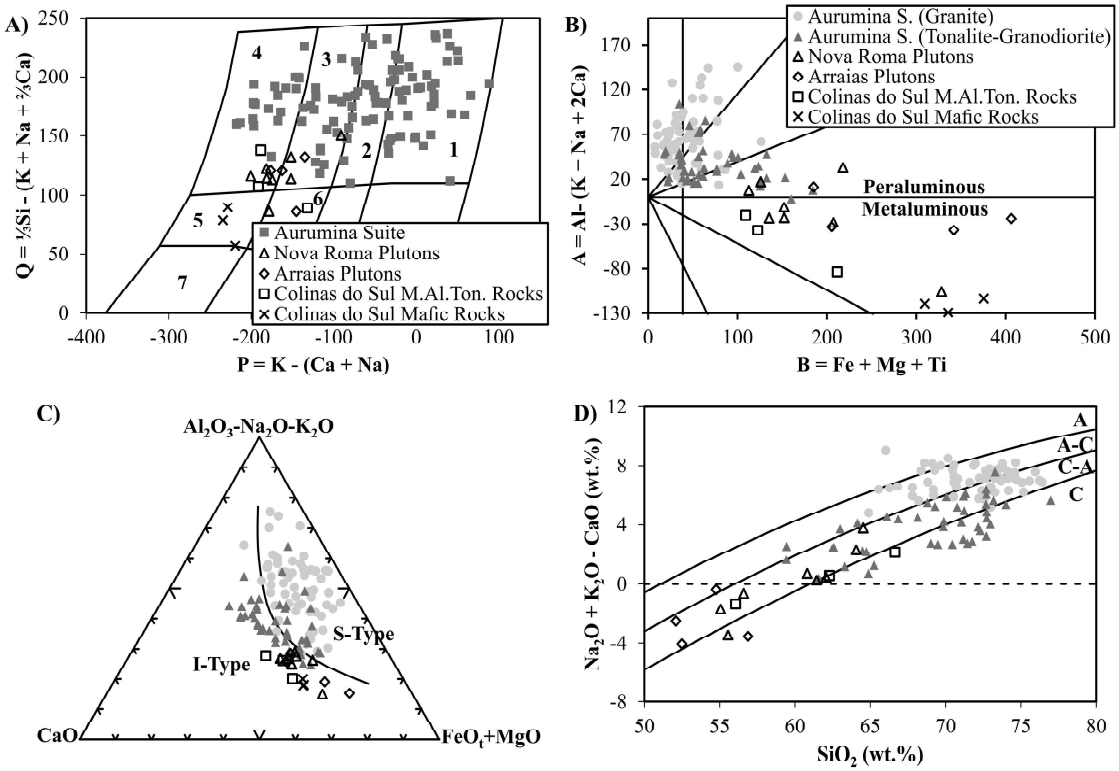

Fig. 4.6. Geochemical features of the analyzed samples. P-Q (**A**) and A-B (**B**) diagrams of Debon and Le Fort (1982). **C**: Modified ACF diagram for discrimination of I- and S-type granitoids of White and Chappell (1977), with boundary adapted by Takahashi *et al.* (1980). **D**: MALI vs. silica diagram of Frost and Frost (2008). M.Al.Ton. = Metaluminous Tonalitic Rocks. Fields in (**A**): 1: granite; 2: monzogranite; 3: granodiorite; 4: tonalite; 5: quartz diorite/quartz gabbro; 6: quartz monzodiorite; 7: gabbro/diorite.

The Nova Roma, Arraias and Colinas do Sul samples display chemical compositions ranging from tonalite to granodiorite and even quartz monzodiorite, with SiO_2 contents varying between 52 and 67 wt.% (Fig. 4.6a). The rocks are characteristically metaluminous, although three samples from Nova Roma and one from Arraias have peraluminous characteristics, possibly due to assimilation of peraluminous host rocks, as these units occur as small bodies and dykes (Fig. 4.6b). The MALI values of these rocks classify them as calcic to calc-alkalic (Fig. 4.6d), and they plot within the I-type field of the modified ACF diagram (Fig. 4.6c). The REE patterns of Nova Roma, Arraias and Colinas do Sul samples are characterized by a moderately fractionated behavior ($[La/Yb]_N$ ratios between 3 and 22), moderate LREE contents, flat HREE trends and slightly negative to no Eu anomalies (Eu/Eu* ratios between 0.7 and 1.2); only one Arraias sample displays a positive anomaly, with a Eu/Eu* ratio of 1.7 (Fig. 4.7c). The HREE contents of Nova Roma and Arraias rocks are ~10 times greater than those of the reference chondrite; these values are slightly higher than the mean HREE contents of the granitic and tonalitic rocks of the Aurumina Suite.

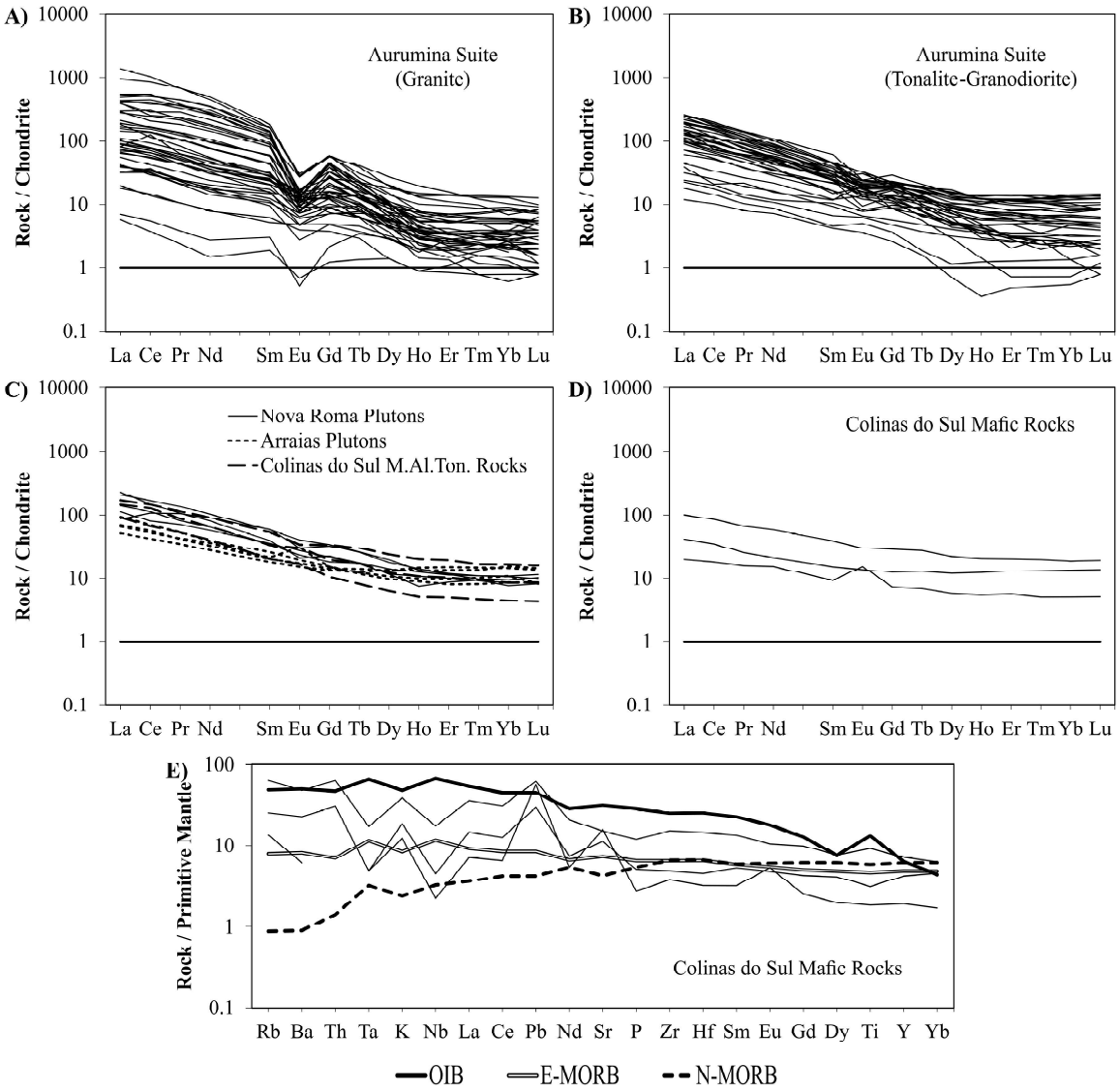

Fig. 4.7. Geochemical features of the analyzed samples. REE patterns of Aurumina Suite granites (**A**) and tonalites-granodiorites (**B**). REE patterns of the Nova Roma and Arraias Plutons (**C**) and the mafic rocks of Colinas do Sul (**D**). The two REE-poorest samples in A correspond to muscovite-albite pegmatites of Au6. Data normalized to chondrite of Evensen *et al.* (1978). **E**: Plot of samples from Colinas do Sul in the multi-element diagram of Sun and McDonough (1989). M.Al.Ton. = Metaluminous Tonalitic Rocks.

The Ni contents of the Nova Roma, Arraias and Colinas do Sul rocks (16-66 ppm) are normally higher than those of the Aurumina Suite rocks (0-34 ppm; one tonalite sample has a value as high as 54 ppm), and one of the Arraias samples has a value of 111 ppm (Table 4.1).

Mafic rocks from Colinas do Sul have SiO_2 between 48 and 50 wt.% and are chemically classified as quartz gabbros (Fig. 4.6a). They are metaluminous in character and have compositions characteristic of I-type rocks (Figs. 4.6b and 4.6d). The samples plot within the tholeiitic trend on the AFM diagram (not shown here) of Irvine and

Baragar (1971) and display E-MORB-type patterns with enrichment of LREEs in relation to HREEs ($[La/Yb]_N$ ratios between 3 and 5) as well as relative enrichment in LILEs (Figs. 4.7d and 4.7e). The Eu anomalies are zero to slightly positive (Eu/Eu* ratios between 0.9 and 1.9), and the HREEs display a flat pattern with contents 8-30 times higher than those of the reference chondrite (Fig. 4.7d).

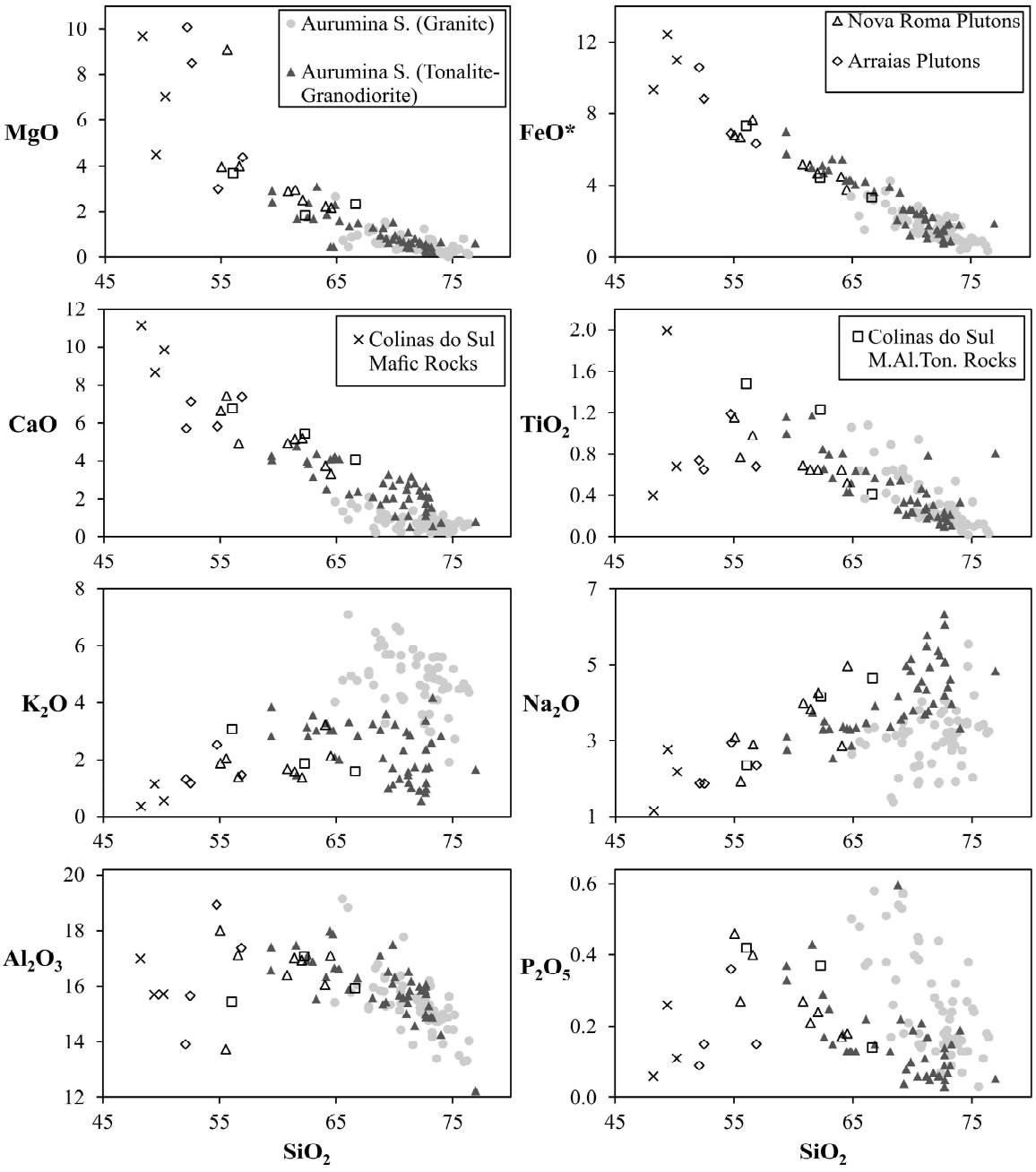

Fig. 4.8. Geochemical features of the analyzed samples: Harker diagrams. M.Al.Ton. = Metaluminous Tonalitic Rocks.

For the aforementioned rock types, global linear to curvilinear trends can be observed in Harker diagrams of MgO, FeO*, CaO and TiO_2 (Fig. 4.8). For K_2O, Na_2O,

Al_2O_3 and P_2O_5, however, clear trends are absent, and samples are arranged in an uncorrelated manner. Instead, samples tend to cluster in compositions characteristic of each rock type. This is the case for the tonalites/granodiorites and granites, which show contrasting positions in the K_2O and Na_2O diagrams, as expected from the definition of these rock types. Even for elements showing some degree of correlation (Mg, Fe, Ca and Ti), a close inspection reveals the lack of a clear differentiation relationship between granites and tonalites/granodiorites, as samples belonging to these groups appear intermixed or in separate clusters. On the other hand, the tonalites/granodiorites of the Aurumina Suite and mafic to intermediate rocks of Colinas do Sul, Nova Roma and Arraias do seem to define more or less consistent trends, although the tonalite/granodiorite data exhibit some degree of scattering at SiO_2 values higher than ~68 wt.% (Fig. 4.8).

4.4.2. U-Pb geochronology

The results of MC-LA-ICP-MS analyses are shown in Table 4.2. We analyzed one sample of Au4 granite (AUFC-40-1), one sample of Au5 granite (AUFC-1-5) and one sample of Au3 tonalite (AUFC-8-1) of the Aurumina Suite, as well as one sample of the Arraias rocks (AUFC-43-1). Cathodoluminescence (CL) imaging was carried out on zircon grains before analysis. The images and ablated spots on the crystals are shown in Appendix I[1].

4.4.2.1.Aurumina Suite granites

The zircon crystals from the granite samples are typically small (60-100 μm), semi-translucent to opaque, and white in color, indicating some degree of metamictization. Rounded borders are a common feature, and length/width ratios vary from 1.5 to 5, with lower values being more representative. In most cases, CL is characterized by a weak intensity, with only a few crystals yielding a bright response. Convoluted zoning is the most common internal structure, although clear oscillatory zoning is also present (Fig. 4.9a). Inherited or xenocrystic cores were identified as a function of their contrasting brightness, shape and internal structures compared to their host crystals (Fig. 4.9b). Mineral inclusions are common within these zircon grains and are generally composed of quartz, feldspar, biotite, muscovite, ilmenite, apatite, monazite and thorite.

[1] Disponível em formato digital no endereço https://www.dropbox.com/s/6of1kj1esopxk24/AppendixI.pdf?dl=0

Table 4.2. MC-LA-ICPMS U-Pb zircon data. Common lead corrections were applied in the calculation of isotope ratios and ages by using measured ^{204}Pb. All errors are reported on a 2σ basis. For each sample, analyses of the 91500 reference zircon that were carried out during the same analytical sessions are included.
f^{206}: fraction of common ^{206}Pb; **c**: core; **r**: rim; **AS Gr**: Aurumina Suite Granite; **AS T**: Aurumina Suite Tonalite; **Arr P**: Arraias Pluton.

Spot	U (ppm)	Th (ppm)	Th/U	f^{206} (%)	$^{206}Pb/^{204}Pb$	Ratio $^{207}Pb/^{206}Pb$	error (%)	Ratio $^{207}Pb/^{235}U$	error (%)	Ratio $^{206}Pb/^{238}U$	error (%)	error corr. (ρ)	Age $^{207}Pb/^{206}Pb$	error (Ma)	Age $^{207}Pb/^{235}U$	error (Ma)	Age $^{206}Pb/^{238}U$	error (Ma)	Concordance (%)
Sample AUFC-40-1 (AS Gr) (13° 29' 48.3" S 47° 00' 30.3" W)																			
ZR1	101	52	0.52	0.15	9637	0.145	1.19	8.803	2.26	0.440	1.92	0.85	2290	20	2318	20	2350	38	102.6
ZR2	583	100	0.17	0.00	835239	0.131	1.21	7.028	2.62	0.389	2.32	0.89	2111	21	2115	23	2120	42	100.4
ZR3	511	41	0.08	0.16	9274	0.130	1.18	7.013	1.75	0.390	1.28	0.73	2102	21	2113	15	2124	23	101.0
ZR4	243	61	0.25	0.24	6151	0.133	1.35	7.145	2.76	0.390	2.40	0.87	2134	23	2130	24	2125	43	99.6
ZR5	305	110	0.36	0.40	3730	0.134	1.02	7.283	1.51	0.394	1.11	0.74	2151	18	2147	13	2143	20	99.6
ZR6	257	46	0.18	1.06	1407	0.132	0.97	7.138	1.99	0.391	1.72	0.87	2129	17	2129	18	2128	31	99.9
91500 (1)	65	16	0.24	0.03	50692	0.074	2.66	1.766	3.90	0.173	2.85	0.73	1042	53	1033	25	1029	27	98.7
91500 (2)	69	17	0.25	0.04	48361	0.074	2.22	1.794	3.20	0.176	2.30	0.72	1038	44	1043	21	1046	22	100.8
Sample AUFC-1-5 (AS Gr) (13°22'25.1" S 47°04'17.4" W)																			
ZR1c	600	139	0.23	0.45	3295	0.138	1.00	7.726	7.34	0.405	7.24	0.99	2206	17	2200	64	2193	134	99.4
ZR1r	1400	69	0.05	0.16	9543	0.134	1.09	7.281	1.73	0.395	1.35	0.78	2148	19	2147	15	2145	25	99.9
ZR2	727	184	0.25	0.36	4111	0.134	0.62	7.336	2.46	0.398	2.37	0.97	2148	11	2153	22	2158	44	100.5
ZR3	270	47	0.18	0.01	154533	0.138	0.79	7.714	1.83	0.406	1.65	0.90	2198	14	2198	16	2199	31	100.1
ZR4	408	138	0.34	0.05	28824	0.139	0.74	7.622	1.74	0.397	1.57	0.91	2217	13	2187	15	2156	29	97.3
ZR5	1155	298	0.26	0.40	3478	0.169	2.29	11.366	3.21	0.487	2.24	0.70	2549	38	2554	29	2559	47	100.4
ZR6	1385	57	0.04	0.32	4665	0.150	0.59	8.162	1.62	0.395	1.51	0.93	2343	10	2249	15	2148	28	91.7
ZR7	709	415	0.59	0.16	8794	0.162	0.87	10.563	5.38	0.473	5.30	0.99	2477	15	2486	49	2496	109	100.8
ZR8	405	104	0.26	0.24	6245	0.152	0.56	8.374	1.68	0.400	1.58	0.94	2368	10	2272	15	2168	29	91.6
ZR9	80	28	0.36	0.07	21122	0.146	0.99	8.575	2.53	0.427	2.32	0.92	2297	17	2294	23	2290	45	99.7
ZR10	106	20	0.19	0.04	40319	0.133	0.85	7.010	1.45	0.382	1.18	0.81	2140	15	2113	13	2085	21	97.4
ZR11	1072	132	0.12	0.08	17838	0.139	0.67	7.848	1.53	0.410	1.38	0.90	2214	12	2214	14	2214	26	100.0
ZR12	726	154	0.21	0.15	9740	0.144	0.98	8.137	1.39	0.410	0.98	0.71	2275	17	2246	12	2215	18	97.4
ZR13	321	187	0.58	0.34	4243	0.149	1.45	8.937	4.13	0.436	3.85	0.94	2332	25	2332	37	2331	75	100.0
ZR14	2006	229	0.11	0.10	14696	0.138	1.83	7.725	7.71	0.407	7.48	0.97	2197	32	2200	67	2202	138	100.2
ZR15	173	48	0.28	0.21	7088	0.140	1.39	7.992	3.48	0.414	3.18	0.92	2228	24	2230	31	2233	60	100.2
ZR16	265	31	0.12	0.45	3261	0.137	0.99	7.641	2.13	0.405	1.88	0.88	2187	17	2190	19	2192	35	100.2
ZR17c	466	145	0.31	0.36	4117	0.144	0.84	8.264	4.17	0.416	4.09	0.98	2276	14	2260	38	2243	77	98.6
ZR17r	276	78	0.28	0.01	126946	0.139	0.93	7.815	2.17	0.407	1.96	0.90	2216	16	2210	20	2203	37	99.4
ZR18c	1204	158	0.13	0.10	14476	0.163	0.74	10.657	1.65	0.474	1.47	0.89	2487	12	2494	15	2502	31	100.6
ZR18r	866	19	0.02	0.60	2478	0.147	1.32	8.037	1.80	0.397	1.23	0.68	2308	23	2235	16	2157	23	93.5
ZR19c	371	95	0.26	0.27	5292	0.155	1.04	9.359	1.70	0.437	1.34	0.79	2406	18	2374	16	2336	26	97.1
ZR20	237	145	0.61	0.39	3737	0.143	0.74	8.084	3.77	0.411	3.70	0.98	2259	13	2240	34	2220	69	98.3
91500 (3)	56	13	0.23	0.03	56114	0.075	2.19	1.877	3.45	0.181	2.66	0.77	1080	43	1073	23	1070	26	99.1
91500 (4)	58	14	0.24	0.03	52058	0.074	3.20	1.805	4.34	0.176	2.93	0.67	1049	63	1047	28	1046	28	99.8
Sample AUFC-8-1 (AS T) (13°04'15.3" S 47°16'37.7" W)																			
ZR1	315	172	0.55	0.01	208997	0.135	1.09	7.336	2.71	0.396	2.48	0.92	2158	19	2153	24	2148	45	99.6

Table 4.2. (Continued).

Spot	U (ppm)	Th (ppm)	Th/U	f^{206} (%)	$^{206}Pb/^{204}Pb$	Ratio $^{207}Pb/^{206}Pb$	error (%)	Ratio $^{207}Pb/^{235}U$	error (%)	Ratio $^{206}Pb/^{238}U$	error (%)	error corr. (ρ)	Age $^{207}Pb/^{206}Pb$	error (Ma)	Age $^{207}Pb/^{235}U$	error (Ma)	Age $^{206}Pb/^{238}U$	error (Ma)	Concordance (%)
ZR2	272	98	0.36	0.00	317763	0.134	0.85	7.295	2.23	0.396	2.07	0.93	2147	15	2148	20	2150	38	100.1
ZR3	223	84	0.38	0.00	817594	0.134	1.06	7.293	2.23	0.395	1.96	0.88	2151	18	2148	20	2144	36	99.7
ZR4	346	180	0.52	0.00	397559	0.134	0.71	7.333	1.82	0.396	1.68	0.92	2155	12	2153	16	2150	31	99.8
ZR5	170	10	0.06	0.07	22270	0.133	0.82	7.215	3.44	0.394	3.33	0.97	2134	14	2138	30	2143	61	100.4
ZR6	341	218	0.64	0.00	488762	0.134	1.12	7.376	3.17	0.398	2.97	0.94	2157	19	2158	28	2159	54	100.1
ZR7	154	70	0.45	0.01	227376	0.132	1.46	7.220	3.90	0.395	3.62	0.93	2130	25	2139	34	2148	66	100.8
ZR8	140	71	0.51	0.01	273251	0.133	1.35	7.281	2.88	0.396	2.54	0.88	2142	23	2147	25	2151	46	100.4
ZR9	220	121	0.55	0.01	224887	0.134	1.39	7.434	3.06	0.401	2.73	0.89	2156	24	2165	27	2174	50	100.8
ZR10	319	233	0.73	0.00	341775	0.134	1.10	7.297	1.69	0.394	1.28	0.76	2156	19	2148	15	2141	23	99.3
ZR11	402	272	0.68	0.00	513205	0.135	1.42	7.460	3.22	0.400	2.89	0.90	2167	25	2168	28	2169	53	100.1
ZR12	240	131	0.54	0.06	25020	0.135	0.98	7.424	2.10	0.398	1.86	0.89	2167	17	2164	19	2161	34	99.7
ZR13	317	223	0.71	0.01	118849	0.136	0.75	7.420	2.20	0.396	2.07	0.94	2174	13	2163	20	2152	38	99.0
ZR14	318	160	0.50	0.00	535102	0.135	0.82	7.412	1.60	0.397	1.37	0.86	2169	14	2162	14	2155	25	99.3
ZR15	603	454	0.75	0.04	33807	0.135	0.80	7.496	2.05	0.403	1.88	0.92	2163	14	2173	18	2182	35	100.9
ZR16	222	133	0.60	0.00	327505	0.135	0.74	7.367	1.91	0.396	1.76	0.92	2165	13	2157	17	2149	32	99.3
ZR17	371	185	0.50	0.01	222636	0.135	0.70	7.406	1.58	0.398	1.42	0.90	2162	12	2162	14	2161	26	99.9
ZR18	195	95	0.49	0.02	95053	0.134	0.89	7.290	1.43	0.394	1.12	0.79	2154	15	2148	13	2141	20	99.4
ZR19	120	56	0.47	0.01	186923	0.134	1.27	7.355	2.64	0.399	2.32	0.88	2145	22	2156	23	2166	42	101.0
ZR20	112	35	0.31	0.01	186348	0.133	1.13	7.235	2.20	0.394	1.88	0.86	2141	20	2141	19	2141	34	100.0
ZR21	309	173	0.56	0.00	483510	0.134	0.95	7.390	2.04	0.399	1.80	0.89	2156	16	2160	18	2164	33	100.4
ZR22	109	52	0.48	0.00	462233	0.134	1.06	7.333	2.19	0.397	1.92	0.87	2152	18	2153	19	2154	35	100.1
ZR23	333	187	0.56	0.01	255144	0.134	0.98	7.323	1.86	0.395	1.58	0.85	2157	17	2152	17	2146	29	99.5
ZR24	81	34	0.42	0.01	192381	0.134	0.84	7.346	2.51	0.397	2.36	0.94	2154	15	2154	22	2155	43	100.0
ZR25	262	102	0.39	0.00	327345	0.134	1.28	7.336	2.35	0.397	1.97	0.84	2150	22	2153	21	2157	36	100.3
ZR26c	1073	4	0.00	0.00	1101322	0.137	1.10	7.620	1.83	0.403	1.46	0.80	2189	19	2187	16	2185	27	99.8
ZR26r	133	39	0.30	0.00	348509	0.134	0.72	7.276	1.22	0.394	0.99	0.81	2151	12	2146	11	2140	18	99.5
ZR27	456	290	0.64	0.00	585192	0.136	1.12	7.480	1.64	0.399	1.19	0.73	2175	19	2171	15	2166	22	99.5
ZR28	74	23	0.32	0.14	10625	0.133	1.73	7.179	2.25	0.392	1.44	0.64	2137	30	2134	20	2131	26	99.7
91500 (5)	51	12	0.23	0.02	69699	0.075	3.40	1.808	6.10	0.175	5.06	0.83	1069	67	1048	39	1039	48	97.1
91500 (6)	60	14	0.23	0.03	48646	0.075	1.85	1.803	3.08	0.175	2.47	0.80	1056	37	1047	20	1042	24	98.7
Sample AUFC-43-1 (Arr P) (12°52'30.3" S 46°53'12.4" W)																			
ZR1	105	39	0.38	0.02	74362	0.136	2.14	7.355	3.67	0.393	2.98	0.81	2175	37	2155	32	2135	54	98.2
ZR2	206	94	0.46	0.01	131837	0.134	1.46	7.281	3.10	0.395	2.73	0.88	2146	25	2147	27	2147	50	100.0
ZR3c	293	72	0.24	0.03	49421	0.134	1.73	7.364	3.86	0.397	3.45	0.89	2156	30	2157	34	2157	63	100.1
ZR3r	267	87	0.33	0.03	45632	0.134	1.88	7.275	4.51	0.394	4.10	0.91	2152	32	2146	40	2139	74	99.4
ZR4	247	133	0.54	0.01	203504	0.134	1.22	7.368	2.82	0.399	2.54	0.90	2151	21	2157	25	2164	47	100.6
ZR5c	180	91	0.51	0.01	141782	0.132	1.26	7.175	1.96	0.393	1.51	0.77	2128	22	2133	17	2139	27	100.5
ZR5r	377	227	0.60	0.01	156373	0.135	1.10	7.582	2.16	0.408	1.86	0.86	2163	19	2183	19	2203	35	101.9
ZR6	198	103	0.52	0.01	117040	0.135	1.25	7.429	2.47	0.400	2.12	0.86	2159	22	2164	22	2170	39	100.5

Table 4.2. (Continued).

Spot	U (ppm)	Th (ppm)	Th/U	f^{206} (%)	$^{206}Pb/^{204}Pb$	Ratio $^{207}Pb/^{206}Pb$	error (%)	Ratio $^{207}Pb/^{235}U$	error (%)	Ratio $^{206}Pb/^{238}U$	error (%)	error corr. (ρ)	Age $^{207}Pb/^{206}Pb$	error (Ma)	Age $^{207}Pb/^{235}U$	error (Ma)	Age $^{206}Pb/^{238}U$	error (Ma)	Concordance (%)
ZR7	93	30	0.32	0.02	64959	0.134	2.07	7.264	3.34	0.394	2.63	0.79	2147	36	2144	29	2141	48	99.7
ZR8	146	55	0.37	0.02	68682	0.136	2.10	7.441	3.16	0.397	2.36	0.75	2177	36	2166	28	2155	43	99.0
ZR9	237	164	0.69	0.02	94532	0.134	1.62	7.285	2.61	0.396	2.04	0.78	2145	28	2147	23	2149	37	100.2
ZR10	251	96	0.38	0.07	21352	0.133	1.84	7.307	2.85	0.397	2.18	0.76	2143	32	2150	25	2156	40	100.6
ZR11	216	123	0.57	0.01	102316	0.132	1.80	7.027	2.97	0.386	2.36	0.80	2125	31	2115	26	2104	42	99.0
ZR12	233	137	0.59	0.02	76453	0.135	1.54	7.385	3.21	0.396	2.81	0.88	2167	27	2159	28	2151	51	99.3
ZR13	183	103	0.57	0.01	139096	0.133	1.55	7.309	2.68	0.398	2.18	0.82	2140	27	2150	24	2160	40	100.9
ZR14	225	94	0.42	0.02	98881	0.134	1.32	7.126	2.23	0.387	1.80	0.81	2145	23	2127	20	2109	32	98.3
ZR15c	155	72	0.46	0.01	105618	0.134	1.45	7.277	2.23	0.395	1.70	0.76	2145	25	2146	20	2147	31	100.1
ZR15r	209	96	0.46	0.01	182311	0.134	1.32	7.339	2.78	0.397	2.45	0.88	2154	23	2154	25	2153	45	100.0
91500 (7)	68	18	0.26	0.05	34002	0.074	4.27	1.783	5.84	0.174	3.99	0.68	1045	84	1039	37	1036	38	99.2
91500 (8)	68	18	0.26	0.06	28990	0.075	4.80	1.823	6.34	0.177	4.14	0.65	1061	94	1054	41	1050	40	99.0

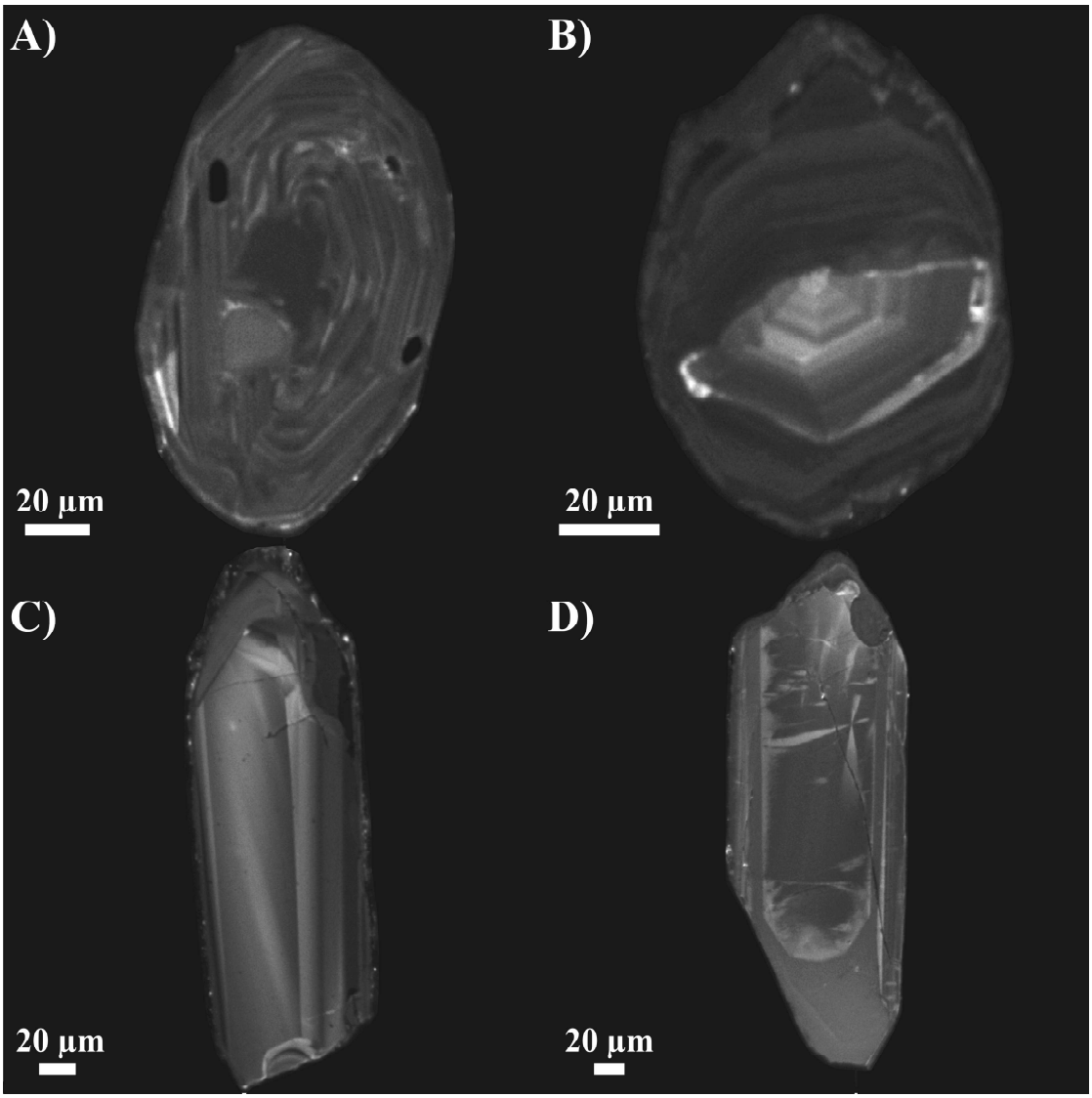

Fig. 4.9. Examples of internal textures of zircon crystals as revealed by CL imaging. **A**: Crystal from sample AUFC-40-1 displaying oscillatory to somewhat convoluted zoning. **B**: Crystal from sample AUFC-1-5 displaying inherited core. **C** and **D**: Crystals from samples AUFC-8-1 and AUFC-43-1, respectively, displaying broad, patchy zoning.

Concordant grains display a $^{207}Pb/^{206}Pb$ age close to 2.13 Ga for sample AUFC-40-1, which is interpreted as the magmatic crystallization age (Fig. 4.10a). One xenocrystic core was identified within this sample, yielding a nearly concordant age of ~2290 Ma. In sample AUFC-1-5, the fraction of inherited zircon is remarkably large yielding a spectrum of concordant to nearly concordant $^{207}Pb/^{206}Pb$ ages varying from 2140 to 2549 Ma (Fig. 4.10b).

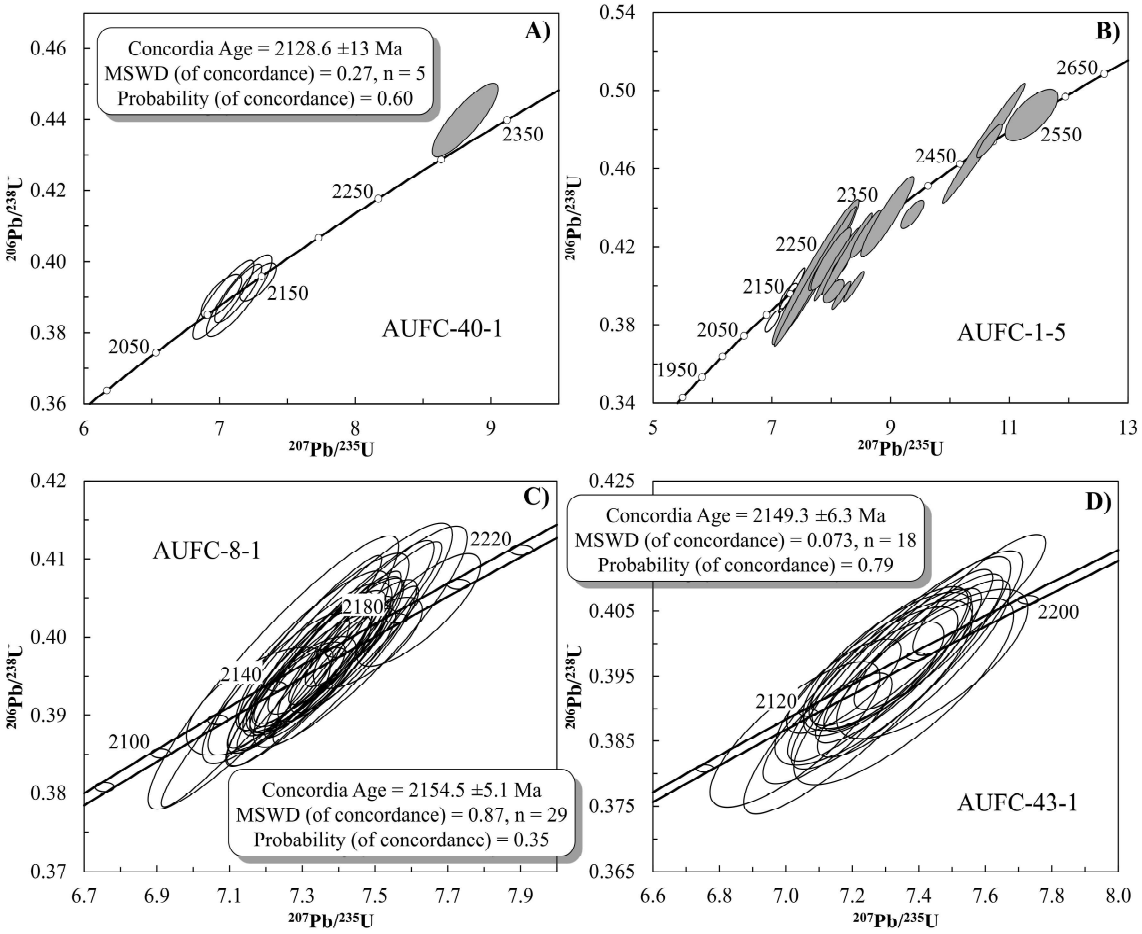

Fig. 4.10. Wetherill concordia plots of the analyzed samples. Samples AUFC-40-1 (**A**), AUFC-1-5 (**B**) and AUFC-8-1 (**C**) correspond to facies Au4, Au5 and Au3, respectively. Sample AUFC-43-1 (**D**) belongs to the Arraias unit. Dark-gray ellipses correspond to zircon crystals interpreted as either xenocrysts or inherited cores.

4.4.2.2.Aurumina Suite tonalite

The zircon grains from sample AUFC-8-1 display morphologies that are distinct from those of the Aurumina Suite granites. The grains are relatively large (150-500 μm), euhedral to subhedral, reddish, translucent and conspicuously elongated, with length/width ratios varying from 4 to 10. The CL images reveal virtually no metamictization, thus allowing preservation of inner structures characterized by patchy or broad zoning (Fig. 4.9c), which is distinct from the concentric and finer pattern found in more acidic rocks (Corfu *et al*., 2003). The mineral inclusions in the zircon grains of this unit are represented by quartz, biotite, muscovite, hornblende, epidote, apatite and feldspar.

Pb loss and common Pb in the zircon grains of sample AUFC-8-1 were very low (Table 4.2), enabling a concordant age of ~2.15 Ga to be obtained (Fig. 4.10c).

4.4.2.3.Arraias tonalite

The zircon grains of this unit (sample AUFC-43-1) are remarkably similar to those of the Aurumina Suite tonalite, with the only macroscopic difference being the presence of some whitish spots that suggest a moderate degree of metamictization. The internal structures are also similar to those of zircon from sample AUFC-8-1 and are characterized by patchy or broad zoning (Fig. 4.9d). Mineral inclusions are represented by quartz, biotite, sphene and hornblende.

A number of zircon crystals of the Arraias tonalite yielded a concordant age of 2.15 Ga, with negligible Pb loss and common Pb (Fig. 4.10d).

4.4.3. Sm-Nd isotope geochemistry

The results of Nd isotope analyses are shown in Table 4.3. An age range between 2.11 and 2.16 Ga was chosen for the calculations, seeking to account for the uncertainty in the U-Pb age estimates and the ages of facies Au1 and Au6, which represent the onset and the end of the magmatic event, respectively (not measured in this work).

As shown in Fig. 4.11, the most striking feature is that, regardless of rock type, the values of ε_{NdT} fall within a rather narrow range between -4.2 and +0.4. Among them, sample AUFC-43-1 (Arraias pluton) tends to have one of the highest ε_{NdT} values (between -0.5 and 0.0), while sample AUFC-1-1 (leucogranite) displays the lowest values (between -3.9 and -4.2). The ε_{NdT} values of the Aurumina Suite granites and tonalites-granodiorites do not show any preferential distribution within the interval and appear to be mixed.

Similarly, T_{DM} model ages also fall within a relatively narrow interval for all rock types, ranging from 2.33 to 2.92 Ga, although model ages between 2.40 and 2.58 Ga seem to be more common. An exception is, again, sample AUFC-1-1, which displays the oldest T_{DM} value of 3.14 Ga (Fig. 4.11).

Table 4.3. Sm-Nd isotope data. Errors in the last two digits of $^{143}Nd/^{144}Nd$ ratios are 2σ. Present-day $^{143}Nd/^{144}Nd_{CHUR}$ and $^{147}Sm/^{144}Nd_{CHUR}$ values used in calculations were 0.512638 and 0.1966, respectively (Jacobsen and Wasserburg, 1980; 1984). T_{DM} ages according to the depleted mantle model of DePaolo (1981).
AS Gr: Aurumina Suite Granite; **AS T/G**: Aurumina Suite Tonalite-Granodiorite; **Arr P**: Arraias Plutons.

* Sample of muscovite-albite pegmatite representing the most evolved phase of granites, and therefore included in the latter group despite being chemically equivalent to tonalite.

Sample	Rock Type	Location		Sm (ppm)	Nd (ppm)	$^{143}Nd/^{144}Nd$	$^{147}Sm/^{144}Nd$	$\varepsilon_{Nd}(T)_{min}$	$\varepsilon_{Nd}(T)_{max}$	T_{DM} (Ga)	T (Ga)
		Lat. (S)	Long. (W)								
AUFC-1-1	AS Gr	13°22'25.1"	47°04'17.4"	0.89	3.50	0.511838 (±16)	0.1543	-4.2	-3.9	3.14	2.11 - 2.16
AUFC-1-2	AS Gr	13°22'25.1"	47°04'17.4"	1.74	7.47	0.511839 (±17)	0.1409	-0.5	+0.1	2.52	2.11 - 2.16
AUFC-1-5	AS Gr	13°22'25.1"	47°04'17.4"	3.18	14.09	0.511744 (±16)	0.1365	-1.2	-0.8	2.57	2.11 - 2.16
AUFC-2-1	AS Gr	13°02'17.2"	46°59'53.3"	21.92	145.03	0.511113 (±23)	0.0914	-1.2	-0.6	2.40	2.11 - 2.16
AUFC-11-2	AS Gr	13°22'58.6"	46°55'41.9"	10.04	45.78	0.511634 (±33)	0.1326	-2.2	-1.8	2.65	2.11 - 2.16
AUFC-13-3	AS Gr	13°14'22.1"	46°50'58.0"	2.87	11.48	0.511895 (±23)	0.1511	-2.2	-1.9	2.82	2.11 - 2.16
AUFC-17-1	AS Gr*	13°13'10.3"	46°49'57.0"	0.13	0.63	0.511490 (±10)	0.1207	-1.8	-1.3	2.55	2.11 - 2.16
AUFC-18-1	AS Gr	13°19'22.5"	46°59'35.5"	3.44	15.10	0.511806 (±19)	0.1378	-0.3	+0.1	2.49	2.11 - 2.16
AUFC-22-1	AS Gr	13°41'54.0"	47°18'15.2"	23.11	167.57	0.510918 (±18)	0.0834	-2.9	-2.1	2.48	2.11 - 2.16
AUFC-24-1	AS Gr	11°57'59.1"	47°35'16.9"	14.08	86.98	0.511174 (±3)	0.0978	-1.8	-1.1	2.45	2.11 - 2.16
AUFC-25-1	AS Gr	11°57'53.3"	47°35'3.8"	5.22	31.01	0.511249 (±7)	0.1018	-1.4	-0.8	2.44	2.11 - 2.16
AUFC-32-1	AS Gr	13°59'23.6"	47°55'43.8"	26.46	178.98	0.511131 (±1)	0.0894	-0.3	+0.4	2.34	2.11 - 2.16
AUFC-34-1	AS Gr	14°04'0.4"	48°04'24.4"	20.78	129.63	0.511196 (±2)	0.0969	-1.1	-0.5	2.41	2.11 - 2.16
AUFC-40-1	AS Gr	13°29'48.3"	47°00'30.3"	30.24	256.69	0.510858 (±2)	0.0712	-0.7	+0.1	2.33	2.11 - 2.16
MALEG-1	AS Gr	13°14'22.3"	46°50'53.8"	2.20	8.74	0.511910 (±25)	0.1524	-2.2	-1.9	2.84	2.11 - 2.16
MALEG-4	AS Gr	13°10'26.0"	46°54'58.6"	4.29	21.13	0.511452 (±20)	0.1227	-3.1	-2.6	2.67	2.11 - 2.16
TEREZI-1	AS Gr	13°45'17.7"	47°13'58.1"	9.82	62.13	0.511091 (±16)	0.0955	-2.8	-2.1	2.51	2.11 - 2.16
TEREZI-2	AS Gr	13°46'19.1"	47°16'43.7"	11.65	67.71	0.511303 (±14)	0.1040	-0.9	-0.3	2.41	2.11 - 2.16
CAV-2	AS Gr	13°48'7.6"	47°35'49.8"	1.95	8.83	0.511694 (±11)	0.1413	-3.4	-3.1	2.86	2.11 - 2.16
CAV-4	AS Gr	13°47'32.7"	47°36'4.0"	12.24	70.86	0.511189 (±7)	0.1044	-3.3	-2.7	2.59	2.11 - 2.16
CAV-8B	AS Gr	13°50'43.1"	47°30'50.8"	3.11	19.88	0.511131 (±13)	0.0944	-1.7	-1.0	2.44	2.11 - 2.16
CAV-9	AS Gr	13°50'48.4"	47°30'28.9"	15.15	95.23	0.511130 (±4)	0.0962	-2.2	-1.6	2.48	2.11 - 2.16
AUFC-4-1	AS T/G	13°05'53.1"	47°10'2.3"	2.36	13.82	0.511282 (±20)	0.1033	-1.2	-0.6	2.43	2.11 - 2.16
AUFC-41-1	AS T/G	13°14'55.2"	47°08'35.7"	8.22	44.17	0.511393 (±3)	0.1125	-1.5	-1.0	2.48	2.11 - 2.16
MALEG-2	AS T/G	13°12'8.2"	46°48'24.5"	4.34	23.12	0.511385 (±18)	0.1135	-1.9	-1.4	2.52	2.11 - 2.16
MALEG-5	AS T/G	13°15'43.2"	46°55'44.5"	2.94	11.81	0.511852 (±18)	0.1508	-2.9	-2.6	2.92	2.11 - 2.16
MALEG-6A	AS T/G	13°18'46.1"	46°56'20.6"	1.08	5.14	0.511620 (±19)	0.1269	-1.0	-0.5	2.50	2.11 - 2.16
MENDES-2	AS T/G	13°20'0.2"	47°03'13.4"	3.71	14.94	0.511847 (±12)	0.1499	-2.8	-2.5	2.88	2.11 - 2.16
CALUNGA-1	AS T/G	13°29'15.0"	47°12'1.6"	1.57	7.48	0.511571 (±14)	0.1268	-1.9	-1.5	2.58	2.11 - 2.16
CAV-6B	AS T/G	13°44'2.1"	47°38'20.7"	17.43	7.54	0.511715 (±21)	0.1397	-2.6	-2.2	2.75	2.11 - 2.16
AUFC-43-1	Arr P	12°52'30.3"	46°53'12.4"	3.49	17.22	0.511585 (±11)	0.1226	-0.5	0.0	2.44	2.11 - 2.16

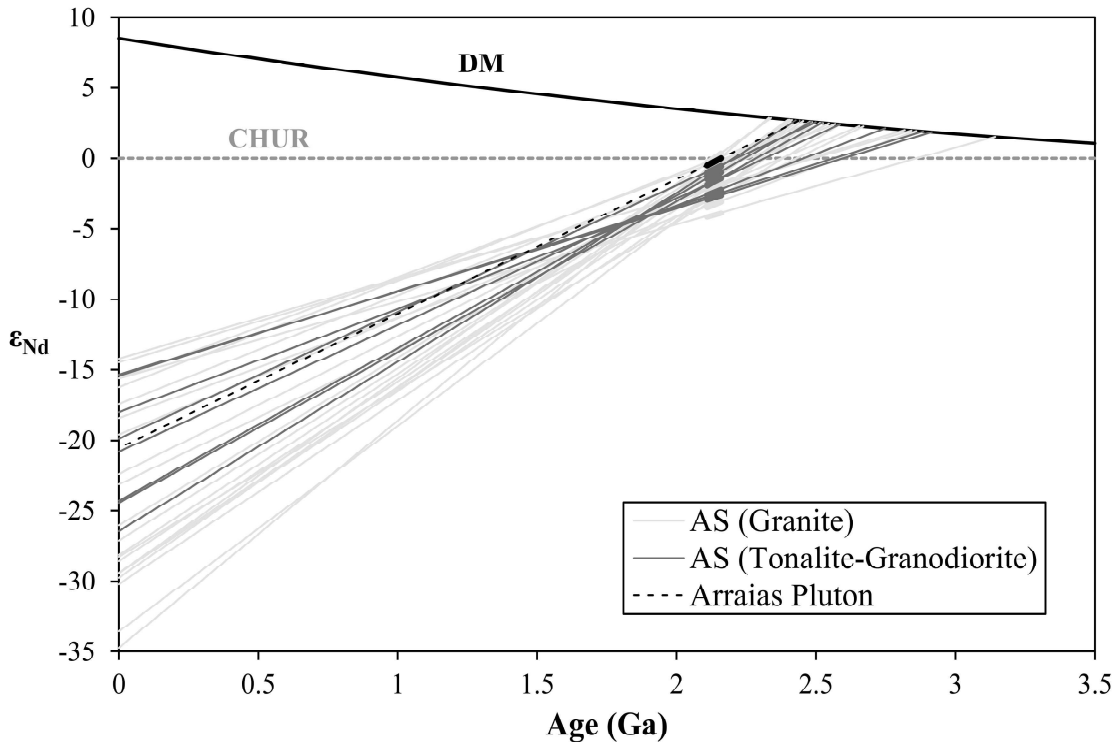

Fig. 4.11. ε_{Nd} vs. age plot of the analyzed samples. A magmatic crystallization age interval between 2.11 and 2.16 Ga is depicted for all samples. Depleted mantle (DM) curve according to model by DePaolo (1981). AS: Aurumina Suite.

4.5. DISCUSSION

4.5.1. Age of magmatism

Previous works on the geochronology of the Aurumina Suite reported zircon U-Pb crystallization ages between 2.12 and 2.18 Ga (Botelho *et al*., 2006a; Fuck *et al*., 2014; Corrêa *et al*., 2015; Sousa *et al*., 2016). Cassiterite U-Pb ages between 2.02 and 2.28 Ga along with muscovite K-Ar ages ranging from 2.01 to 2.13 Ga were also obtained by Sparrenberger and Tassinari (1999). In this work, CL imaging was carried out before LA-ICP-MS analyses, with the goal of detecting zones within the crystals that possibly represent discrete geological events. As shown in Appendix I, one inherited core in a zircon crystal from the Au4 granite was observed, while several inherited cores were found in the case of the Au5 granite. Fig. 4.10a shows a concordant age of 2.13 Ga for sample AUFC-40-1 while an age range between 2.14 and 2.50 Ga is observed in the case of Au5. Such older ages are interpreted as reflecting inheritance from older basement, which is in agreement with results of zircon U-Pb geochronology from samples of the Ticunzal Formation, with provenance age peaks between 2.19 and 2.4 Ga, along with subordinated populations at >2.4 Ga (Cuadros *et al*., in preparation). It follows that the

lower age limit of 2.18 Ga reported by Fuck *et al*. (2014) for the Aurumina Suite might actually represent a signal from inherited material. Therefore, the lower limit proposed in this work is 2.15-2.16 Ga. The abundance of inherited zircon in the Au5 sample is understandable when it is taken into account that this granite is intimately associated with the Ticunzal Formation in outcrop, as evidenced by enclaves of the latter within the granitic mass, which displays a migmatitic aspect. This probably indicates that extensive assimilation of the host rocks has taken place. Consequently, in view of the occurrence of a young age population close to ~2.15 Ga obtained from sample AUFC-1-5, which is interpreted to represent its magmatic crystallization age, it is suggested here that the Au5 granite does not represent a younger phase in the Aurumina Suite magmatism and that, instead, it is probably related to earlier pulses of Au1, as supported also by the geochemical criteria (see the source rock discussion below).

In the case of the Arraias sample, a concordant age of 2.15 Ga was obtained and is interpreted as its magmatic crystallization age (Fig. 4.10d), with the field relations showing an Au1 muscovite granite as its host rock.

4.5.2. Source rocks

Since early work on granites from the Lachlan Fold Belt, it has been clear that, in general, peraluminous granites owe a great deal of their nature to derivation from the melting of metasedimentary sources (*e.g.*, White and Chappell, 1977; Chappell and White, 1992; 2001, Chappell *et al*., 2000). This was later supported by experimental work (*e.g.*, Clemens and Wall, 1981; Patiño-Douce and Johnston, 1991; Holtz *et al*., 1992; Patiño-Douce and Beard, 1996; Patiño-Douce, 1999). Thus, a common tendency in petrological literature to assign an S-type character to peraluminous igneous rocks was established. One of the most striking features of the Aurumina Suite is the great volume of peraluminous tonalitic-granodioritic rocks that crop out over more than 7,350 km^2 and are intimately associated with peraluminous granites. Classifying these tonalites/granodiorites as S-type rocks is, however, contentious, as rocks of such composition are commonly thought to result from the melting of mafic sources rather than graywacke or pelitic ones (*e.g.*, Barker and Arth, 1976; Rapp *et al*., 1991; Rushmer, 1991; Rapp and Watson, 1995; Winther, 1996; Wyllie *et al*., 1997; Rapp *et al*., 2003).

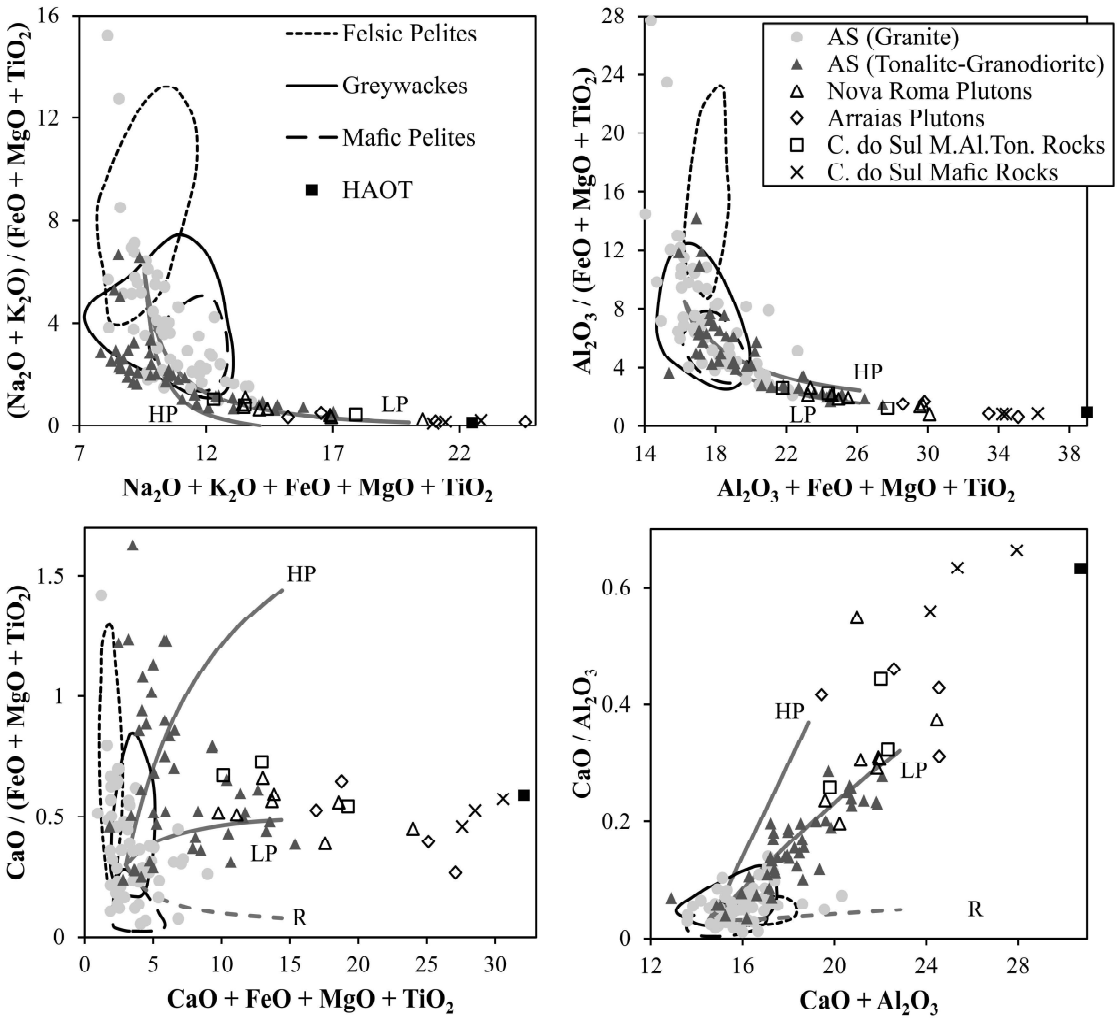

Fig. 4.12. Visualization of the analyzed samples in the major element plots by Patiño-Douce (1999). Fields correspond to compositions of melts generated from different metasedimentary sources, while the HP and LP curves correspond to high-pressure (12-15 kbar) and low-pressure (≤ 5 kbar) reaction paths, respectively, between those sources and a basaltic melt. The "R" curves correspond to the paths that would be followed by melts undergoing restite separation without interaction with a mafic component. Experimental data from Patiño-Douce (1999). The basaltic member is represented by the high-alumina olivine tholeiite (HAOT) used in the experiments of Patiño-Douce (1995). M.Al.Ton. = Metaluminous Tonalitic Rocks. AS = Aurumina Suite.

When major element data from the Aurumina Suite are visualized in the sums vs. ratios plots presented by Patiño-Douce (1999), a distinctive pattern for most of Aurumina Suite tonalites/granodiorites and the group of mafic/intermediate rocks (Nova Roma, Arraias and Colinas do Sul) emerges (Fig. 4.12): these rocks tend to follow the path defined experimentally by Patiño-Douce (1995) for reaction between metapelite and basaltic melt at low pressures (< 5 kbar), with the Colinas do Sul samples plotting closest to the high-Al olivine tholeiite (HAOT) end-member. In contrast, the granites tend to plot within the fields of melts derived from graywacke and pelite sources. Thus, these features provide a first hint of the possible hybrid character of the source that produced the

Aurumina Suite, adding to the compositional contrasts already observed in Figs. 4.6c, 4.7a and 4.7b, as well as the remarkable resemblance between the tonalites of both the Aurumina Suite and Arraias in terms of chemical composition, age, zircon mineral inclusions (*e.g.*, hornblende is observed in both peraluminous and metaluminous rock types) and morphology of the latter (see section 4.2). The low-pressure conditions for such a hybridization process would be consistent with the relatively low $(La/Yb)_N$ ratios observed in the Aurumina Suite samples, suggesting that significant amounts of garnet would not have been formed upon reaction at the source (Fig. 4.7b, Table 4.1).

One important aspect of the studied rocks is the lack of features and textures indicative of magma mixing. The granites and tonalites/granodiorites of the Aurumina Suite appear remarkably homogeneous in all inspected outcrops, without any mafic enclaves or schlieren structures, although biotite-rich paragneiss enclaves are common. The Nd isotopic compositions shown in Fig. 4.11 indicate a rather narrow range of initial ε_{NdT} values between +0.4 and -4.2. While the initial ε_{NdT} values of S-type granites typically vary between -5 and -10, or even lower (*e.g.*, McCulloch and Chappell, 1982; Deniel *et al*., 1987; Villaseca *et al*., 2008; Köksal and Göncüoğlu, 2008; Paul *et al*., 2014), higher values in the Aurumina Suite are consistent with homogenization of a crustal source with more radiogenic mantle-derived material with initial $\varepsilon_{NdT} \geq 0$. Therefore, it is suggested here that the magmas of the Aurumina Suite were produced by hybridization resulting from the reaction of metasedimentary rocks with mantle-derived melts at depth. This is in agreement with the results of experiments carried out by Patiño-Douce (1995), in which melting of mixtures of basaltic glass and gneissic/pelitic material yielded hybrid compositions similar to the ones presented here. This hybridization process could also explain the common presence of graphite in both granitic and tonalitic rocks, thus accounting for the reduced character of the Aurumina Suite, as inferred from the presence of ilmenite instead of magnetite in the studied samples.

Although the Ticunzal Formation could at first be regarded as a likely crustal source, the ε_{NdT} values of this formation are in the same range as those obtained here for the Aurumina Suite (Cuadros *et al*., in preparation), thus preventing the establishment of such a parentage relationship because more negative ε_{NdT} values would be required to obtain the signature of the Aurumina Suite by reaction with more radiogenic, mantle-derived material. Likewise, if juvenile mantle-derived magmas actually participated in the origin of the Aurumina Suite, then the T_{DM} ages obtained for the suite must reflect an

average of the isotopic compositions of the end-members involved in the hybridization, which would indicate that the metasedimentary component must have had isotopic compositions compatible with older T_{DM} ages and more negative ε_{NdT} values, therefore ruling out the Ticunzal Formation as a possible source. Preliminary results of recent mapping campaigns by the Brazilian Geological Survey in the region of Dianópolis indicate the presence of Aurumina Suite plutons intruding the 2.2-2.4 Ga tonalitic-supracrustal basement and the absence of the Ticunzal Formation, which would support the latter hypothesis (CPRM, 2014). In this regard, one possibility is that the metasedimentary component of the source is related to the same material from which the peraluminous, low-K calc-alkaline rocks of the Suite 2 in the Almas-Dianópolis domain are derived, and for which T_{DM} ages as old as 2.76 Ga are reported (Cruz, 2001). However, older T_{DM} ages of the Aurumina Suite (close to 2.9-3.1 Ga) could also indicate that older unknown sources might have been involved. Alternatively, it might be possible that the Ticunzal Formation was actually a source for the Aurumina Suite, but the rocks in the deep source region were different from those that are exposed at the surface today. This situation would be similar to that of some S-type granites in both the Lachlan Fold Belt and the eastern Hodgkinson Province in Australia, where it is hypothesized that metasedimentary source rocks that produced the magmas differ from the turbiditic rocks that host the granites (Clemens, 2003; Champion and Bultitude, 2013). Although it is clear that the exposed Ticunzal Formation rocks must have exerted some influence on both the chemical and isotopic compositions of the Aurumina Suite, as evidenced by the widespread occurrence of paragneiss, schist and graphitic enclaves (Fig. 4.5c), a simple assimilation mechanism would not be sufficient to produce both the homogeneous isotope composition and peraluminosity observed in the granites and tonalites of the Aurumina Suite. Assimilation is also recognized in the case of a Nova Roma intrusion, where field observations reveal a zone of transition from metaluminous, hornblende-dominated quartz dioritic-tonalitic rocks to peraluminous, hornblende-free tonalites intruding Au2 biotite-muscovite monzogranites. An interesting situation occurs in the case of one of the Arraias intrusions, where a high-MgO (~10 wt.%) tonalite displays magmatic cummingtonite as the main ferromagnesian phase. Although rare, magmatic cummingtonite occurs mostly in sub-volcanic rhyodacitic intrusions, where it is indicative of temperatures up to 800°C and high P_{H_2O}/P_{total} (d'Arco *et al.*, 1981; Geschwind and Rutherford, 1992; Evans and Ghiorso, 1995; Pallister *et al.*, 1996; Rutherford and Devine, 1996). However, in the case of plutonic rocks, the few known

occurrences of magmatic cummingtonite are characteristically related to compositions ranging from gabbro/diorite to granodiorite (*e.g.*, Deer, 1935; Nockolds, 1940; Stewart, 1946; De Capitani *et al.*, 1990). Although it is not clear why cummingtonite appears in the latter cases, it is interesting to note that a common feature linking the known examples is the hybrid characteristics of the mafic-intermediate rocks that host the mineral. In the Strzelin Massif, Pietranik (2003) reports magmatic cummingtonite in a tonalite displaying magma-mixing characteristics. In this case, Pietranik (2003) interpreted cummingtonite as having formed after Ca depletion of the magma due to crystallization of anhydrite.

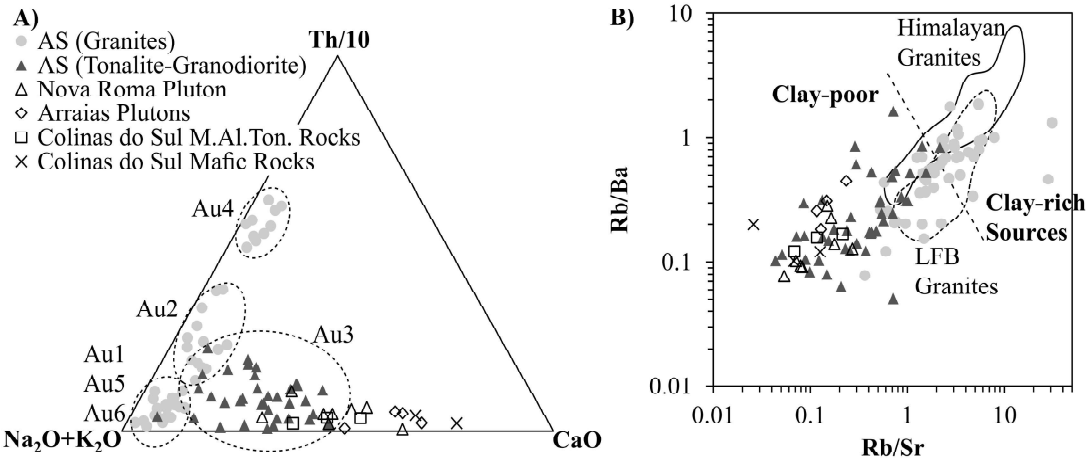

Fig. 4.13. Geochemical features of the analyzed samples. **A**: Alkalis-Th/10-CaO diagram displaying contrasts in the Th contents of the different rock types. **B**: Rb/Sr vs. Rb/Ba diagram for discrimination between clay-poor and clay-rich sources of granites. Reference boundary and compositional fields of Himalayan and Lachlan Fold Belt (LFB) granites as presented by Sylvester (1998). M.Al.Ton. = Metaluminous Tonalitic Rocks. AS = Aurumina Suite.

The sample compositions plotted in the alkalis-Th/10-CaO diagram shown in Fig. 4.13a define a pattern consisting in granites divided into three separate clusters with contrasting Th contents. As mentioned above, the granites of facies Au2 and Au4 are distinguished in the field by their characteristically high gamma-ray response (which is typically stronger in Au4 than in Au2) resulting from large amounts of Th contained in minerals such as monazite and thorite. Notably, some samples previously mapped as Au2 fall in the upper cluster of Fig. 4.13a (corresponding to the highest content of Th) as well as all samples of Au4. The intermediate Th-rich cluster is composed of a group of Au2 samples, while the Th-poor cluster is defined by samples belonging to facies Au1, Au5 and Au6. Samples of Au2 plotting in the upper cluster have fabric and mineralogical features compatible with those of Au4 granites (*i.e.*, large amounts of biotite and potassic feldspar). Thus, it is proposed here that the alkalis-Th/10-CaO diagram serves as a geochemical discriminant for the different Aurumina Suite granite types and that some

granites previously mapped as Au2 (including the granite exposed in the type area of Aurumina village) actually correspond to the Au4 facies, demonstrating the need to refine the geological mapping of the studied region. Moreover, it is suggested that the compositional differences of the three clusters in Fig. 4.13a reflect distinct granite sources, thus suggesting likely lithological diversity in the metasedimentary source. This criterion can be applied in a restricted fashion to the pegmatitic granites of Au6, which owe their low Th content and overall composition to extreme fractionation, as they represent the latest and most evolved facies of the Aurumina Suite. Indeed, as shown in Fig. 4.13b, a number of granite samples tend to fall in the field of peraluminous granites derived from clay-rich sources of Sylvester (1998), while some seem to reflect clay-poor sources. It is not clear whether the latter group owes its signature to actual derivation from clay-poor sources or to interaction between basaltic melts and pelitic rocks. However, as noted in Fig. 4.12, the sample compositions fit the hybridization curves between mafic magma and pelitic rocks. The Au3 samples (tonalites and granodiorites) display relatively low Th contents, and their position in the alkalis-Th/10-CaO diagram suggests that they might have formed via interaction between mafic components and the sources defined by clusters related to Au2 and Au1-Au5 facies (Fig. 4.13a). In the latter case, it is likely that the Au5 phase is actually related to earlier pulses of Au1 rather than younger ones, as mentioned above, given its apparent magmatic age of ~2.15 Ga, as well as the chemical and mineralogical similarities shown in Fig. 4.13a.

4.5.3. Tectonic setting

The traditional paradigm that exists in the petrological literature about peraluminous granites being S-type and somehow related to Himalayan-type collisional magmatism, led in the past to assume such a setting for the magmatism that produced the Aurumina Suite. This assumption was in part sustained by the trace element compositions of Aurumina Suite granites that plotted in the collisional fields of tectonic discrimination diagrams (Botelho *et al*., 2006a; Sousa *et al*., 2016). However, a number of features argue against this model, the most important of which is the absence of the essential components that constitute a collisional setting, such as a large allochthonous continental mass and a crustal-scale suture separating that continental mass from the western margin of the São Francisco Craton, which would represent the second landmass involved in such a hypothetical collision. In addition, typical Himalayan S-type granites are commonly leucocratic, of limited extent and display isotopic compositions with a strongly crustal

signature (*e.g.*, Le Fort, 1981; Deniel *et al*., 1987; Le Fort *et al*., 1987; Guo and Wilson, 2012), properties that are not particularly evident in the peraluminous granites of the Aurumina Suite. One of the key differences between the Himalayan case and the geological setting dealt with in this work is the presence of mafic magmatic activity in the latter, as stated in the previous section. The intrusion of mafic magmas would have provided not only the components necessary to generate the great volume of tonalitic rocks and their associated geochemical and isotopic signatures but also the heat necessary to melt the crust and generate the equally great volume of granitic magmas. No basaltic rocks associated in space and time with the leucogranites are currently known in the Himalaya, and the driving mechanisms for partial melting of the metasedimentary sources of those granites are thought to be related either to crustal thickening, increased fluid activity, shear-zone activity heating, radioactive heating or lithospheric decompression (Harris and Massey, 1994; Whittington and Treloar, 2002; Nábělek and Liu, 2004; Searle *et al*., 2009; Guo and Wilson, 2012).

When the geochemical argument for a collisional setting of the Aurumina Suite is revised, some considerations must be made in relation to its meaning. In Fig. 4.14, two classic tectonic discrimination diagrams by Pearce *et al*. (1984) and Batchelor and Bowden (1985) are shown along with recently developed discrimination criteria by Verma *et al*. (2013). In all cases, there is ambiguity as to the actual tectonic setting of the Aurumina Suite, as data tend to be distributed between the collisional and magmatic arc fields. However, it must be noted that, despite this apparently dual behavior, the tonalitic rocks of the Aurumina Suite and the mafic to intermediate rocks of Nova Roma and Arraias are the ones that plot within the arc field, while the granites tend to plot within the collisional setting field. This means that the composition of those rocks is actually reflecting their sources rather than their tectonic setting. Clearly, the arc-related rocks used by the different authors to delineate the boundaries of the arc fields of the diagrams in Fig. 4.14 must have had a mantle-derived source, while the sources of the rocks belonging to the collisional fields must have been metasedimentary rocks. The fact that samples of the Aurumina Suite are distributed between those two fields is an indication of the relative contributions of the two distinct components that participated in the generation of the Aurumina Suite magmas via a source hybridization process, as discussed in the previous section. Therefore, invoking a collisional event predated by the establishment of a magmatic arc for the generation of the granites and tonalites of the

Aurumina Suite, as proposed by Sousa *et al*. (2016), is unnecessary as well as erroneous, especially when taking into account that these rocks were formed during the same magmatic event, as indicated by the geochronological and field evidence.

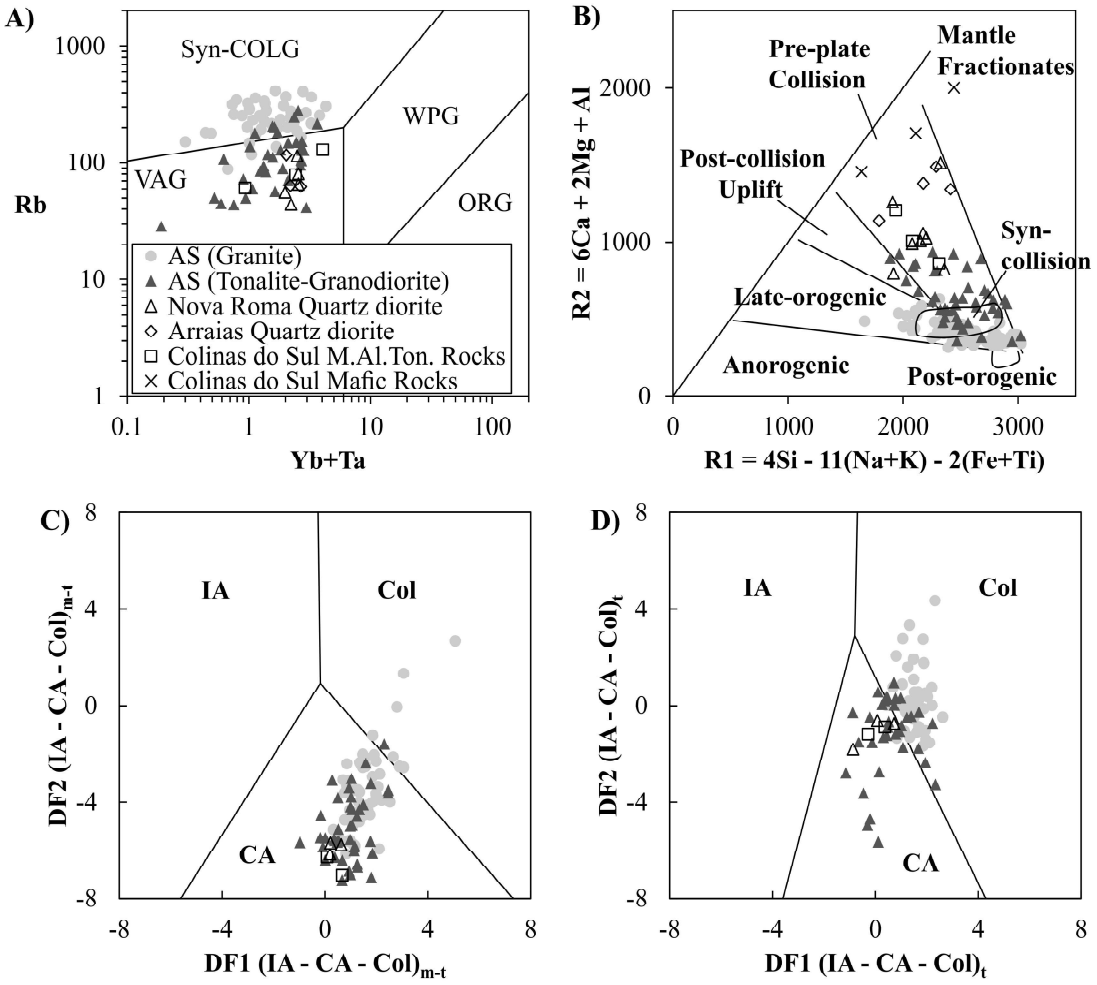

Fig. 4.14. Plots of the analyzed samples in tectonic discrimination diagrams. **A**: Rb vs. Yb+Ta diagram by Pearce *et al*. (1984). **B**: Adapted R1-R2 diagram by Batchelor and Bowden (1985). Diagrams using discriminant functions based on both major and trace element data (**C**) and trace element only (**D**), as devised by Verma *et al*. (2013). Composition of samples plotted in C and D were first verified and adjusted using the IgRoCs software developed by Verma and Rivera-Gómez (2013). Syn-COLG: syn-collisional granites; WPG: within-plate granites; VAG: volcanic-arc granites; ORG: ocean-ridge granites; IA: island arc; Col: collision; CA: continental arc; M.Al.Ton.= Metaluminous Tonalitic Rocks; AS = Aurumina Suite.

Having thus ruled out the establishment of a Rhyacian collisional orogen in the region studied in this work, some very interesting similarities between the setting of the Aurumina Suite and the Jurassic-Cretaceous cordilleran interior of North America are noted. Firstly, the latter region is known for the occurrence of an extensive belt of Jurassic-Paleogene voluminous two-mica peraluminous granitic rocks with crustal geochemical signatures, emplaced during a compressional regime (Miller and Bradfish, 1980; Miller and Barton, 1990). These rocks have been shown to occur in association

with metaluminous, intermediate plutonic rocks, sometimes even displaying evidence of interaction with coeval mafic magmas which occur either as enclaves or dykes within the peraluminous rocks (*e.g.*, Hyndman, 1983; Hyndman and Foster, 1988) and that might represent melts formed after upwelling of asthenospheric mantle (Elison, 1995; Leventhal *et al*., 1995; Wells and Hoisch, 2008). This peraluminous belt was located inland from a contemporary magmatic arc to the west (up to >400 km), at the margin of old thick crust represented by the North American Craton. In the case presented in this work, the peraluminous Aurumina Suite is located on the western margin of the São Francisco Craton, 50-200 km eastward from the axis defined by arc-related rocks in the regions of Monte do Carmo, Campinorte-Artulândia and Silvânia (Fig. 4.15). In Monte do Carmo, the volcanic Santa Rosa Suite contains a group of dacitic and rhyolitic rocks that occur in association with the Carmo Granite. These units yield zircon U-Pb ages of 2086 ± 10 Ma (Santa Rosa Suite) and 2048 ± 13 Ma (Carmo Granite) and display chemical and isotopic compositions compatible with generation in an arc setting (Saboia, 2009). The Campinorte Sequence and associated Pau de Mel plutonic suite include metasedimentary and metavolcanic rocks, tonalite, granodiorite and granite with ages between 2090 and 2180 Ma and are interpreted as having formed in a magmatic arc based on geological, geochemical and isotopic data (Oliveira *et al*., 2007; Giustina *et al*., 2009; Cordeiro *et al*., 2014). Close to Campinorte, in the Artulândia region, another portion of this magmatic arc is inferred based on the presence of metavolcanic rocks and associated calc-alkaline tonalite and granodiorite yielding zircon U-Pb ages between 2130 and 2156 Ma (Filgueiras, 2015). Similarly, an arc setting has been inferred for the metavolcanic rocks of the Silvânia Sequence and the Jurubatuba granite further south, which yielded zircon magmatic ages of 2115 Ma and 2089 Ma, respectively (Fischel *et al*., 2001). Therefore, it would be plausible that the Monte do Carmo, Campinorte and Silvânia rocks represent the Rhyacian magmatic arc to which the Aurumina Suite magmatism is related, thus corresponding to an analogue case in which the peraluminous granites of the North American hinterland are related to the coeval arc magmatism exemplified by the Sierra Nevada Batholith in the North American cordillera (Miller and Barton, 1990). The enriched nature of the Colinas do Sul mafic rocks is consistent with the generation of basaltic magmas from an asthenospheric source, as has been proposed for analogous rocks in the cordilleran interior of North America.

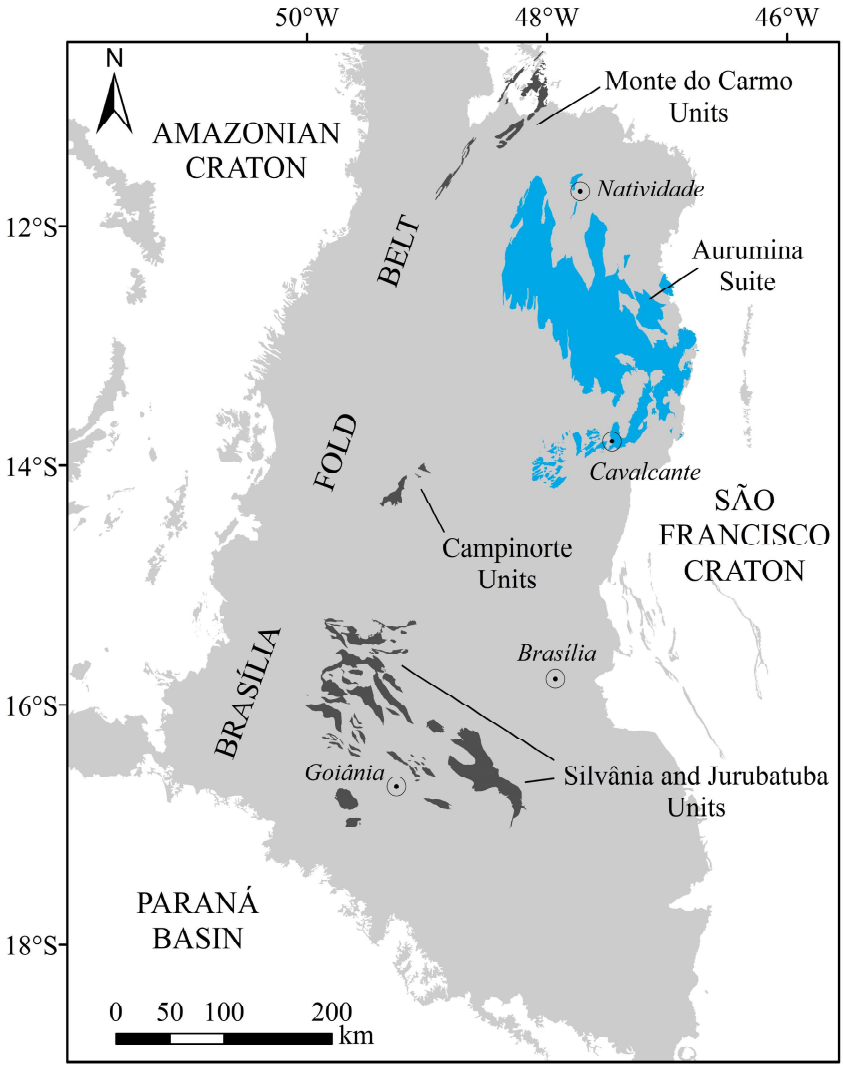

Fig. 4.15. Geological sketch of the Tocantins Province (light gray) showing the position of the Aurumina Suite (blue) in relation to coeval (Rhyacian) arc-related rocks (dark gray). Based on 1:1,000,000 scale geological charts by the Brazilian Geological Survey (CPRM; http://geobank.cprm.gov.br/).

However, some important differences exist between the two cases and they must be addressed here. Unlike the North American analogue, mingling of crustal and basaltic melts is not observed in the Aurumina Suite, as participation of a mantle-derived phase in its generation is thought to have occurred at the source and not at emplacement levels, which would also explain the abundance of tonalitic rocks reported in this work. In addition, it has been shown that, for some of the North American granites, partial melting of the source occurred at rather high pressures (*e.g.*, Hyndman, 1983; Kapp *et al.*, 2002), as opposed to the shallow depths inferred for magma hybridization of the Aurumina Suite. Isotopic data indicate that the crustal signature of some of the North American granites does not require derivation from metasedimentary precursors and is instead due to the isotopically evolved character of the old Precambrian sources in relation to the Mesozoic

age of magma extraction, although a progressively greater contribution of metasedimentary material might have occurred later in the magmatic history (Miller and Barton, 1990). In the case of the Aurumina Suite, a much shorter time gap between source formation and melting is inferred from the T_{DM} ages, which mainly vary between 2.4 and 2.6 Ga, and metasedimentary sources are deemed necessary to explain the hybrid isotopic composition of the Aurumina Suite as well as its reduced character. Lastly, the extent of the peraluminous belt in the North American interior is far greater than that of the Aurumina Suite, possibly reflecting differences in geodynamic regimes or simply a poorer preservation state of the Paleoproterozoic crust that might have been either eroded away or covered by younger supracrustal units.

4.6. CONCLUSIONS

The data presented in this work suggest the following conclusions:

- Peraluminous granites and tonalites/granodiorites of the Aurumina Suite were emplaced on the western border of the São Francisco Craton during the 2.11- 2.16 Ga interval.

- The geochemical and isotopic data suggest that the Aurumina Suite and associated metaluminous/intermediate units, such as the Nova Roma, Colinas do Sul and Arraias rocks, represent a continuum of hybrid magmas that resulted from reaction between metasedimentary rocks and basaltic melts at shallow depths in the crust (< 18 km).

- The metasedimentary component of the source that produced the Aurumina Suite could be related to the same source(s) that generated the 2.2-2.4 Ga rocks in the Almas-Dianópolis domain or to older, unknown material. Alternatively, the Ticunzal Formation might have played a role as a source of the Aurumina Suite, but the rocks deep in the source region must have had different characteristics from the ones found at the surface today, which host the Aurumina Suite.

- A number of similarities exist between the region studied in this work and the Jurassic-Paleogene peraluminous granitic belt of the cordilleran hinterland of North America, which suggests a similar arc-related setting for the magmatism of the Aurumina Suite.

4.7. ACKNOWLEDGEMENTS

This work was possible thanks to financial support from the Conselho Nacional de Desenvolvimento Científico e Tecnológico (CNPq) of Brazil under grant 156627/2012-4 to FAC, and INCTET grant to RAF. NFB, RAF and ELD acknowledge CNPq research fellowships. Assistance from technical staff of the geochronology and petrography laboratories of the University of Brasília is also gratefully acknowledged.

CAPÍTULO 5 - "THE TICUNZAL FORMATION IN CENTRAL BRAZIL: RECORD OF RHYACIAN SEDIMENTATION AND METAMORPHISM IN THE WESTERN BORDER OF THE SÃO FRANCISCO CRATON"

ABSTRACT

The Ticunzal Formation is exposed in the northern portion basement of the external zone of the Brasília Fold Belt and corresponds to a sequence of biotite-garnet paragneisses and mica-graphite schists with mineral assemblages indicating retrograde metamorphism under greenschist facies conditions. The formation displays local mylonitic structures and is intruded syn- to post-tectonically by 2.11-2.16 Ga peraluminous plutons of the Aurumina Suite. Detrital zircon U-Pb ages, Nd model ages between 2.23 and 2.88 Ga and geochemical data reflect a provenance mainly represented by the 2.20 and 2.46 Ga tonalitic/granodioritic rocks of the Almas-Dianópolis terrane, exposed northwards of the study area. Zircon U-Pb geochronology and field observations suggest an age interval for the deposition of the precursor sediments of the Ticunzal Formation between 2.16 and 2.19 Ga. Raman spectroscopy analyses on graphite indicate high-crystallinity internal structures consistent with peak metamorphic temperatures between 620 and 630ºC. Trace element geochemical data of Ticunzal Formation samples suggest that precursor sediments were deposited in a continental arc-related basin, defining a setting consistent with an active mobile belt at the western margin of the São Francisco Craton during Rhyacian times, as inferred also from the characteristics of rocks from the Almas-Dianópolis terrane and the Aurumina Suite.

Keywords: São Francisco Craton; Brasília Fold Belt; Ticunzal Formation; sediment provenance; Lomagundi-Jatuli isotopic event; graphite thermometry.

5.1. INTRODUCTION

The São Francisco Craton in central-eastern Brazil represents a distinct lithospheric unit comprising Archean-Paleoproterozoic basement locally reworked to variable extents during Meso- to Neoproterozoic tectono-magmatic events, and covered by Proterozoic and Phanerozoic sequences (Almeida, 1967; 1977; Teixeira and Figueiredo, 1991; Trompette *et al*., 1992; Sial *et al*., 2009; Teixeira et al., 2017). Part of a single paleocontinental entity together with the West Congo Craton during pre-Mesozoic times,

the São Francisco Craton is at present limited by a number of Neoproterozoic mobile belts, including the Brasília, Rio Preto, Riacho do Pontal, Sergipana, Rio Pardo and Araçuaí fold belts (Almeida, 1977; 1981; Teixeira and Figueiredo, 1991; Alkmim *et al*., 1993; Sial *et al*., 2009). Two main Archean-Paleoproterozoic portions of the basement of the São Francisco Craton are currently exposed, corresponding to the Mineiro belt to the south, and a central-eastern domain that includes the Itabuna-Salvador-Curaçá belt and the Serrinha, Jequié and Gavião blocks (Barbosa and Sabaté, 2004; Alkmim and Noce, 2006; Barbosa et al., 2012).

The boundary between the São Francisco Craton and the Brasília Fold Belt is located in a region that, despite having experienced a growth in geological knowledge in recent decades, remains poorly understood in terms of geotectonic history and exact delimitation between the cratonic and mobile belt domains (Cordeiro *et al*., 2014; Sousa *et al*., 2016). Seismic and gravimetric data reveal similarities in lithospheric makeup between the northern part of the external zone of the Brasília Fold Belt and the adjacent portion of the São Francisco Craton, leading to proposals of establishing the actual western boundary of the São Francisco Craton at the limit between the Goiás Massif and the external zone of the Brasília Fold Belt (Assumpção *et al*., 2004; 2017; Berrocal *et al*., 2004; Soares *et al*., 2006). Such tectonic features, coupled with the presence of Early Paleoproterozoic metamorphic and magmatic units in the external zone of the Neoproterozoic Brasília Fold Belt, lead to conclude that another Paleoproterozoic basement domain of the São Francisco Craton exists at its western margin, in addition to those already known in the southern and central-eastern portions of the craton, as mentioned above.

In this work, new geochemical, geochronological, mineralogical and isotopic data of the medium-grade metasedimentary Ticunzal Formation in the northern portion of the external zone of the Brasília Fold Belt are presented as a contribution to the geological knowledge of the western margin of the São Francisco Craton, aiming to improve the understanding of the geotectonic characteristics of the São Francisco Craton as a whole, and therefore offering new perspectives for models of paleocontinental reconstruction and crustal evolution.

5.2. GEOLOGICAL SETTING

5.2.1. Regional framework

The Tocantins Province in central Brazil is commonly regarded as a Neoproterozoic orogenic feature marking amalgamation of three main continental blocks: the Amazonian Craton, the São Francisco Craton, and the Paranapanema block (Almeida *et al.*, 1981; Pimentel and Fuck, 1992; Strieder and Suita, 1999). Three main fold belts make up the Tocantins Province: the Paraguay and Araguaia fold belts on the southeastern and eastern margins of the Amazonian Craton, respectively, and the Brasília Fold Belt on the western margin of the São Francisco Craton. The Brasília Fold Belt extends for more than 1000 km between latitudes 10ºS and 20ºS and follows a general N-S trend (Fig. 5.1).

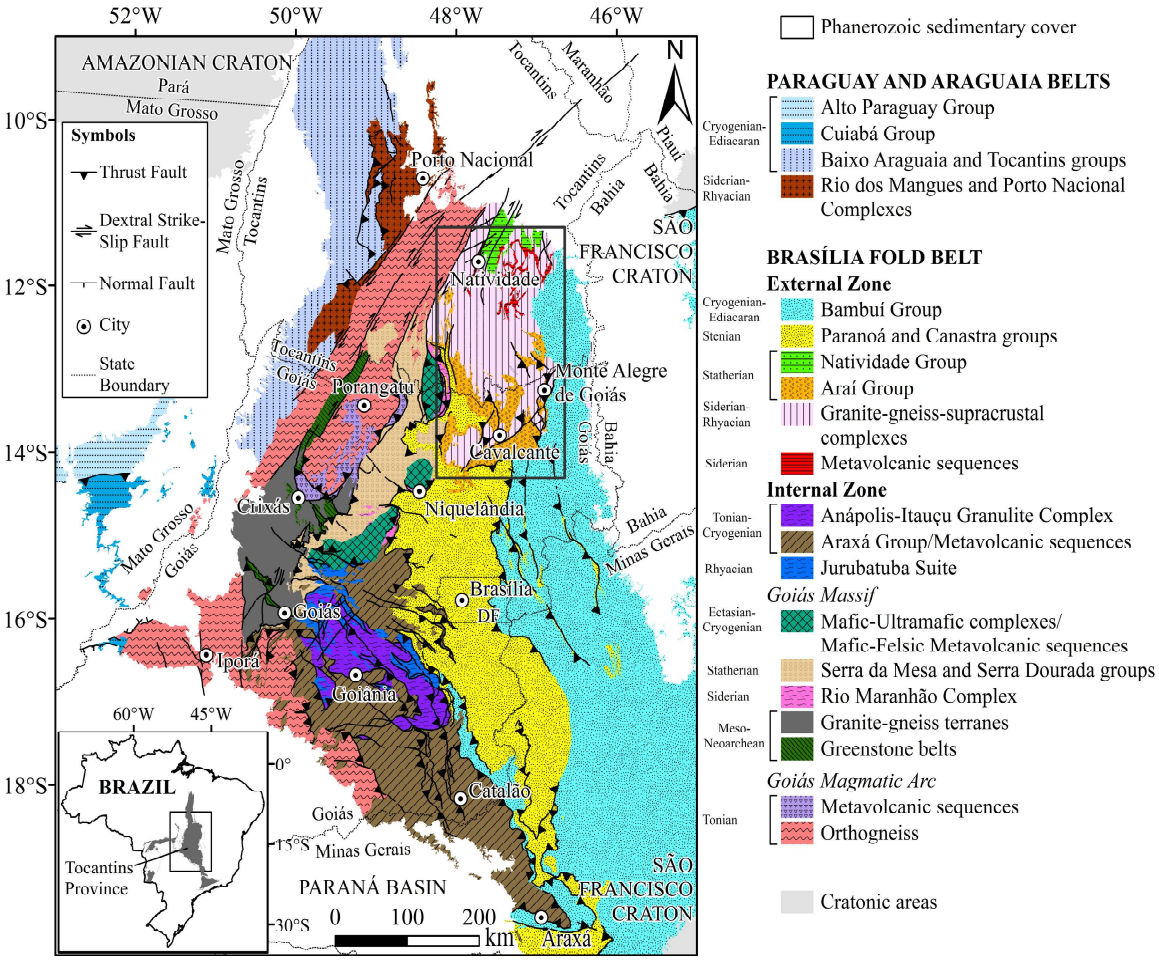

Fig. 5.1. Geological sketch of the Brasília Fold Belt. Modified after Pimentel *et al.* (2004). Studied area indicated by rectangle in the central-top right portion of the image.

Geologically, the Brasília Fold Belt is divided into a number of sectors (Fuck *et al.*, 1994; 2017; Dardenne, 2000; Pimentel *et al.*, 2004; Valeriano *et al.*, 2008), one of them

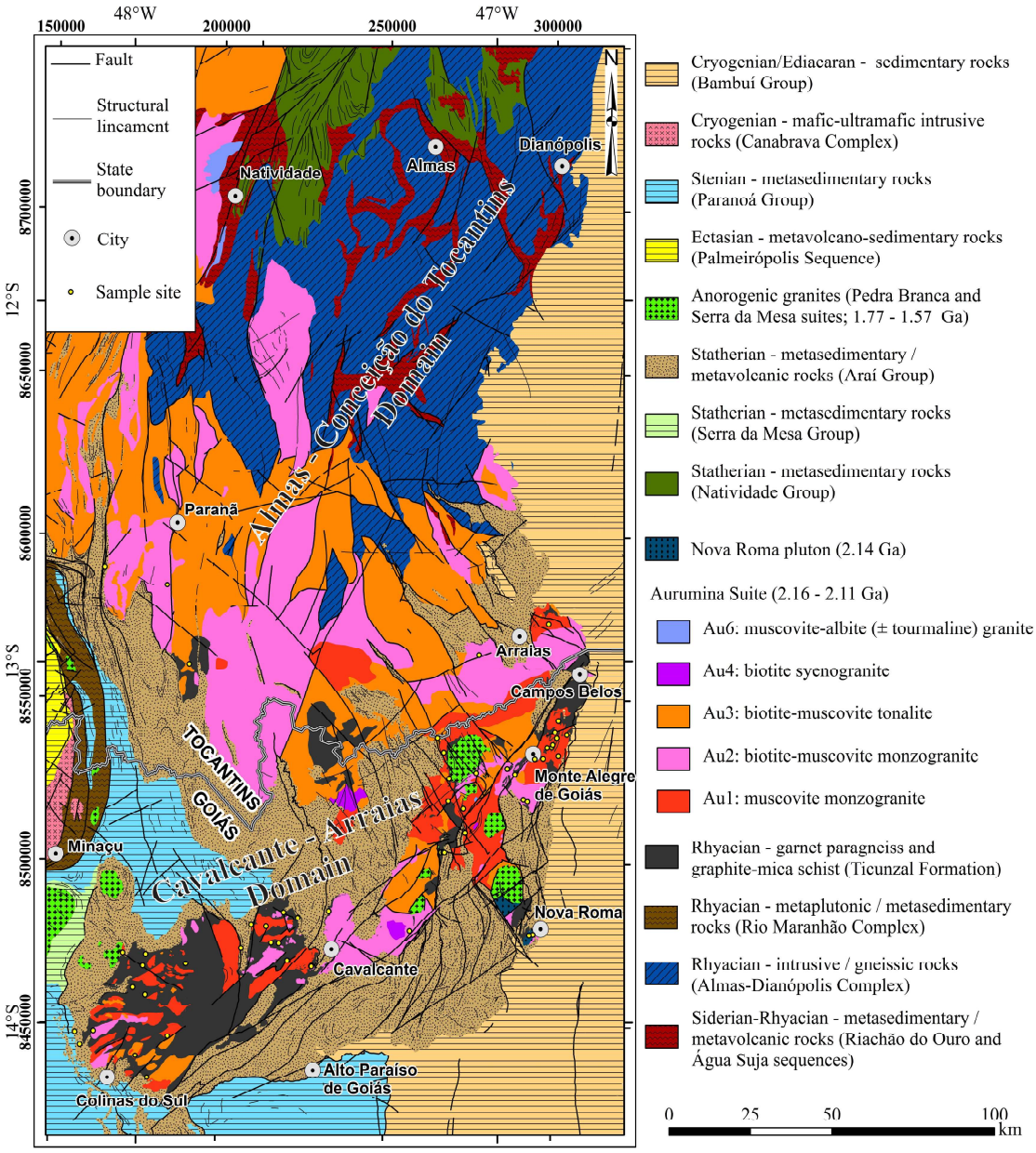

Fig. 5.2. Geological map of the studied area (see Fig. 5.1 for reference). Based on geological charts SC.23, SD.22, SD.23, SC.22-Z-D, SD.22-X-D, SD.23-V-A, SC.23-Y-C, SD.23-V-C-III, SD.23-V-C-V and SD.23-V-C-VI by the Brazilian Geological Survey (CPRM; http://geobank.cprm.gov.br/).

corresponding to an external zone composed in its northern part of 2.45-2.0 Ga basement (Fig. 5.2) referred to as the Cavalcante-Natividade block (Fuck *et al.*, 2014). Ages between 2.19 and 2.50 Ga have been obtained from tonalitic rocks belonging to the Almas-Conceição do Tocantins domain, within the northern part of this block (Fuck *et al.*, 2014; Sousa *et al.*, 2016). According to Cruz (2001) and Cruz *et al.* (2003), the Almas-Dianópolis granite-gneiss terrane in this sector encompasses the Ribeirão das Areias Complex (2.45 Ga) and a suite of peraluminous rocks (2.2 Ga), both of which contain tonalite, granodiorite, trondhjemite, and minor monzogranite. A suite of 2.2 Ga

metaluminous tonalite, granodiorite, trondhjemite, quartz diorite and quartz monzodiorite is also present, and the above-mentioned units intrude a greenstone sequence known as the Riachão do Ouro Group, which is composed of mafic to ultramafic volcanic rocks and a sequence of metasedimentary and felsic volcanic rocks (Costa, 1985; Cruz and Kujumjian, 1996; 1998).

The southern portion of the Cavalcante-Natividade block, namely the Cavalcante-Arraias domain (Fig. 5.2), is intruded by tin-bearing A-type granites of the Pedra Branca Suite and partially covered by the slightly deformed volcanic-sedimentary sequences of the Araí Group, with the latter two units representing a rifting event that took place at ~1.77 Ga. A later anorogenic magmatic event at ~1.58 Ga is represented by the tin-bearing granites of the Serra da Mesa Suite (Pimentel *et al*., 1991; 1999). Meso- to Neoproterozoic sedimentation in this domain is represented by the Paranoá and Bambuí groups in the southern and eastern portions, respectively. The basement of the Cavalcante-Arraias domain is essentially sialic crust comprising medium-grade paragneisses and schists, and peraluminous granites and tonalites. Due to poor mapping and a lack of geochemical data, the paragneisses, peraluminous granites and tonalites were formerly grouped into a granite-gneiss complex that extended through a large portion of the northern and western sectors of the Brasília Fold Belt (*e.g.*, Marini *et al*., 1984a, 1984b). Through detailed mapping campaigns and geochemical work, Botelho (1992) started separating some distinctive units based on compositional contrasts, thus leading to recognition of units such as the Aurumina Suite (Botelho *et al*., 1999) and the Nova Roma Pluton. The Aurumina Suite comprises peraluminous granites and tonalites that intrude Ticunzal Formation schists and paragneisses concordantly (Marini *et al*., 1978; 1984b; Fernandes *et al*., 1982).

5.2.2. Local geology

5.2.2.1. Ticunzal Formation

Identified for the first time by Marini *et al*. (1978), the Ticunzal Formation was originally described as a sequence of graphite-bearing mica-schist, meta-arkose and mica quartzite formerly referred to as Cachoeira das Éguas Formation. However, this name was later geographically restricted in use and the name Ticunzal Formation was adopted by Fernandes *et al*. (1982) in a more regional context. According to Marini *et al*. (1984b), schists that crop out in the Ticunzal Range (the type area of this formation located west

of Cavalcante) are up to 300 m thick in the upper portion of the sequence, while paragneisses of the lower portion are up to 200 m thick. The main rock types of the formation include paragneisses with varying amounts of biotite, muscovite, garnet and graphite, as well as quartz-muscovite schists, muscovite-garnet schists, tourmaline schists, chlorite-muscovite-quartz schists and graphite schists, the latter being the most representative lithology. Although rare, metaconglomerate and quartzite are also found in some sections of the formation.

The rocks of the Ticunzal Formation display a mineral assemblage consisting of chlorite, epidote, carbonate and fine-grained muscovite, which suggests retrograde metamorphism from amphibolite to greenschist facies. The presence of relict garnet and high-crystallinity carbonaceous matter (*i.e.*, graphite) also points to this. Chiastolite can also be found close to contacts with Aurumina Suite intrusions.

The Ticunzal Formation constitutes the oldest unit so far found in outcrop within the Cavalcante-Arraias domain with no older units found in outcrop to date. In thin section, paragneisses commonly display lepidoblastic foliation that is sometimes enhanced by parallel arrangements of quartz ribbons. This foliation, however, is not always evident, leading in some cases to confusion with granites of the Aurumina Suite. Garnet is useful in dismissing this confusion, as this mineral is common in the paragneisses but rare within the granitic rocks, except for a discrete body of garnet tonalite and some muscovite granites. The same applies to graphite, which often occurs as relatively abundant discrete fine lamellae in the paragneisses. The paragneisses are mainly composed of quartz (the most abundant mineral at >50%), plagioclase and microcline, the latter two commonly occurring in sub-equal amounts. Mica contents are seldom larger than 10%, and garnet is usually present as subhedral grains in amounts up to 5%. Accessory minerals include zircon, monazite, apatite, magnetite, ilmenite and graphite. Quartz and feldspars are anhedral, with the former typically displaying polygonization, sub-grain formation and sutured boundaries. Biotite and muscovite are mostly subhedral, with bands rich in these minerals commonly being finer grained than the quartz-feldspar layers (Fig. 5.3a). Granoblastic textures with characteristic triple junctions are sometimes found in quartz-rich layers, while garnet displays poikiloblastic texture with inclusions of quartz and biotite.

The schists are fine grained and display a well-developed lepidoblastic foliation that is sometimes accompanied by compositional banding defined by alternating mica-,

quartz- or graphite-rich layers (Fig. 5.3b). Muscovite and chlorite constitute > 50% of most schist varieties, with subordinate biotite locally attaining up to 10%. The remainder is usually composed of quartz, feldspar, iron oxides and graphite, the latter mineral varying from absent to dominant in graphite-schist samples. Quartz and muscovite porphyroblasts are sometimes observed, as well as rounded to sub-angular grains of accessory garnet and apatite. Quartz-rich bands commonly have a granoblastic texture, with individual grains displaying polygonization, sub-grain formation and sutured boundaries. In some cases, mylonitic features, such as S-C structures and sigmoidal porphyroclasts, are observed. Four deformational phases can be recognized in the Ticunzal Formation as inferred from structures such as crenulation foliation, truncated relict lepidoblastic foliation, and late brittle faults and joints.

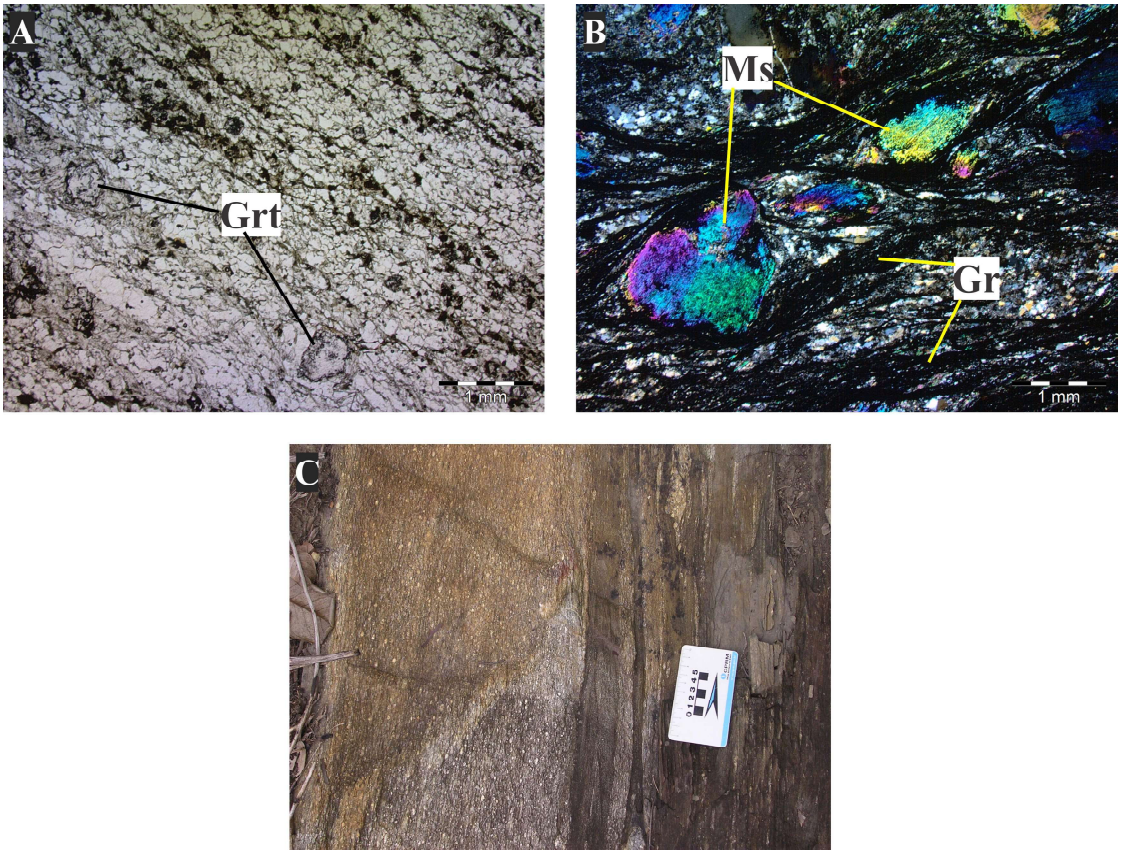

Fig. 5.3. Photomicrographs of some rock types. **A**: Garnet (Grt) -biotite paragneiss of the Ticunzal Formation. Note foliation in the SE-NW direction of the photograph and garnet porphyroblasts at both the bottom and left portions of the image. Parallel-polarized light. **B**: Muscovite (Ms) -graphite (Gr) schist displaying mica fish grains (center) within mylonitic foliation defined by anastomosing bands of quartz and graphite. Crossed-polarized light. **C**: Lit-par-lit intrusion of biotite-muscovite granite (light-colored rock) along foliation planes of Ticunzal Formation paragneiss (dark-colored rock).

Geochemically, the rocks display rather variable K_2O/N_2O and TiO_2/Zr ratios coupled with high MgO values, suggesting a mainly pelitic protolith with variable

contributions from graywackes and arkosic psammites. In addition, some conspicuous uranium-ore mineralizations intimately related to contacts with Aurumina Suite plutons have been reported. A hydrothermal model involving graphite-bearing Ticunzal Formation host rocks has been suggested for the origin of those mineralizations (Bogossian, 2012; Dardenne and Botelho, 2014). The age of the Ticunzal Formation is not well constrained, but it is regarded as likely early Paleoproterozoic (Rhyacian) in age, as suggested by T_{DM} ages between 2.0 and 2.8 Ga (Pimentel *et al*., 2004; Botelho *et al*., 2006a; Fuck *et al*., 2014).

5.2.2.2.Aurumina Suite and associated metaluminous rocks

The Aurumina Suite comprises several peraluminous rock types including, from oldest to youngest, muscovite monzogranite, muscovite-biotite monzogranite, biotite tonalite, biotite syenogranite, tourmaline leucogranite and tourmaline pegmatite. These facies have been labeled as Au1, Au2, Au3, Au4 and Au6, respectively (Alvarenga *et al*., 2007). Facies Au5 is recorded in just one outcrop and corresponds to migmatitic granites intimately associated with the Ticunzal Formation. Intrusions vary from syn- to post-kinematic in character as evidenced by *lit-par-lit* structures where members Au1 and Au2 intrude the Ticunzal Formation along foliation planes (Fig. 5.3c), as well as the existence of a N10-30E trending mylonitic foliation affecting both the granites and their metamorphic host rocks. Discordant styles of intrusion have also been observed, sometimes yielding breccia-like contact zones. Facies Au3, Au4, Au5 and Au6 typically show little to no deformation at all. Biotite-rich and/or graphite-bearing enclaves ranging from 0.5 to 30 cm in size are commonly found within rocks of this suite.

Granites belonging to the Au1, Au2, Au4 and Au5 facies are composed of quartz (~25-30%), microcline (30-35%), plagioclase (10-15%) and variable proportions of muscovite and biotite (together up to 20%), with the syenogranites of facies Au4 having the largest amounts of biotite. Opaque minerals occur in small amounts (<1%) and are represented almost exclusively by ilmenite, although in some cases small lamellae of graphite occur randomly in interstices between quartz and feldspar grains, or along cleavage planes in micas. Accessory minerals commonly include rounded apatite, monazite and zircon, and alteration minerals, such as sphene and leucoxene, are observed as overgrowths on ilmenite. Epidote occurs either in association with altered biotite masses or as rims on monazite. Tonalites and granodiorites of Au3 facies display a mineralogy similar to that of granites but with higher contents of plagioclase at the

expense of microcline. Phosphate accessory minerals, like apatite and monazite, are less common in these rock types and biotite is typically reddish in color while displaying, in some cases, a sagenitic texture due to rutile exsolution. Locally, garnet is an abundant phase (up to 10%) and occurs as small poikilitic grains. Au6 phases represent strongly differentiated residual liquids that are, in some instances, composed of albite as the dominant feldspar, along with tourmaline, cassiterite and tantalite. Muscovite is the only mica in these rocks, which are typically zircon-poor while having conspicuous amounts of manganese-rich fluorapatite and garnet.

Zircon U-Pb ages of Aurumina Suite samples vary between 2.12 and 2.18 Ga (Botelho *et al*., 2006a; Fuck *et al*., 2014; Corrêa *et al*., 2015; Sousa *et al*., 2016). These data are consistent with muscovite K-Ar ages (2129 ±26 Ma and 2006 ±26 Ma) and cassiterite U-Pb ages (2.277-2.023 Ma) obtained by Sparrenberger and Tassinari (1999) in peraluminous pegmatite samples from Monte Alegre de Goiás. More recently, Cuadros *et al*. (submitted) determined an age interval spanning from 2.11 to 2.16 Ga for the whole suite based on zircon U-Pb data. ε_{NdT} values typically vary between -1 and -3 (but with a full range between 0 and -7), and T_{DM} ages between 2.3 and 3.1 have been previously reported for the Aurumina Suite (Pereira, 2001; Botelho *et al*., 2002; 2006a; Fuck *et al*., 2014; Cuadros *et al*., submitted).

Despite being far less abundant than the rocks of either the Aurumina Suite or the Ticunzal Formation, some metaluminous units of mafic to intermediate composition are exposed between Colinas do Sul and Arraias. Except for the Nova Roma plutons, these units occur as stocks or dykes too small to be shown in Fig. 5.2.

The Nova Roma pluton is an undeformed composite body that intruded mica-graphite schists of the Ticunzal Formation and Au2 muscovite-biotite granites. In some instances, a progressive assimilation of the host rocks can be observed in outcrop, yielding a hybrid rock type between metaluminous and peraluminous. In thin section, this unit consists of plagioclase (50%), quartz (20-25%), biotite (0-15%) and hornblende (0-10%). Some biotite-bearing samples even display discrete graphite lamellae occurring along cleavage planes of biotite. Accessory minerals include zircon, apatite, allanite and ilmenite, while epidote, muscovite and chlorite occur as alteration products. Plagioclase appears as strongly altered coarse anhedral grains, while biotite is subhedral and has small apatite and zircon inclusions. Alvarenga *et al*. (2007) reported a U-Pb zircon age of 2.14 ± 0.007 Ga with a T_{DM} model age of 2.48 Ga and an ε_{NdT} value of -3.9 for this unit.

Close to Arraias, small plutons and dykes of quartz diorite and tonalite intrude Au2 biotite-muscovite granites and Au3 biotite tonalites. The melanocratic quartz diorites are composed of cummingtonite (30%), biotite (25%), plagioclase (40%) and quartz (5%). Ilmenite, chalcopyrite and zircon appear as accessory minerals, with hematite formed as alteration product of ilmenite. Cummingtonite appears as subhedral columnar crystals that in some instances have small inclusions of plagioclase. Biotite is typically anhedral and displays a characteristic compositional zoning in which the cores possess a stronger reddish color than the rims. Plagioclase occurs as anhedral altered grains displaying lobate borders. Cuadros *et al*. (submitted) obtained a magmatic crystallization age on zircon of 2.15 ± 0.01 Ga for one of the cummingtonite-bearing plutons.

Small plutons and dykes of metagabbro and metaperidotite intrude the Ticunzal Formation close to Colinas do Sul. In general, these rocks display strong retrograde metamorphism, rendering it difficult to recognize their primary mineralogy. Variable amounts of tremolite/actinolite, plagioclase, talc and biotite are found in these rocks, with epidote, leucoxene, titanite and zoisite as typical alteration phases. In some instances, quartz appears as an alteration phase (5-10%), but it is also possible that this mineral was part of the primary mineral assemblage. The original textures of these mafic/ultramafic rocks are pervasively transformed, but in some cases, it is possible to recognize relicts of cumulate textures where plagioclase is more abundant, as well as triple junctions in amphibole aggregates.

5.3. ANALYTICAL METHODS

5.3.1. Major and trace element geochemistry

Chemical analyses of rock powder were performed by AcmeLabs Ltd. following 4A and 4B routines. The 4A routine involved ICP-AES analysis of major and minor elements after lithium metaborate/tetraborate fusion and dilute HNO_3 digestion. In 4B routine, trace elements of selected samples were analyzed by ICP-MS following the same preparation as in 4A with digestion in aqua regia of an additional separate split. Several samples were analyzed by equivalent methods during previous projects in which only concentrations of a select group of trace elements were determined (Table 5.1).

5.3.2. Zircon U-Pb geochronology

The methodology and equipment set-up used for the U-Pb geochronology closely followed that presented by Bühn *et al*. (2009), to whom the reader is referred for further details. Geochronological U-Pb analyses were carried out at the geochronology laboratory of the University of Brasília using a Thermo Finnigan Neptune multicollector inductively coupled plasma mass spectrometer. The input of mineral substance into the spectrometer was achieved by means of the laser ablation technique using a New Wave 213 μm Nd-YAG solid-state laser. A beam diameter of 30 μm and a laser energy of ~3.1 J/cm^2 at a frequency of 10 Hz were used. Samples were inserted into a He-flushed laser chamber with a gas flux between 0.35 and 0.45 l/min. The removal of ^{204}Hg from the He flux was achieved by passing the gas through glass tubes containing gold-coated quartz particles intended to minimize the isobaric interference with ^{204}Pb, thus allowing calculation of common lead corrections. For standard and sample analysis, the signals were collected in a single block with 40 cycles of 1.049 s each, with reading of the signals starting after they had attained their maximum following the onset of ablation.

The standard-sample bracketing technique was applied by analyzing one standard spot and one blank every eight sample spots, thus accounting for instrumental drift. The GJ-1 zircon provided by the ARC National Key Centre for Geochemical Evolution and Metallogeny of Continents (GEMOC) of Australia was used as standard. The reference ages of the standard are as follows: ^{207}Pb/^{206}Pb age = 608.6 ± 1.1 Ma, ^{206}Pb/^{238}U age = 600.4 ± 1.8 Ma, and ^{207}Pb/^{235}U age = 602.1 ± 3.0 Ma (Jackson *et al*., 2004). Data reduction was achieved using a spreadsheet developed at the geochronology laboratory of the Brasília University. This spreadsheet allowed evaluation of isotope ratios for every cycle on a 2σ rejection basis. The corrected ratios and associated calculated ages were displayed using Isoplot 3.75 (Ludwig, 2012).

5.3.3. Sm-Nd isotope geochemistry

All the whole-rock Sm and Nd isotope analyses were performed at the geochronology laboratory of the Brasília University. The analytical procedures applied in this study to measure the ^{147}Sm/^{144}Nd and ^{143}Nd/^{144}Nd isotope ratios were those described by Gioia and Pimentel (2000). Rock samples were ground to a powder and dosed with ^{149}Sm and ^{150}Nd spike solutions. The separation of Sm from Nd was accomplished using cation exchange columns followed by evaporation of the obtained fractions with two drops of 0.025 N H_3PO_4. The residue was dissolved in 1 μl of 5% distilled HNO_3 and

loaded onto a double Re filament assembly. The mass spectrometer used was a Finnigan MAT 262 with 7 collectors in static mode. The uncertainties for $^{147}Sm/^{144}Nd$ and $^{143}Nd/^{144}Nd$ ratios were better than ±0.2% (2σ) and ±0.0064% (2σ), respectively, based on analysis of the BHVO-1 international rock standard. The $^{143}Nd/^{144}Nd$ ratio was normalized using $^{146}Nd/^{144}Nd=0.7219$, and the employed decay constant was 6.54×10^{-12} y^{-1} (Lugmair and Marti, 1978).

5.3.4. Raman spectroscopy

Raman analyses of graphite followed the methodology presented by Beyssac *et al*. (2002). Standard polished thin sections of rocks containing graphitic material were studied petrographically in order to choose graphite lamellae completely contained within colorless minerals such as quartz and muscovite, with 20 to 30 lamellae being analyzed per sample. Raman spectra were obtained at the Nanoscience and Nanobiotechnology Center of the Physics Institute of the University of Brasília using a T64000 Jobin-Yvon triple spectrometer coupled with an optical microscope having a 50X objective that allowed a ~5 μm diameter laser beam. Signal was generated after excitation using an Ar Coherent CW ion laser with a wavelength of 514.5 nm at room temperature. Signal was collected using a CCD-type detector cooled with liquid nitrogen. After acquisition, fluorescence background was subtracted from Raman spectra using the algorithm proposed by Cadusch *et al*. (2013) under second-order, single-weighted mode with a smoothing parameter $\gamma=10^6$. Spectra modeling and calculation were carried out using software PeakFit v. 4.12 under Voight function configuration.

5.4. RESULTS

5.4.1. Geochemistry

Results of geochemical analyses are summarized in Table 5.1. Paragneisses and schists of the Ticunzal Formation display a fairly wide variation in composition as evidenced by their SiO_2 contents ranging between 42 and 82 wt.%, although values between 65 and 75 wt.% are dominant. Fe_2O_3/K_2O and SiO_2/Al_2O_3 ratios point to shale, wacke and arkose as main geochemical lithotypes, without a clear correspondence between the latter subdivision and the petrographic schist-paragneiss classification (Fig. 5.4a). On the other hand, K_2O/Na_2O ratios are moderate to high (0.45-141.5), with schists displaying a tendency towards higher ratios than paragneisses (Figs. 5.5a and 5.5b). Low

Table 5.1. Whole-rock major and trace element data. Empty entries correspond either to values below detection limits, or unanalyzed elements. Major oxides in wt.% and trace elements in ppm.
S: Schist; **P**: Paragneiss.

Sample	Rock Type	Location		SiO_2	TiO_2	Al_2O_3	Fe_2O_3	MnO	MgO	CaO	Na_2O	K_2O	P_2O_5	LOI	TOT/C	TOT/S	Sum	La	Ce	Pr	Nd	Sm	Eu	Gd	Tb	Dy	Ho	Er	Tm	Yb	Lu	Sc	Th	Zr	Cr	Ni
		Lat. (S)	Long. (W)																																
AUFC-11-3	S	13° 22' 58.6"	46° 55' 41.9"	48.94	0.97	24.30	10.46	0.09	2.19	0.14	0.12	7.96	0.08	4.50	0.03		99.78	67.3	137.4	15.84	59.2	10.22	1.14	8.82	1.34	7.43	1.45	4.06	0.64	4.01	0.62	22	25.7	269.8	109.47	47.4
AUFC-12-2	S	13° 16' 12.6"	46° 53' 47.3"	79.93	0.36	9.57	3.36	0.02	1.00	0.01	0.07	3.84	0.03	1.70			99.89	22.8	44.7	4.71	17.4	2.53	0.35	1.66	0.25	1.33	0.31	0.97	0.17	1.16	0.21	7	7.5	105.5	143.68	15.0
AUFC-13-1	S	13° 14' 22.1"	46° 50' 58.0"	61.14	0.54	18.33	7.76	0.07	1.69	0.05	0.24	3.92	0.12	5.90	0.97		100.73	42.2	84.2	9.36	35.2	6.58	1.14	6.07	0.92	5.16	1.10	3.22	0.47	2.90	0.47	16	12.5	147.8	75.26	91.7
AUFC-13-2	S	13° 14' 22.1"	46° 50' 58.0"	73.14	0.54	15.45	1.52		0.56	0.04	0.11	4.76	0.09	3.60	1.62		101.43	41.2	82.5	8.25	27.8	4.14	0.77	3.17	0.48	2.59	0.57	1.68	0.26	1.70	0.31	11	12.2	197.1	82.10	1.1
99-VIII-48	S	13° 13' 55.2"	46° 50' 48.2"	77.40	0.43	12.99	3.32	0.02	0.86	0.20	0.02	2.83	0.13	1.62			99.82	26.0	61.0			4.50	2.00		0.50					2.00	0.40		8.6	327.0	30.11	16.0
99-VIII-67A	S	13° 11' 45.8"	46° 50' 25.7"	81.70	0.51	11.80	0.75	0.00	0.54	0.54	0.05	2.78	0.05	0.91			99.63	19.0	35.0			2.20											8.6	333.0	41.05	0.0
99-IX-189	S	13° 09' 57.7"	46° 49' 52.1"	65.20	0.70	17.54	7.18	0.06	1.98	0.27	0.48	4.03	0.08	1.58			99.10	57.0	110.0		25.3	7.30	2.00	6.12	1.10	1.70				4.00	0.40		14.0	242.0	73.89	34.0
98-III-17	S	13° 41' 31.2"	47° 27' 55.9"	65.98	0.68	16.66	7.28	0.03	2.29	0.12	0.86	2.76	0.07	3.05			99.78																	252.0	49.95	12.0
98-III-18a	S	13° 41' 30.3"	47° 27' 57.2"	63.21	1.12	15.76	10.43	0.01	1.55	0.15	0.37	2.93	0.20	2.85			98.58																	167.0	52.00	10.0
98-III-123	S	13° 42' 30.3"	47° 33' 2.5"	70.30	0.46	13.96	3.69	0.00	2.90	0.59	1.37	2.95	0.03	2.46			98.71																	119.0	49.26	5.0
98-V-63b	S	13° 50' 35.1"	47° 30' 48.9"	60.43	1.07	21.44	4.81	0.01	2.45	0.21	0.73	5.35	0.10	3.21			99.81																	130.0	46.53	4.0
98-VI-68	S	13° 47' 39.6"	47° 42' 31.2"	60.13	0.78	19.04	8.48	0.05	3.91	0.50	0.43	3.47	0.09	3.55			100.43																	155.0	62.26	48.0
98-VI-179c	S	13° 49' 44.1"	47° 34' 42.8"	54.71	1.05	22.85	6.63	0.04	3.53	0.83	0.87	4.82	0.10	4.19			99.62																	134.0	56.79	21.0
98-VII-4	S	13° 46' 53.2"	47° 36' 14.7"	64.61	0.75	16.62	5.52	0.07	2.50	0.72	1.76	2.69	0.31	3.55			99.10																	137.0	46.53	28.0
98-VIII-8	S	13° 41' 42.0"	47° 35' 26.3"	51.88	0.98	15.79	10.41	0.01	5.78	6.58	2.74	1.23	0.13	4.12			99.65																	69.0	82.10	21.0
98-VIII-36b	S	13° 43' 46.5"	47° 40' 48.9"	64.39	0.51	19.48	2.98	0.01	1.62	0.92	1.41	5.46	0.31	2.99			100.08																	34.0	2.74	2.0
01-V-124	S	12° 53' 47.0"	46° 51' 28.2"	69.84	0.68	12.97	7.86	0.08	1.97	0.19	0.09	2.78	0.16	3.10			99.72	19.6	40.5	4.86	18.2	4.20	0.87	4.34	0.65	3.12	0.67	1.57	0.22	1.48	0.25	9	11.5	175.6	32.77	28.0
95-II-134	S	13° 44' 47.7"	47° 14' 33.9"	72.19	0.41	15.36	2.17	0.00	1.05	0.23	0.34	6.09	0.16	2.39			100.39																	283.0	0.68	0.0
95-V-26	S	13° 31' 48.4"	47° 09' 21.2"	72.49	0.33	9.57	11.01	0.00	3.10	0.05	0.30	1.22	0.04	3.28			101.39																	77.0	44.47	52.0
95-V-28	S	13° 31' 46.7"	47° 08' 58.2"	66.76	0.71	15.47	7.18	0.00	3.08	0.14	0.69	3.33	0.06	3.51			100.93																	172.0	53.37	35.0
95-V-29	S	13° 31' 49.7"	47° 08' 45.7"	64.83	0.78	17.32	4.86	0.00	3.75	0.71	1.04	4.07	0.11	3.28			100.75																	151.0	65.00	23.0
05-I-059	S	13° 12' 42.3"	47° 09' 54.3"	66.29	0.48	17.23	3.64	0.07	1.29	2.10	1.85	4.63	0.17	2.20			99.95	27.1	63.4	6.62	25.7	4.20	1.22	3.35	0.58	1.98	0.56	1.20	0.20	0.94	0.17	7	7.4	128.0		2.9
09-VII-72	S	13° 54' 9.5"	48° 00' 28.0"	74.14	0.06	15.30	1.08	0.04	0.44	0.78	4.74	2.24	0.17	0.90	0.03		99.92	22.5	16.1	4.58	18.2	3.69	1.57	3.71	0.56	2.91	0.58	1.64	0.23	1.27	0.17		1.7	32.1	14.00	1.2
09-XI-115 B	S	13° 50' 34.1"	47° 58' 48.4"	59.42	0.59	17.63	6.16	0.09	1.89	2.99	0.65	5.38	0.82	4.10	0.13		99.85	34.5	75.5	8.18	31.0	5.40	1.10	4.07	0.73	4.35	0.92	2.86	0.42	2.87	0.44	15	10.2	178.2	109.00	31.3
09-XIV-X	S	14° 05' 28.1"	48° 00' 4.5"	65.83	0.82	15.26	5.03	0.08	2.17	1.99	3.18	3.56	0.34	1.40			99.66	73.6	151.2	15.37	52.3	6.28	1.25	3.07	0.40	1.57	0.22	0.52	0.07	0.43	0.06	8	7.2	333.2	62.00	32.7
TF10-III 247	S	12° 44' 13.7"	48° 05' 3.3"	69.75	0.51	15.56	2.07		1.87	0.02	0.10	6.07	0.03	3.90	1.10	0.19	101.17	37.1	83.6	8.57	28.1	3.64	0.83	2.32	0.43	2.63	0.58	1.77	0.28	1.76	0.28	10	9.1	316.2	82.08	16.2
AUFC-19-1	P	13° 17' 54.5"	46° 58' 22.2"	69.75	0.46	15.24	4.01	0.06	1.22	2.44	3.06	2.29	0.13	1.10	0.09		99.85	47.7	88.4	9.79	35.1	6.27	1.17	5.08	0.69	3.74	0.69	1.96	0.29	2.02	0.30	8	17.5	190.6	41.05	17.7
AUFC 30-1	P	13° 50' 31.6"	47° 58' 49.5"	80.31	0.44	9.71	3.45	0.09	0.93	0.79	1.88	1.42	0.05	0.80	0.05		99.92	34.6	69.3	7.18	24.7	4.11	0.91	3.24	0.47	2.62	0.55	1.67	0.24	1.65	0.25	7	11.0	238.3	54.72	16.4
AUFC 35-1	P	13° 50' 14. 7"	47° 51' 42.4"	74.49	0.11	14.78	0.95	0.01	0.24	0.55	3.44	4.20	0.19	1.00			99.96	9.6	19.0	2.25	8.2	2.21	0.21	2.12	0.33	1.69	0.20	0.46	0.06	0.35	0.04	2	3.4	50.5		0.5
AUFC 35-2	P	13° 50' 14. 7"	47° 51' 42.4"	66.74	0.65	16.09	3.95	0.04	0.70	1.43	2.95	5.33	0.40	1.50	0.08		99.86	139.9	347.0	41.02	146.2	20.68	1.41	9.78	0.80	2.69	0.26	0.62	0.09	0.63	0.10	3	83.8	395.7	20.52	5.0
AUFC 39-1	P	13° 24' 31.7"	47° 05' 37.8"	67.74	0.50	16.96	2.67	0.03	0.81	1.17	5.36	2.64	0.33	1.60	0.08		99.89	94.8	203.7	23.82	87.8	14.63	1.48	8.44	0.80	3.23	0.46	1.25	0.18	1.06	0.17	3	43.4	277.2	20.52	8.7
99-VI-42	P	13° 18' 49.1"	46° 57' 3.7"	53.00	0.98	23.05	10.02	0.12	2.54	0.29	0.44	4.23	0.07	4.68			99.42	65.0	130.0			9.00	2.00	0.00	0.80	0.00				4.00	0.40		17.0	363.0	80.74	22.0
98-III-121	P	13° 42' 35.2"	47° 33' 5.7"	73.72	0.42	11.29	3.83	0.01	4.19	0.79	1.93	1.43	0.05	2.49			100.15																	74.0	27.37	5.0
98-V-61a	P	13° 50' 43.2"	47° 30' 50.8"	75.31	0.77	11.61	4.17	0.04	1.48	0.73	1.73	2.67	0.15	1.63			100.29																	200.0	65.68	9.0
01-I-94	P	12° 58' 59.7"	47° 03' 0.8"	65.18	0.42	17.28	5.57	0.08	1.43	0.52	2.70	3.42	0.16	3.10			99.86	46.6	87.3	9.91	36.2	6.80	1.09	5.67	0.82	4.72	0.92	2.34	0.42	2.18	0.32	11	7.4	99.2	32.77	27.0
05-II-002	P	13° 15' 11.0"	47° 08' 52.1"	70.72	0.31	15.08	3.06	0.06	0.83	4.23	2.19	1.72	0.10	1.40			99.70	74.3	128.6	13.77	45.6	7.30	1.07	6.50	0.95	4.60	1.20	3.15	0.48	2.65	0.46	6	35.0	206.2		5.9
05-VI-202A	P	13° 23' 11.6"	47° 08' 8.0"	76.14	0.49	10.75	4.63	0.08	0.99	1.96	2.01	1.29	0.07	1.40			99.81	32.7	65.7	7.29	26.0	4.50	0.91	3.21	0.55	2.64	0.56	1.74	0.21	1.52	0.29	8	8.8	177.0		20.5
05-VI-210	P	13° 19' 27.9"	47° 07' 58.6"	76.33	0.48	10.71	4.66	0.08	0.98	1.91	1.96	1.27	0.07	1.50			99.95	34.3	69.1	7.38	29.0	5.40	1.09	3.49	0.54	2.49	0.59	1.90	0.28	1.91	0.28	8	8.5	211.7		22.9
05-VII-280	P	13° 18' 35.9"	47° 03' 29.5"	66.95	0.51	15.58	4.94	0.09	1.34	1.86	3.28	3.71	0.12	1.30			99.68	45.9	89.7	9.10	33.3	6.00	1.35	4.70	0.97	4.80	0.99	2.91	0.43	2.93	0.44	10	21.8	241.4		10.3
05-VIII-135A	P	13° 28' 33.6"	47° 05' 20.7"	70.78	0.57	13.75	4.93	0.06	1.39	0.59	1.36	4.02	0.06	2.40			99.91	38.1	85.8	8.76	31.7	5.60	1.13	4.11	0.71	3.50	0.62	1.95	0.24	1.97	0.25	10	11.0	214.8		29.0
05-XV-099	P	13° 45' 25.3"	46° 54' 7.2"	76.33	0.22	13.57	2.00	0.01	0.42	0.11	0.13	3.78	0.12	3.20			99.89	41.4	79.6	9.38	32.6	7.10	1.16	4.41	0.55	1.92	0.18	0.41	0.10	0.26	0.06	2	11.1	126.6		23.9
09-V-140	P	13° 48' 23.1"	48° 02' 7.2"	66.23	0.63	15.95	6.14	0.07	1.48	0.26	1.38	5.07	0.14	2.50			99.85	34.4	89.6	9.83	37.6	6.77	0.68	4.93	0.78	4.24	0.79	2.44	0.34	2.29	0.32	14	12.2	242.3	116.00	23.7
09-IX-48	P	14° 01' 17.8"	48° 07' 0.9"	66.57	0.62	15.68	6.11	0.08	1.85	0.55	1.52	4.45	0.06	2.30	0.39		100.18	53.6	83.6	12.24	46.6	7.62	1.30	6.57	1.08	5.80	1.10	3.12	0.45	3.10	0.42	14	11.8	212.4	82.00	28.0
09-IX-88	P	14° 03' 34.4"	48° 09' 15.2"	71.14	0.37	10.51	4.85	0.20	2.65	4.42	2.11	1.26	0.06	2.20	0.80		100.57	31.4	63.5	6.99	26.9	4.82	0.88	4.65	0.80	4.29	0.81	2.36	0.33	2.11	0.32	11	8.0	229.1	82.00	51.7
09-IX-97	P	14° 01' 26.8"	48° 10' 5.1"	75.12	0.47	11.54	4.28	0.08	1.16	1.85	3.10	1.64	0.08	0.50	0.39		100.21	31.3	60.0	7.13	27.4	4.38	0.99	3.82	0.65	3.68	0.78	2.34	0.34	2.15	0.32	10	7.9	220.9	103.00	23.8
09-XI-115 A	P	13° 50' 34.1"	47° 58' 48.4"	43.75	1.20	30.15	6.53	0.16	1.91	0.14	0.69	8.98	0.08	6.00	0.16		99.75	34.3	94.1	9.39	33.7	6.44	0.91	4.77	0.89	4.91	1.01	3.21	0.51	3.42	0.53	24	14.1	495.2	137.00	19.4
09-XI-171 A	P	13° 48' 38.2"	47° 58' 18.3"	48.69	1.02	23.30	9.36	0.13	2.76	1.53	0.53	7.35	0.47	4.50	0.27		99.91	40.1	103.0	10.58	38.9	7.35	1.14	5.79	1.06	6.28	1.24	3.91	0.59	4.01	0.60	23	21.7	270.0	157.00	45.6
09-XI-171 B1	P	13° 48' 38.2"	47° 58' 18.3"	72.62	0.15	14.99	1.14		0.35	0.39	3.03	5.80	0.18	1.20	0.02		99.87	30.7	59.8	6.66	24.9	4.07	0.60	3.07	0.44	1.78	0.25	0.66	0.08	0.46	0.07	2	4.6	67.3	14.00	2.4
09-XI-171 B2	P	13° 48' 38.2"	47° 58' 18.3"	45.86	1.30	26.54	9.06	0.16	2.57	0.76	0.52	7.82	0.28	4.80	0.41		100.08	29.3	103.9	8.13	30.1	6.13	0.91	4.87	1.01	6.32	1.37	4.49	0.75	5.09	0.78	26	20.1	409.2	171.00	31.0
09-XI-188	P	13° 55' 23.1"	47° 58' 24.3"	45.40	1.18	28.19	7.88	0.14	2.39	0.48	0.70	8.30	0.20	4.80	0.31		99.97	43.4	129.8	11.99	43.4	8.35	1.18	6.38	1.15	6.29	1.18	3.49	0.55	3.72	0.56	25	24.8	405.0	137.00	30.8
09-XIII-72 A	P	13° 50' 13.5"	47° 51' 40.6"	71.48	0.17	16.00	1.30		0.30	0.66	3.97	4.63	0.21	1.20			99.92	31.6	69.7	8.01	28.1	4.32	0.55	2.44	0.33	1.25	0.14	0.33	0.04	0.27	0.03		9.2	72.5	14.00	1.0

Table 5.1. (Continued).

Sample	Rock Type	Location		SiO_2	TiO_2	Al_2O_3	Fe_2O_3	MnO	MgO	CaO	Na_2O	K_2O	P_2O_5	LOI	TOT/C	TOT/S	Sum	La	Ce	Pr	Nd	Sm	Eu	Gd	Tb	Dy	Ho	Er	Tm	Yb	Lu	Sc	Th	Zr	Cr	Ni
		Lat. (S)	Long. (W)																																	
09-XIII-72 B	P	13° 50' 13.5"	47° 51' 40.6"	70.29	0.38	15.98	2.20	0.03	0.43	0.89	3.49	4.64	0.18	1.40	0.05		99.96	66.8	188.8	22.04	79.1	13.15	1.22	7.12	0.98	3.57	0.40	0.91	0.11	0.73	0.10	3	55.4	213.3	14.00	2.6
09-XVI-025	P	14° 02' 15.4"	47° 54' 43.1"	60.59	1.11	17.04	7.38	0.12	2.30	3.67	1.86	4.17	0.27	1.20	0.06		99.77	42.1	83.2	9.94	37.3	6.63	1.61	4.89	0.74	3.59	0.66	1.71	0.25	1.49	0.22	10	6.2	202.6	21.00	8.8
09-XIV-90	P	14° 09' 4.3"	47° 58' 8.1"	65.48	0.69	16.26	6.06	0.05	2.26	0.17	0.74	5.59	0.10	2.40			99.80	51.6	105.0	14.60	54.0	9.60	1.61	6.20	1.01	4.98	0.82	2.38	0.39	2.53	0.38	17	11.5	215.8	116.00	42.4
TF10-III.41	P	12° 41' 32.9"	48° 13' 28.4"	66.95	0.73	14.45	6.42	0.19	1.88	2.11	2.62	2.97	0.10	1.40	0.31		100.13	26.8	59.3	6.06	21.6	3.96	1.44	3.72	0.78	5.13	1.15	3.43	0.57	3.61	0.57	18	7.1	273.0	88.92	42.4
TF10-VI.237B	P	12° 47' 13.0"	47° 54' 42.0"	60.38	0.57	16.76	8.57	1.54	1.84	3.05	2.48	1.44	0.12	3.10	1.64		101.49	33.4	90.6	7.95	29.5	5.55	1.05	4.67	0.80	4.49	0.93	2.53	0.37	2.44	0.36	17	12.2	131.5	95.76	64.8
TF10-XVI.38	P	13° 00' 24.4"	47° 51' 3.9"	68.54	0.42	15.68	4.43	0.15	1.24	1.18	3.60	3.17	0.08	1.40	0.15		100.04	48.3	95.3	9.85	34.5	5.83	1.20	4.77	0.81	4.56	0.97	2.90	0.46	2.91	0.46	9	32.6	229.2	54.72	19.5

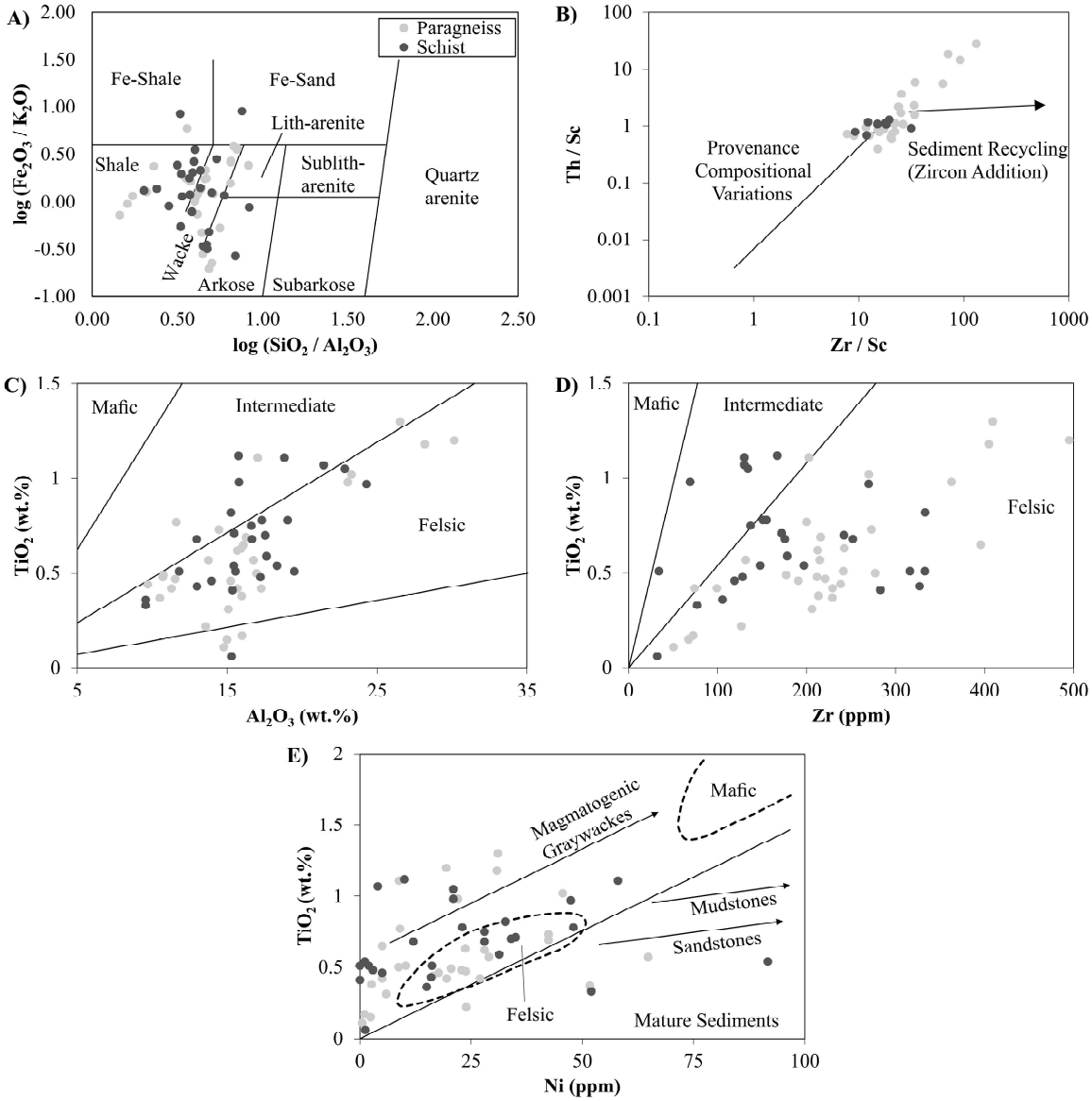

Fig. 5.4. Geochemical features of the analyzed samples. **A**: Logarithmic plot of Fe_2O_3/K_2O vs SiO_2/Al_2O_3 of Herron (1988). **B**: Zr/Sc vs. Th/Sc plot of McLennan *et al*. (1993). TiO_2 vs. Al_2O_3 (**C**) and TiO_2 vs. Zr (**D**) diagrams for provenance composition discrimination of Hayashi *et al*. (1997). **E**: TiO_2 vs. Ni diagram for provenance composition discrimination of Floyd *et al*. (1989; 1991).

TiO_2 and Ni coupled with rather high Al_2O_3 and Zr contents in all Ticunzal Formation samples are compatible with provenance dominantly felsic in composition (Figs. 5.4c, 5.4d and 5.4e). This is in agreement with the evolved provenance compositions inferred from high Th/Sc ratios that, along with intermediate Zr/Sc ratios, indicate that the sediments that gave origin to the Ticunzal Formation were not substantially reworked (Fig. 5.4b). Samples AUFC-35-2, AUFC-39-1, 05-XV-099 and 09-XIII-72B are exceptions to the latter case as they display higher Th/Sc (> 5) and Zr/Sc (> 35) ratios. A close inspection of this group of samples in thin section reveals that such geochemical

features are due to higher amounts of zircon and/or monazite as compared to the rest of samples of the Ticunzal Formation.

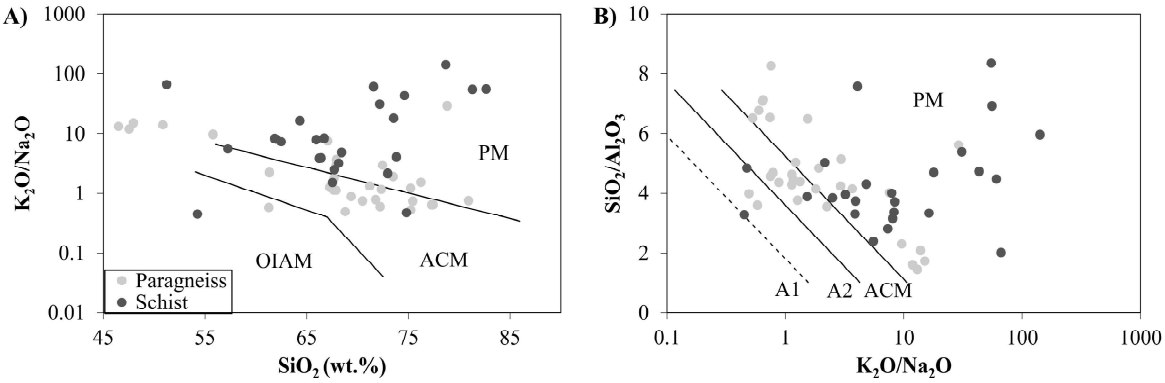

Fig. 5.5. Geochemical features of the analyzed samples. K_2O/Na_2O vs. SiO_2 (**A**) and SiO_2/Al_2O_3 vs. K_2O/Na_2O (**B**) tectonic discrimination diagrams of Roser and Korsch (1986). PM: passive margin; ACM: active continental margin; OIAM: oceanic island arc margin; A1: arc (basaltic and andesitic debris); A2: evolved arc (felsic debris).

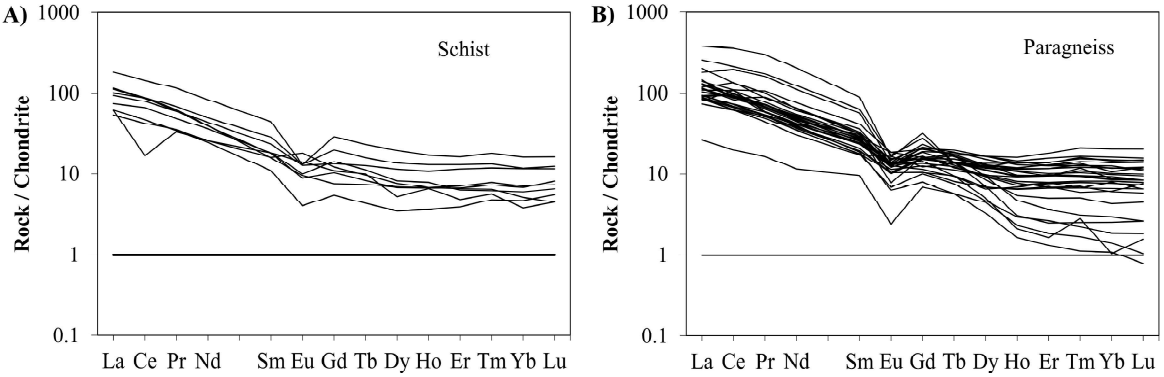

Fig. 5.6. REE patterns of Ticunzal Formation schists (**A**) and paragneisses (**B**). Data normalized to chondrite of Evensen *et al*. (1978).

Two main REE patterns can be identified in the paragneisses (Fig. 5.6b), one of them being characterized by HREE contents lower than five times that of the reference chondrite (samples AUFC-35-1, AUFC-35-2, AUFC-39-1, 05-XV-099, 09-XI-171B1, 09-XIII-72A and 09-XIII-72B), strong negative Eu anomalies (Eu/Eu* between 0.3 and 0.6) and rather high amounts of LREE ($[La/Yb]_N$ between 60 and 150), with the exception of samples AUFC-35-1, 09-XIII-72A and 09-XI-171B1 which have rather low LREE contents (Fig. 5.6b). The second pattern displays HREE amounts more than five times those of the reference chondrite, Eu anomalies varying from moderately negative to slightly positive and $(La/Yb)_N$ ratios between 3 and 19. On the other hand, schists display a single pattern that is similar to that of the HREE-enriched paragneisses, with only sample 09-VII-72 displaying a negative Ce anomaly (Fig. 5.6a).

5.4.2. U-Pb geochronology

Zircon crystals from three paragneiss samples and one schist sample were analyzed by MC-LA-ICP-MS (Table 5.2), with only those from sample AUFC-19-1 having been imaged by cathodoluminescence (CL) before laser ablation analyses (Appendix II[2]). Zircon grains from the paragneiss samples are relatively small (60-130 µm), anhedral, translucent and reddish to pink in color. Elongated shapes are as common as equidimensional ones, with both types displaying rounded smooth borders. Inclusions of quartz, biotite, microcline, albite, garnet and sphene are found within zircon grains, and CL reveals that cores displaying typical oscillatory zoning are common and often occupy almost the entire dimension of the grains, leaving small room for thin, non-zoned rims. Broad zoning and convolute structures are also found within a number of weak CL-brightness crystals without a clear inner core-rim subdivision. Contacts between cores and rims vary from sharp to irregular, with cores being in many cases brighter than rims, which display weak to no CL response (Fig. 5.7). In addition, cores often display internal fractures that do not propagate into rims, which display in some cases metamictic patches characterized by small amounts of Al and Ca, as indicated by EDS analyses.

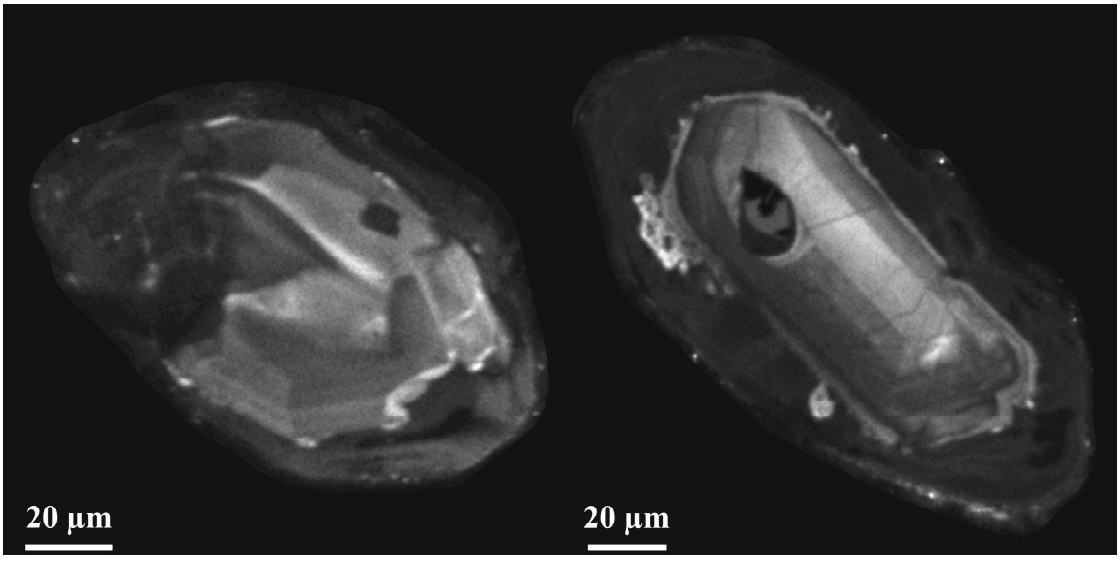

Fig. 5.7. Examples of internal textures of zircon grains from sample AUFC-19-1 (paragneiss) as revealed by cathodoluminescence imaging.

In all of the samples, a moderate fraction of the analyzed crystals displays a strongly discordant behavior caused by Pb loss. $^{207}Pb/^{206}Pb$ age spectra of the studied samples

[2] Disponível em formato digital no endereço https://www.dropbox.com/s/ppht9ebw382dsjg/AppendixII.pdf?dl=0

Table 5.2. MC-LA-ICPMS U-Pb zircon data of Ticunzal Formation samples. Common lead corrections were applied in the calculation of isotope ratios and ages by using measured ^{204}Pb. All errors are reported on a 2σ basis. **P**: paragneiss; **S**: schist; $\mathbf{f^{206}}$: fraction of common ^{206}Pb; **c**: core; **r**: rim.

Spot	Th/U	f^{206} (%)	$^{206}Pb/^{204}Pb$	Ratio $^{207}Pb/^{206}Pb$	error (%)	Ratio $^{207}Pb/^{235}U$	error (%)	Ratio $^{206}Pb/^{238}U$	error (%)	error corr. (ρ)	Age $^{207}Pb/^{206}Pb$	error (Ma)	Age $^{207}Pb/^{235}U$	error (Ma)	Age $^{206}Pb/^{238}U$	error (Ma)	Concordance (%)
Sample AUFC-19-1 (P) (13° 17' 54.5" S 46° 58' 22.2" W)																	
ZR1	0.40	0.16	9275	0.1448	1.55	8.5855	2.37	0.4300	1.79	0.76	2286	26	2295	21	2306	35	100.9
ZR2	0.40	0.26	5684	0.1370	0.82	7.5690	1.36	0.4006	1.09	0.80	2190	14	2181	12	2172	20	99.2
ZR3	0.64	1.04	1404	0.1370	1.39	7.8160	2.18	0.4137	1.66	0.77	2190	24	2210	19	2232	32	101.9
ZR4	0.47	1.35	1093	0.1390	1.34	7.6230	1.75	0.3979	1.10	0.63	2214	23	2188	16	2159	20	97.5
ZR5	0.37	0.25	5994	0.1390	1.13	7.5261	1.89	0.3926	1.51	0.80	2215	19	2176	17	2135	27	96.4
ZR6	0.37	0.94	1553	0.1460	1.32	8.5367	2.41	0.4240	2.00	0.83	2300	22	2290	22	2278	39	99.1
ZR7	0.11	0.43	3318	0.1637	2.58	10.4235	3.64	0.4617	2.56	0.70	2494	43	2473	33	2447	52	98.1
ZR8	0.15	0.00	478886	0.1654	0.65	11.1197	1.39	0.4876	1.23	0.88	2512	11	2533	13	2560	26	101.9
ZR9	0.53	0.39	3827	0.1392	2.29	7.6751	3.69	0.4000	2.89	0.78	2217	39	2194	33	2169	53	97.8
ZR10	0.77	1.89	759	0.1547	1.25	9.3883	5.20	0.4401	4.96	0.97	2399	21	2377	47	2351	99	98.0
ZR11	0.51	0.07	20680	0.1412	0.86	8.0516	1.63	0.4136	1.38	0.85	2242	15	2237	15	2231	26	99.5
ZR12	0.38	0.11	13409	0.1392	0.77	8.1351	2.27	0.4239	2.13	0.94	2217	13	2246	20	2278	41	102.7
ZR13	0.45	1.15	1291	0.1380	1.45	7.5104	2.01	0.3947	1.38	0.69	2202	25	2174	18	2145	25	97.4
ZR14	0.27	0.28	5294	0.1396	1.15	7.8642	1.66	0.4085	1.20	0.72	2222	20	2216	15	2208	22	99.4
ZR15	0.35	0.13	11313	0.1378	0.99	7.4262	1.53	0.3907	1.17	0.76	2200	17	2164	14	2126	21	96.6
ZR16	0.16	0.82	1741	0.1489	0.87	9.1203	4.65	0.4441	4.53	0.98	2334	15	2350	42	2369	90	101.5
ZR17	0.24	0.70	2053	0.1523	1.53	9.3350	2.74	0.4445	2.25	0.83	2372	26	2371	25	2371	45	99.9
ZR18	0.49	0.23	6376	0.1419	1.54	8.0356	2.19	0.4106	1.55	0.71	2251	26	2235	20	2218	29	98.5
ZR19	0.38	0.20	7488	0.1378	1.24	7.7686	2.13	0.4089	1.73	0.81	2200	21	2205	19	2210	32	100.5
ZR20	0.37	0.50	2852	0.1458	0.96	8.9972	1.79	0.4475	1.50	0.84	2297	16	2338	16	2384	30	103.8
ZR21	0.46	0.49	2971	0.1370	1.36	7.7119	2.18	0.4084	1.69	0.78	2189	24	2198	19	2207	32	100.8
ZR22	0.40	0.01	226295	0.1382	0.81	7.4995	2.16	0.3935	2.00	0.93	2205	14	2173	19	2139	36	97.0
ZR23	0.44	0.33	4509	0.1417	1.08	7.8044	2.02	0.3993	1.70	0.85	2249	18	2209	18	2166	31	96.3
ZR24	0.48	0.09	17372	0.1370	2.14	7.6219	2.70	0.4035	1.64	0.61	2189	37	2187	24	2185	30	99.8
ZR25	0.81	0.02	67565	0.1520	1.21	9.3686	2.11	0.4469	1.73	0.82	2369	21	2375	19	2382	34	100.5
ZR26	0.49	1.09	1349	0.1453	1.23	8.0924	1.95	0.4040	1.50	0.77	2291	21	2241	18	2187	28	95.5
ZR27	0.42	0.16	8945	0.1377	0.91	7.7210	1.91	0.4066	1.68	0.88	2199	16	2199	17	2199	31	100.0
ZR28	0.38	1.16	1285	0.1361	1.28	7.1892	1.72	0.3830	1.13	0.66	2179	22	2135	15	2090	20	96.0
ZR29	0.46	0.00	393672	0.1387	0.77	7.6839	1.39	0.4017	1.15	0.83	2212	13	2195	12	2177	21	98.4
ZR30	0.42	0.64	2289	0.1426	1.91	8.1510	2.98	0.4145	2.27	0.77	2259	33	2248	27	2235	43	98.9
ZR31	0.59	0.21	6718	0.1555	0.97	9.4067	2.27	0.4387	2.05	0.90	2408	16	2378	21	2345	40	97.4
ZR32	0.54	0.33	4464	0.1407	0.82	7.9661	1.36	0.4105	1.08	0.80	2236	14	2227	12	2217	20	99.1
ZR33	0.35	0.62	2416	0.1398	0.66	7.5232	1.37	0.3902	1.19	0.87	2225	11	2176	12	2124	22	95.4
ZR34	0.51	0.28	5197	0.1400	0.80	7.9289	1.96	0.4106	1.79	0.91	2228	14	2223	18	2218	34	99.6
ZR35	0.54	1.28	1154	0.1345	1.01	7.2839	1.53	0.3929	1.13	0.75	2157	17	2147	14	2136	21	99.0
ZR36	0.34	0.24	6227	0.1414	0.99	7.6526	1.61	0.3926	1.26	0.79	2244	17	2191	14	2135	23	95.1
ZR37	0.34	0.26	5751	0.1397	0.86	7.6302	5.61	0.3961	5.53	0.99	2224	15	2188	49	2151	101	96.7
ZR38	0.28	0.22	6467	0.1573	0.88	9.6368	1.71	0.4442	1.46	0.86	2427	15	2401	16	2370	29	97.6

Table 5.2. (Continued).

Spot	Th/U	f^{206} (%)	$^{206}Pb/^{204}Pb$	Ratio $^{207}Pb/^{206}Pb$	error (%)	Ratio $^{207}Pb/^{235}U$	error (%)	Ratio $^{206}Pb/^{238}U$	error (%)	error corr. (ρ)	Age $^{207}Pb/^{206}Pb$	error (Ma)	Age $^{207}Pb/^{235}U$	error (Ma)	Age $^{206}Pb/^{238}U$	error (Ma)	Concordance (%)
ZR39	0.44	1.94	739	0.1486	0.94	8.9675	2.23	0.4377	1.98	0.90	2330	16	2335	20	2340	39	100.4
ZR40	0.18	0.89	1632	0.1537	0.91	9.0205	1.69	0.4258	1.42	0.84	2387	15	2340	15	2287	27	95.8
ZR41	0.47	0.40	3669	0.1370	1.00	7.4863	1.46	0.3962	1.07	0.73	2190	17	2171	13	2152	20	98.3
ZR42	0.41	0.02	59654	0.1402	1.38	7.9999	2.01	0.4139	1.46	0.73	2229	24	2231	18	2233	28	100.2
ZR43	0.62	0.84	1702	0.1608	1.50	10.1052	2.47	0.4557	1.95	0.79	2464	25	2444	23	2420	40	98.2
ZR44	0.40	0.49	3059	0.1380	0.90	7.3548	1.48	0.3864	1.17	0.79	2203	16	2155	13	2106	21	95.6
ZR45	0.43	0.01	171767	0.1380	1.11	7.5802	2.69	0.3985	2.45	0.91	2202	19	2183	24	2162	45	98.2
ZR46	0.68	0.47	3087	0.1383	1.10	7.9340	2.42	0.4161	2.15	0.89	2206	19	2224	22	2243	41	101.7
ZR47	0.35	0.01	246470	0.1383	0.83	7.6227	1.58	0.3998	1.34	0.85	2206	14	2188	14	2168	25	98.3
ZR48	0.55	0.00	1362512	0.1417	0.85	8.1302	1.66	0.4160	1.43	0.86	2249	15	2246	15	2242	27	99.7
ZR49	0.57	0.39	3758	0.1412	1.01	8.0740	2.12	0.4149	1.86	0.88	2241	17	2239	19	2237	35	99.8
ZR50	0.25	1.60	925	0.1347	1.97	7.2287	3.54	0.3892	2.90	0.83	2160	34	2140	31	2119	53	98.1
ZR51	0.97	0.05	30327	0.1544	0.78	9.4255	1.37	0.4427	1.13	0.82	2395	13	2380	13	2363	22	98.6
ZR52	0.56	0.07	22465	0.1395	0.74	7.8821	1.46	0.4097	1.26	0.86	2221	13	2218	13	2214	24	99.7
ZR53c	0.21	0.62	2383	0.1438	1.58	8.1261	2.51	0.4100	1.94	0.78	2273	27	2245	22	2215	36	97.4
ZR53r	0.12	0.24	5998	0.1447	0.98	8.4022	1.73	0.4213	1.41	0.82	2284	17	2275	16	2266	27	99.2
ZR54	0.48	1.43	1023	0.1390	1.49	7.9312	2.38	0.4139	1.82	0.77	2214	26	2223	21	2233	35	100.8
ZR55	0.29	0.32	4589	0.1396	1.23	7.8378	2.21	0.4072	1.83	0.83	2222	21	2213	20	2202	34	99.1
ZR56	0.41	0.05	30882	0.1343	1.28	7.2768	2.06	0.3930	1.61	0.78	2155	22	2146	18	2137	29	99.2
ZR57	0.29	0.01	166311	0.1379	1.22	7.3130	2.00	0.3847	1.59	0.79	2201	21	2150	18	2098	28	95.3
ZR58	0.87	0.96	1494	0.1518	0.88	9.3218	1.75	0.4452	1.49	0.86	2367	15	2370	16	2374	30	100.3
Sample MALEG-7A (P) (13° 17' 54.5" S 46° 58' 21.2" W)																	
ZR1	0.29	0.10	13606	0.1647	2.03	10.6920	3.57	0.4709	2.93	0.82	2504	34	2497	33	2488	60	99.3
ZR2	0.04	0.03	51462	0.1373	1.41	7.7012	3.17	0.4069	2.85	0.90	2193	24	2197	28	2201	53	100.4
ZR3	0.06	0.27	5399	0.1354	1.39	7.5375	2.53	0.4038	2.11	0.84	2169	24	2177	22	2186	39	100.8
ZR4	0.09	0.05	28938	0.1533	1.49	9.7913	2.63	0.4632	2.16	0.82	2383	25	2415	24	2454	44	103.0
ZR5	0.24	0.06	25708	0.1386	1.66	7.3998	3.01	0.3872	2.50	0.83	2210	29	2161	27	2110	45	95.5
ZR6	0.11	0.28	2658	0.1350	1.49	7.6853	2.60	0.4128	2.12	0.82	2164	26	2195	23	2228	40	102.9
ZR7	0.32	0.01	109561	0.1373	1.36	7.5954	2.40	0.4011	1.98	0.83	2194	23	2184	21	2174	37	99.1
ZR8	0.32	0.09	15576	0.1479	1.68	8.4176	3.15	0.4127	2.67	0.85	2322	29	2277	28	2227	50	95.9
ZR9	0.17	0.06	24769	0.1574	1.55	9.5066	2.98	0.4381	2.55	0.85	2428	26	2388	27	2342	50	96.5
ZR10	0.18	0.03	52148	0.1564	1.67	9.6889	3.22	0.4492	2.75	0.86	2417	28	2406	29	2392	55	98.9
ZR11	0.19	0.03	51760	0.1419	1.34	8.1611	3.11	0.4171	2.81	0.90	2251	23	2249	28	2247	53	99.8
ZR12	0.16	0.01	184162	0.1381	1.23	8.2023	3.55	0.4309	3.34	0.94	2203	21	2254	32	2310	64	104.8
ZR13	0.37	0.01	248274	0.1571	1.31	10.0589	3.41	0.4645	3.14	0.92	2424	22	2440	31	2459	64	101.5
ZR14	0.28	0.04	34737	0.1442	1.43	8.0899	4.18	0.4070	3.93	0.94	2278	24	2241	37	2201	73	96.6
ZR15	0.46	0.04	37971	0.1578	1.94	9.8314	5.65	0.4520	5.31	0.94	2432	33	2419	51	2404	106	98.9
ZR16	0.16	0.03	51960	0.1376	1.49	7.8802	4.12	0.4154	3.84	0.93	2197	26	2217	36	2240	72	102.0
ZR17	0.23	0.31	4852	0.1427	1.98	7.8365	4.77	0.3984	4.33	0.91	2260	34	2212	42	2162	79	95.6
ZR18	0.23	0.15	9713	0.1419	1.92	7.7357	3.90	0.3953	3.39	0.87	2251	33	2201	34	2147	62	95.4

Table 5.2. (Continued).

Spot	Th/U	f^{206} (%)	$^{206}Pb/^{204}Pb$	Ratio $^{207}Pb/^{206}Pb$	error (%)	Ratio $^{207}Pb/^{235}U$	error (%)	Ratio $^{206}Pb/^{238}U$	error (%)	error corr. (ρ)	Age $^{207}Pb/^{206}Pb$	error (Ma)	Age $^{207}Pb/^{235}U$	error (Ma)	Age $^{206}Pb/^{238}U$	error (Ma)	Concordance (%)
ZR19	0.22	0.07	21456	0.1390	1.40	7.8768	3.53	0.4111	3.23	0.92	2214	24	2217	31	2220	61	100.2
ZR20	0.29	0.02	263604	0.1379	1.56	8.0890	3.32	0.4254	2.93	0.88	2201	27	2241	30	2285	56	103.8
ZR21	0.35	0.15	9700	0.1381	1.69	7.9283	3.89	0.4164	3.50	0.90	2203	29	2223	34	2244	66	101.9
ZR22	0.28	0.16	8995	0.1456	1.61	8.2847	2.47	0.4127	1.88	0.76	2295	27	2263	22	2227	35	97.1
ZR23	0.15	0.05	27618	0.1362	1.27	7.6006	2.53	0.4048	2.18	0.86	2179	22	2185	22	2191	40	100.6
ZR24	0.17	0.06	22954	0.1383	1.73	7.8042	3.63	0.4092	3.18	0.88	2206	30	2209	32	2211	59	100.2
ZR25	0.09	0.03	41890	0.1402	1.29	8.4551	2.81	0.4375	2.49	0.89	2229	22	2281	25	2339	49	104.9
ZR26	0.28	0.05	20067	0.1422	1.44	8.6513	2.73	0.4414	2.32	0.85	2254	25	2302	25	2357	46	104.6
ZR27	0.28	0.02	67306	0.1540	1.55	9.7492	2.72	0.4590	2.24	0.82	2391	26	2411	25	2435	45	101.8
ZR28	0.20	0.05	31928	0.1423	1.65	8.0344	2.90	0.4095	2.38	0.82	2255	28	2235	26	2213	44	98.1
ZR29	0.24	0.03	45521	0.1396	1.38	7.7885	3.12	0.4046	2.80	0.90	2223	24	2207	28	2190	52	98.5
ZR30	0.17	0.02	55435	0.1371	1.46	7.6136	4.08	0.4029	3.81	0.93	2190	25	2186	36	2182	70	99.6
ZR31	0.90	0.03	45421	0.1594	1.63	9.8225	4.80	0.4469	4.51	0.94	2449	27	2418	43	2381	89	97.2
ZR32	0.17	0.11	13791	0.1372	2.25	7.3161	4.62	0.3866	4.03	0.87	2193	39	2151	40	2107	72	96.1
Sample CAV-1A (P) (13° 49' 41.0" S 47° 34' 51.7" W)																	
ZR1	0.17	0.02	83710	0.1372	0.88	7.7174	2.43	0.4079	2.27	0.93	2192	15	2199	22	2205	42	100.6
ZR2	0.09	0.05	30437	0.1574	1.39	9.5718	2.35	0.4411	1.89	0.81	2428	23	2394	21	2355	37	97.0
ZR3	0.04	0.02	65324	0.1795	1.12	12.7166	2.52	0.5139	2.26	0.90	2648	18	2659	23	2673	49	100.9
ZR4	0.01	0.03	52534	0.1415	1.17	8.1327	2.65	0.4168	2.38	0.90	2246	20	2246	24	2246	45	100.0
ZR5	0.21	0.02	67833	0.1343	1.27	7.4327	2.51	0.4014	2.16	0.86	2155	22	2165	22	2176	40	101.0
ZR6	0.08	0.01	70795	0.1628	1.54	11.0711	3.20	0.4932	2.80	0.88	2485	26	2529	29	2585	59	104.0
ZR7	0.19	0.02	64505	0.1370	1.60	7.8140	2.41	0.4136	1.80	0.75	2190	28	2210	21	2231	34	101.9
ZR8	0.12	0.02	55531	0.1367	1.72	7.6174	2.32	0.4041	1.56	0.67	2186	30	2187	21	2188	29	100.1
ZR9	0.15	0.04	35910	0.1384	1.44	7.8879	2.15	0.4132	1.60	0.74	2208	25	2218	19	2230	30	101.0
ZR10	0.12	0.01	97578	0.1598	1.30	10.5116	1.84	0.4769	1.31	0.71	2454	22	2481	17	2514	27	102.4
ZR11	0.23	0.03	46132	0.1361	1.02	7.9672	1.85	0.4247	1.55	0.84	2178	18	2227	17	2282	30	104.8
ZR12	0.17	0.03	54032	0.1372	1.08	7.6141	2.61	0.4025	2.38	0.91	2192	19	2187	23	2181	44	99.5
ZR13	0.20	0.04	37954	0.1384	0.92	7.5448	1.90	0.3953	1.67	0.88	2208	16	2178	17	2147	30	97.3
ZR14	0.24	0.01	124989	0.1862	0.91	12.7857	1.84	0.4981	1.60	0.87	2708	15	2664	17	2606	34	96.2
ZR15	0.20	0.02	80150	0.1358	1.10	7.5502	2.35	0.4032	2.08	0.88	2174	19	2179	21	2184	38	100.4
ZR16	0.18	0.09	15969	0.1619	1.20	10.4194	1.79	0.4669	1.32	0.74	2475	20	2473	16	2470	27	99.8
ZR17	0.18	0.03	49453	0.1362	1.32	7.6897	2.33	0.4096	1.91	0.82	2179	23	2195	21	2213	36	101.6
ZR18	0.13	0.02	84633	0.1645	1.15	10.7643	1.74	0.4746	1.30	0.75	2502	19	2503	16	2504	27	100.1
Sample XUPE-1 (S) (13° 14' 23.8" S 46° 51' 43.9" W)																	
ZR1	0.16	0.04	33774	0.1351	1.48	7.5135	2.68	0.4032	2.23	0.83	2166	26	2175	24	2184	41	100.8
ZR2	0.19	0.08	15162	0.1365	1.38	7.6683	2.70	0.4075	2.32	0.86	2183	24	2193	24	2203	43	100.9
ZR3	0.24	0.01	133261	0.1354	1.22	7.4736	3.51	0.4003	3.29	0.94	2169	21	2170	31	2171	60	100.1
ZR4	0.35	0.01	123849	0.1395	1.10	7.9184	1.91	0.4118	1.56	0.82	2220	19	2222	17	2223	29	100.1
ZR5	0.15	0.02	78390	0.1346	1.43	7.3846	2.23	0.3979	1.71	0.77	2159	25	2159	20	2159	31	100.0
ZR6	0.30	0.04	61569	0.1379	1.40	7.7393	4.49	0.4071	4.26	0.95	2201	24	2201	40	2202	79	100.0

Table 5.2. (Continued).

Spot	Th/U	f^{206} (%)	$^{206}Pb/^{204}Pb$	Ratio $^{207}Pb/^{206}Pb$	error (%)	Ratio $^{207}Pb/^{235}U$	error (%)	Ratio $^{206}Pb/^{238}U$	error (%)	error corr. (ρ)	Age $^{207}Pb/^{206}Pb$	error (Ma)	Age $^{207}Pb/^{235}U$	error (Ma)	Age $^{206}Pb/^{238}U$	error (Ma)	Concordance (%)
ZR7	0.17	0.03	50613	0.1901	1.01	13.9285	2.12	0.5313	1.87	0.88	2743	16	2745	20	2747	42	100.1
ZR8	0.17	0.03	51218	0.1359	0.98	7.5334	1.88	0.4021	1.60	0.85	2175	17	2177	17	2179	30	100.2
ZR9	0.15	0.07	21054	0.1395	1.21	7.9100	3.56	0.4113	3.35	0.94	2221	21	2221	32	2221	63	100.0
ZR10	0.16	0.04	27344	0.1359	0.99	7.5936	2.02	0.4054	1.77	0.87	2175	17	2184	18	2194	33	100.9
ZR11	0.10	0.02	87491	0.1565	0.73	10.3486	1.39	0.4795	1.18	0.85	2418	12	2466	13	2525	25	104.4
ZR12	0.21	0.04	35380	0.1374	0.90	7.6422	1.76	0.4034	1.51	0.86	2194	16	2190	16	2185	28	99.6
ZR13	0.19	0.09	16960	0.1393	1.33	7.9234	4.45	0.4126	4.24	0.95	2218	23	2222	39	2227	79	100.4
ZR14	0.19	0.03	36012	0.1344	1.08	7.6860	1.78	0.4148	1.41	0.80	2156	19	2195	16	2237	27	103.8
ZR15	0.30	0.04	34650	0.1611	1.14	10.5217	2.23	0.4738	1.91	0.86	2467	19	2482	20	2500	40	101.3
ZR16	0.17	0.03	44891	0.1374	1.39	7.7696	2.40	0.4101	1.96	0.82	2195	24	2205	21	2215	37	100.9
ZR17	0.37	0.02	41075	0.1563	0.92	9.8009	2.03	0.4548	1.81	0.89	2416	16	2416	19	2417	36	100.0
ZR18	0.26	0.02	76683	0.1388	0.92	7.8838	1.90	0.4120	1.66	0.87	2212	16	2218	17	2224	31	100.5
ZR19	0.23	0.05	28843	0.1393	0.99	7.9768	3.10	0.4154	2.93	0.95	2218	17	2228	28	2239	55	100.9
ZR20	0.39	0.10	14106	0.1393	0.80	7.9244	1.65	0.4127	1.44	0.87	2218	14	2222	15	2227	27	100.4
ZR21	0.35	0.02	84309	0.1420	0.81	8.2375	1.76	0.4207	1.56	0.89	2252	14	2257	16	2264	30	100.5
ZR22	0.20	0.04	39125	0.1403	1.23	8.0770	2.24	0.4175	1.86	0.83	2231	21	2240	20	2249	35	100.8
ZR23	0.30	0.03	43770	0.1394	0.88	8.2916	1.82	0.4312	1.59	0.87	2220	15	2263	16	2311	31	104.1
ZR24	0.28	0.03	83376	0.1348	0.77	7.4149	1.36	0.3990	1.12	0.83	2161	13	2163	12	2164	21	100.1
ZR25	0.16	0.03	53301	0.1604	0.92	10.3002	2.35	0.4657	2.17	0.92	2460	15	2462	22	2464	44	100.2
ZR26	0.16	0.02	73840	0.1347	0.81	7.3752	1.44	0.3970	1.20	0.83	2160	14	2158	13	2155	22	99.8

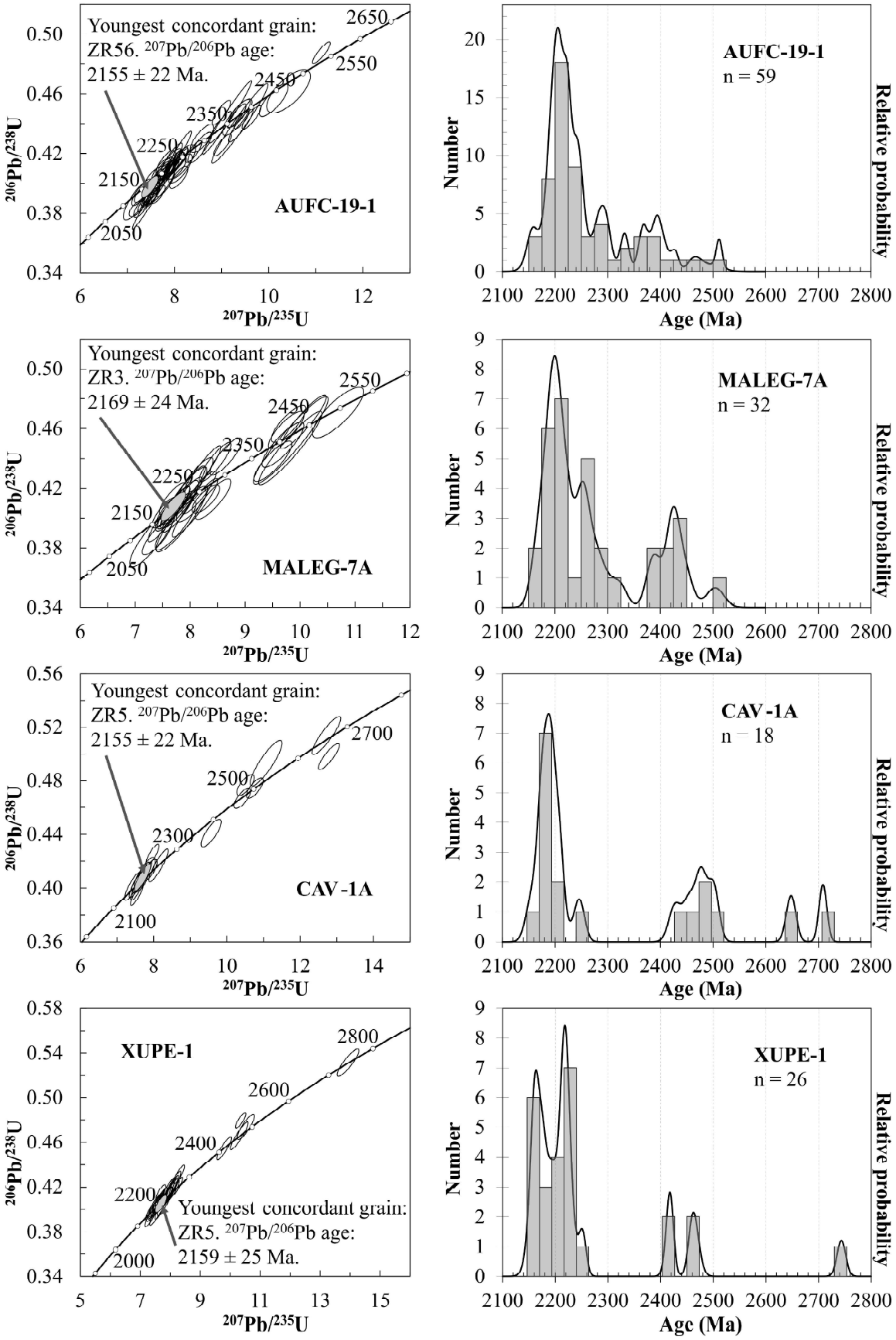

Fig. 5.8. U-Pb zircon data of analyzed samples. Only data from zircon crystals with concordances between 95 and 105% are shown. The ages shown in the histograms correspond to $^{207}Pb/^{206}Pb$ ages. Sample XUPE-1 corresponds to a schist. All ages and errors were calculated on a 2σ basis.

were obtained considering only analyses with concordances between 95 and 105% (Fig. 5.8; Table 5.2). Those spectra show a predominant age peak at 2.19-2.25 Ga followed by less prominent age populations at 2.40-2.50 Ga, 2.25-2.30 Ga and 2.15-2.19 Ga. Only samples XUPE-1 and CAV-1A yielded three zircon grains with ages between 2.65 and 2.75 Ga.

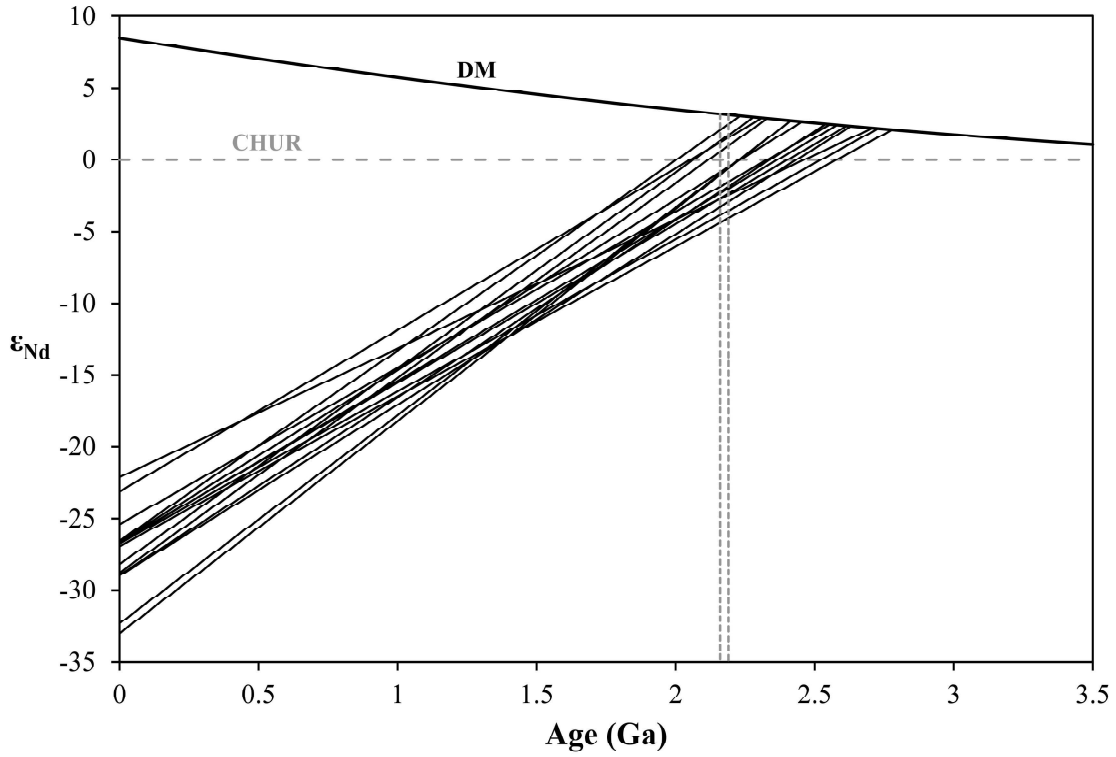

Fig. 5.9. ε_{Nd} vs. age plot of the analyzed samples. Depleted mantle (DM) curve according to model by DePaolo (1981). 2.16-2.19 Ga age interval shown for reference.

5.4.3. Sm-Nd isotope geochemistry

Results of Nd isotope analyses are shown in Table 5.3. Schists and paragneisses yielded $^{143}Nd/^{144}Nd$ and $^{147}Sm/^{144}Nd$ ratios within intervals 0.510945-0.511503 and 0.0815-0.1268, respectively, leading to T_{DM} ages varying between 2.23 and 2.88 Ga (Fig. 5.9). Given the reference age interval between 2.19 and 2.16 Ga (see significance of this interval in the discussion below), ε_{NdT} of the Ticunzal Formation display both positive (+0.54 to +2.48) and negative (-0.54 to -4.46) values, with the former obtained from samples AUFC-12-2, AUFC-13-1, AUFC-13-2 (schists) and AUFC-39-1 (paragneiss), which also yielded the youngest T_{DM} ages between 2.23 and 2.33 Ga.

Table 5.3. Sm-Nd isotope data. Errors in the last two digits of $^{143}Nd/^{144}Nd$ ratios are 2σ. Present-day $^{143}Nd/^{144}Nd_{CHUR}$ and $^{147}Sm/^{144}Nd_{CHUR}$ values used in calculations were 0.512638 and 0.1966, respectively (Jacobsen and Wasserburg, 1980; 1984). T_{DM} ages according to the depleted mantle model of DePaolo (1981). **S**: Schist; **P**: Paragneiss.

Sample	Rock Type	Location		Sm (ppm)	Nd (ppm)	$^{143}Nd/^{144}Nd$	$^{147}Sm/^{144}Nd$	T_{DM} (Ga)	ε_{Nd} (T ~ 2.19 / 2.16 Ga)
		Lat. (S)	Long. (W)						
AUFC11-3	S	13° 22' 58.6"	46° 55' 41.9"	12.14	65.58	0.511336	0.1119	2.56	-1.57 / -1.90
AUFC12-2	S	13° 16' 12.6"	46° 53' 47.3"	2.53	16.83	0.511163	0.091	2.33	+0.95 / +0.54
AUFC13-1	S	13° 14' 22.1"	46° 50' 58.0"	6.84	37.91	0.511452	0.109	2.31	+1.52 / +1.18
AUFC13-2	S	13° 14' 22.1"	46° 50' 58.0"	4.29	28.67	0.511193	0.0904	2.28	+1.71 / +1.29
AUFC19-1	P	13° 17' 54.5"	46° 58' 22.2"	6.862	41.28	0.511155	0.1005	2.54	-1.90 / -2.27
AUFC35-2	P	13° 50' 14. 7"	47° 51' 42.4"	22.52	162.47	0.510981	0.0838	2.41	-0.58 / -1.02
AUFC39-1	P	13° 24' 31.7"	47° 05' 37.8"	14.33	92.70	0.511277	0.0935	2.23	+2.48 / +2.07
XUPE-1	S	13° 14' 23.8"	46° 51' 43.9"	6.74	35.29	0.511257	0.1155	2.78	-4.14 / -4.46
MALEG-3	P	13° 16' 9.5"	46° 52' 24.5"	4.70	27.29	0.511276	0.1041	2.45	-0.54 / -0.90
MALEG-7A	P	13° 17' 54.5"	46° 58' 21.2"	5.48	31.82	0.511152	0.1041	2.88	-2.97 / -3.34
CAV-1A	P	13° 49' 41.0"	47° 34' 51.7"	6.85	37.47	0.511273	0.1105	2.62	-2.41 / -2.75
CAV-5	P	13° 46' 47.1"	47° 37' 31.3"	4.65	24.74	0.511267	0.1143	2.73	-3.60 / -3.93
CAV-6A	P	13° 44' 2.1"	47° 38' 20.7"	5.20	28.81	0.511270	0.1090	2.58	-2.05 / -2.39
CAV-7	P	13° 50' 41.6"	47° 30' 55.5"	79.36	37.82	0.511503	0.1268	2.71	-2.51 / -2.78
CAV-8A	P	13° 50' 43.1"	47° 30' 50.8"	33.48	248.46	0.510945	0.0815	2.41	-0.64 / -1.09

5.4.4. Raman spectroscopy

Carbonaceous matter lamellae of three samples of carbonaceous schists of the Ticunzal Formation were analyzed using Raman spectroscopy, with complete spectrum data shown in Appendix III[3]. In general, spectra morphology is quite variable as a function of the orientation of the lamellae and the thickness and characteristics of the host mineral (either quartz or muscovite). However, a tendency towards morphologies displaying high-intensity, well-defined G peaks with subordinated, low-intensity D1 and D2 peaks was observed (Fig. 5.10). The fact that the G peak is associated to structural order within graphene layers, while D1 and D2 peaks are associated to defects in those structures (Beyssac *et al.*, 2002), means that the obtained spectra are indicative of high-crystallinity in the analyzed carbonaceous matter, allowing to refer properly to the latter

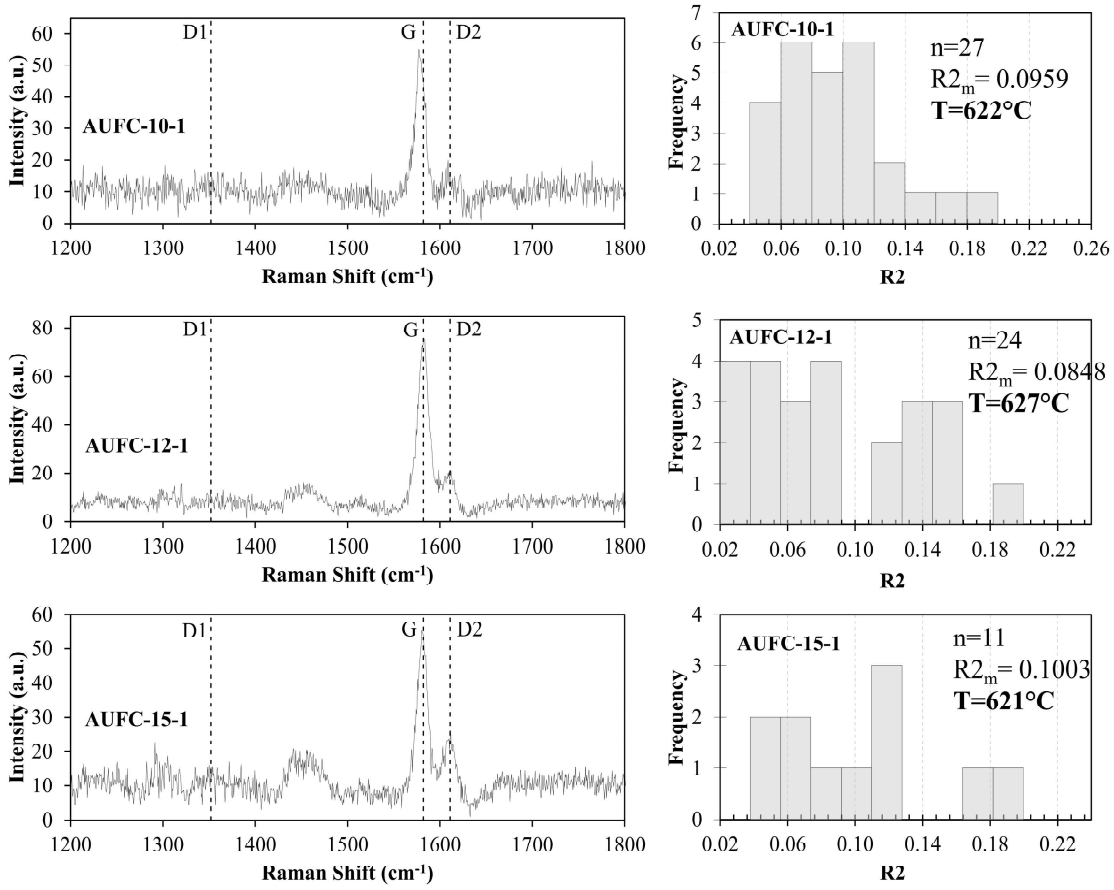

Fig. 5.10. Examples of representative graphite Raman spectra obtained from Ticunzal Formation schist samples. Positions of graphite main structural (G) and crystalline defect (D1 and D2) peaks are shown. Ranges of R2 values obtained from each sample are shown in the histograms along with their mean values and the respective temperature estimations using the methodology from Beyssac *et al.* (2002). See complete data in Appendix III.

[3] Disponível em formato digital no endereço https://www.dropbox.com/s/t5viqkxj0kr3thb/AppendixIII.xls?dl=0

as graphite. This had been already suggested by petrographic observations that revealed a strong bireflectance of the graphitic lamellae, which is known to be correlated to high degrees of crystallinity.

After data processing of all spectra, the obtained mean values of the R2 parameter for each sample were 0.0848, 0.0959 and 0.1003 (Fig. 5.10; Appendix III), which allowed estimating peak regional metamorphic temperatures of 627ºC, 622ºC and 621ºC, respectively, with aid of the equation T(°C)=-445*R2+641 (Beyssac *et al*., 2002).

5.5. DISCUSSION

5.5.1. Age and provenance

Previous estimates of the age of the Ticunzal Formation relied solely on Nd model ages, which resulted in large uncertainties as to its actual deposition age (Pimentel *et al*., 2004; Botelho *et al*., 2006a; Fuck *et al*., 2014). Zircon U-Pb data presented in this work allowed for the first time an accurate assessment of the age and likely source of sediments of the Ticunzal Formation.

The clear field evidence indicating that the Ticunzal Formation was intruded syn- to post-kinematically by peraluminous plutons of the Aurumina Suite leads to establishment of the crystallization age of the latter as the minimum age of sedimentation of the Ticunzal Formation. Based on zircon U-Pb data and field relations, Cuadros *et al*. (submitted) have shown that the earliest magmatic pulses of the Aurumina Suite probably took place between 2.15 and 2.16 Ga. The $^{207}Pb/^{206}Pb$ ages between 2.15 and 2.19 Ga obtained in this work from a group of Ticunzal Formation zircon grains could be interpreted as artifacts caused by Pb loss, as the intrusion of the Aurumina Suite must have represented an extensive thermal disturbance likely responsible for the rejuvenation of some of the zircon ages, which might have been facilitated by the presence of metamorphic fluids under amphibolite facies conditions and the metamictic character of some zircon crystals. Given the relatively close temporal proximity that exists between the intrusion of the Aurumina Suite and the youngest zircon forming event in the provenance of the Ticunzal Formation (2.19-2.25 Ga), Pb losses in the latter would appear in the $^{206}Pb/^{238}U$-$^{207}Pb/^{235}U$ diagram as a small offset of ellipses along the concordia curve, with deviations from the latter so negligible that allow preservation of the concordant character of data points, thus mimicking an apparently younger provenance. Therefore, a deposition age interval between 2.16 and 2.19 Ga is proposed here for the

sediments that gave origin to the Ticunzal Formation. It must be noted that this interval is relatively narrow and its width is comparable to the magnitude of errors in the age calculations, leaving room for future refinements achieved by higher resolution techniques.

In addition to the interval of 2.19-2.25 Ga, the U-Pb data presented above reveal two more episodes of zircon formation at 2.40- 2.50 Ga and 2.65-2.75 Ga. An additional age interval between 2.25 and 2.30 Ga can also be identified from the data, but is regarded as rather unreliable in view of its poor definition in the age spectra (Fig. 5.8).

The Almas-Conceição do Tocantins domain in the northern portion of the external zone of the Brasília Fold Belt is characterized by the presence of abundant plutonic rocks of tonalite-trondhjemite-granodiorite (TTG) affinity, with ages between 2.19 and 2.50 Ga (Fuck *et al*., 2014; Sousa *et al*., 2016). In particular, the Almas-Dianópolis terrane within this domain is characterized by tonalitic/granodioritic rocks grouped under the denominations of Ribeirão das Areias Complex, Suite 1 and Suite 2 (Costa, 1985; Cruz and Kujumjian, 1998; Cruz, 2001; Cruz *et al*., 2003). Cruz (2001) reported a sphene SHRIMP U-Pb age of 2.46 Ga for the Ribeirão das Areias Complex, and zircon SHRIMP U-Pb ages of ~2.20 Ga for suites 1 and 2. Geochemically, these three units display two distinct REE patterns, with Suite 1 being characterized by a relative enrichment of HREE and moderate negative Eu anomalies, while both the Ribeirão das Areias Complex and Suite 2 display subtle negative to positive Eu anomalies and lower HREE contents (Cruz *et al*., 2003). Geochemical data from Ticunzal Formation samples presented here point out a provenance predominantly felsic in composition, although conspicuously high Ni contents are observed in a couple of samples (Figs. 5.4c, 5.4d and 5.4e). In addition, their REE contents define two patterns, each one characterized by distinct $(La/Yb)_N$ ratios and, to some extent, LREE contents that make them very similar to the REE patterns displayed by the TTG units of the Almas-Dianópolis terrane, except for the larger negative Eu anomalies found in the low-HREE group of Ticunzal Formation paragneisses (Fig. 5.6b). Given these geochemical and geochronological similarities, it is proposed here that the Almas-Dianópolis terrane in the external zone of the Brasília Fold Belt acted as the main source of the sediments that gave origin to the Ticunzal Formation. This is consistent with the similarity that exists between the Nd model ages of the Ticunzal Formation (2.23-2.88 Ga) and those of the Ribeirão das Areias Complex and suites 1 and 2 (2.44-2.76 Ga; Cruz, 2001), as well as other related tonalitic rocks from the Almas-Conceição do

Tocantins domain (2.33-3.04 Ga; Fuck *et al*., 2014; Sousa *et al*., 2016). Sediment derivation from the Almas-Dianópolis terrane is also consistent with the tonalitic-granodioritic mineralogical composition displayed by some paragneiss samples of the Ticunzal Formation and the low degree of sediment reworking suggested by low Zr/Sc ratios that could be interpreted as a proximal character of the provenance (Table 5.1; Fig. 5.4b). A small number of zircon analyses yielding SHRIMP ages between 2.17 and 2.19 Ga were also obtained by Cruz (2001) from suites 1 and 2, which were interpreted by this author as a likely result from isotopic disturbances in zircon crystals caused by late magmatic fluids associated with cooling of the tonalitic-granodioritic rocks of these suites. Hence, it is also possible that the zircon crystals with ages between 2.17 and 2.19 Ga obtained from Ticunzal Formation samples in this work correspond to the rejuvenated zircon populations found in suites 1 and 2, which would not only reinforce the idea of the Almas-Dianópolis terrane as a provenance for the Ticunzal Formation, but it would also support the proposal of a maximum deposition age of 2.19 Ga for the Ticunzal Formation presented in this work, as ages between 2.17 and 2.19 Ga would lack any regional significance.

5.5.2. Constraints on tectonic seting, metamorphism and basin characteristics

Determining the tectonic characteristics of the basin in which the Ticunzal Formation was deposited represents a major challenge given the intense deformation and metamorphism that the formation has undergone, as well as the lack of outcrop continuity that, altogether, prevent the proper assessment of structural, sedimentological and stratigraphic features needed to such endeavor. On the other hand, geochemical approaches are also useful in attempting to understand the tectonic history of sedimentary sequences (McLennan *et al*., 1993), and such an approach is therefore adopted in this work. At first glance, major element geochemical data seem to suggest that the Ticunzal Formation represents a sequence that was probably deposited in a passive margin setting, based mainly on the rather high K_2O/Na_2O ratios displayed by the analyzed samples. These data, however, bear a great degree of variation that allows the compositions of some samples to plot also within the fields of active continental margin and arc settings (Figs. 5.5a, 5.5b, and 5.11a). It is likely that the scattering of the K_2O/Na_2O ratios observed in the studied samples actually reflects compositional disturbances that took place during metamorphism and deformation of the Ticunzal Formation, as exemplified

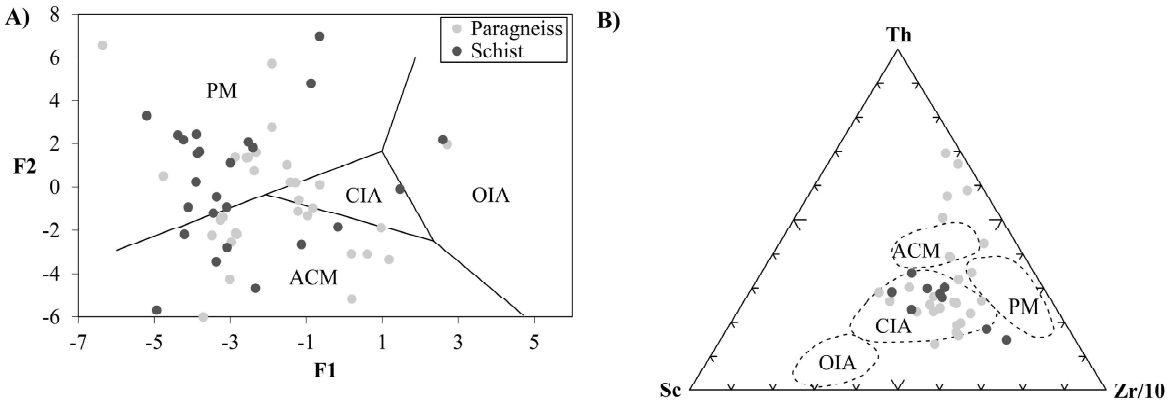

Fig. 5.11. Geochemical features of the analyzed samples. **a**: discriminant function-based tectonic classification diagram of Bhatia (1983). **b**: Th-Sc-Zr/10 tectonic discrimination diagram of Bhatia and Crook (1986). PM: passive margin; ACM: active continental margin; CIA: continental island arc; OIA: oceanic island arc.

by the muscovite-rich mineral assemblages found in some mylonitic paragneisses and schists. Furthermore, high K_2O/Na_2O sediments would not be expected to be derived from a dominantly tonalitic/granodioritic provenance such as the Almas-Dianópolis terrane, as stated above, which reinforces the idea of possible geochemical changes in the major element compositions of the Ticunzal Formation rocks. When trace element geochemical data are also taken into account, it becomes clear that most of the compositions tend to plot within the continental island arc field of Bhatia and Crook (1986), with some samples going towards the active continental margin field, and even further in the direction of the Th vertex (Fig. 5.11b). The anomalous behavior displayed by the latter group of samples can be understood in terms of their mineralogical composition, as these samples represent the same monazite-rich paragneisses that also displayed an anomalous trend in Fig. 5.4b. Thus, it is proposed here that the sediments that gave origin to the Ticunzal Formation were deposited in a peri-cratonic basin related to a continental arc setting. Such context is consistent with the subduction-related setting that would have prevailed in the region prior to the deposition of the Ticunzal Formation and in which the ~2.20 Ga calc-alkaline tonalitic/granodioritic rocks of the Almas-Dianópolis terrane were formed (Cruz, 2001; Cruz *et al*., 2003), as well as with the arc-related setting in which the Aurumina Suite was intruded between 2.11 and 2.16 Ga (Cuadros *et al*., submitted). The existence of these subduction-related regimes is thus the main reason to discard the possibility of a passive margin setting suggested by major element data of the Ticunzal Formation samples. Current available data, however, are insufficient to specify whether a continental arc was developed at the margin of the São Francisco Craton itself, or it actually corresponded to a fringing arc off the western margin of the craton.

Metamorphism of the Ticunzal Formation reached upper-amphibolite facies as suggested by the peak metamorphic temperatures between 620 and 630ºC obtained from Raman spectroscopy in graphite. The establishment of the thermal regime under which such metamorphism took place might have been facilitated by the intrusion of the voluminous magmas associated with the Aurumina Suite and the elevated geothermal gradients associated with the asthenospheric rise that is thought to have triggered the mafic-granitic magmatism of the Aurumina Suite and related plutons (Cuadros *et al*., submitted). In fact, it is suggested here that the maximum age of the Ticunzal Formation metamorphic peak would coincide with that of the intrusion of the earliest magmatic pulses of the Aurumina Suite (~ 2.16 Ga: Cuadros *et al*., submitted), given the syntectonic character of these plutons in the Ticunzal Formation and the nearly concordant $^{207}Pb/^{206}Pb$ ages between 2.15 and 2.16 Ga obtained from some zircon crystals of the Ticunzal Formation that are interpreted as a result of isotopic rejuvenation caused by the Aurumina Suite magmatism. The Ticunzal Formation metamorphism would predate the well-documented, granulite-facies metamorphic events recorded on the eastern portions of the São Francisco Craton at 2.0-2.08 Ga (Ledru *et al*., 1994; Barbosa and Sabaté, 2004; Barbosa and Barbosa, 2017), which suggests that Paleoproterozoic tectonic reworking of the lithosphere started earlier at the western margin of the craton. The Ticunzal Formation could be an analog of the rocks belonging to the metamorphic core complexes that exist in the cordilleran hinterland of North America and to which nearly coeval metaluminous and peraluminous magmas are associated (Armstrong, 1982; Coney and Harms, 1984; Yonkee and Weil, 2015). However, more detailed structural and thermal history reconstructions of the Ticunzal Formation are needed in order to verify whether such parallel can be actually established or not.

As inferred from the data presented above, one of the most remarkable features of the basin where the Ticunzal Formation was deposited would be the short duration of its sedimentation. Rather than an intrinsic characteristic of the sedimentary processes that generated the formation, such short-lived sedimentation could be envisioned as a natural consequence of the tectonic evolution of the basin, as the latter would have seen its sedimentation arrested by the crustal destabilization that ultimately led to the onset of the Aurumina Suite magmatism and coeval amphibolite-facies metamorphism. This early destabilization, coupled with the restricted character of the basin (*i.e.*, a silled basin) that is suggested by the limited geographical distribution of the Ticunzal Formation, are

compatible with the continental arc-related setting inferred above. On a global scale, the occurrence of organic matter-rich sedimentary rocks during the 2.06-2.20 Ga lapse has been shown to be extremely restricted, which constitutes the paradox related to the well-documented Lomagundi-Jatuli isotopic event, when sedimentary carbonates deposited around the world underwent a positive excursion in their $\delta^{13}C$ signatures (Melezhik and Fallick, 1996; Melezhik et al., 1999; 2013). Several models attempting to explain this paradox have been put forward (Melezhik and Fallick, 1996; 1997, Melezhik et al., 2005), although none of them turns out to be entirely satisfactory. One of the questions that remains, is whether the scarcity of organic matter-rich rocks representing the material that would have been needed to balance the positive $\delta^{13}C$ excursion of carbonates formed during the 2.06-2.20 Ga lapse is due to poor preservation in the geological record (*i.e.*, loss by erosion or subduction), or actual lack of suitable conditions for major deposition of organic matter during sedimentation. Silled basins are settings where deposition of organic matter-rich sediments is particularly favored (Littke, 1993), and thus, it is likely that the restricted nature of the Ticunzal Formation basin was the main factor that led to its conspicuous accumulation of organic matter. The latter feature might have been, in turn, an important factor controlling the formation of uranium-ores within the Ticunzal Formation, as solid organic matter plays a main role in decreasing uranium mobility through complexation and precipitation (Spirakis, 1996; Cumberland *et al.*, 2016). The preservation of the Ticunzal Formation rocks could be related to the fact that the crust in this sector of the São Francisco Craton was rapidly stabilized after the ~2.16 Ga tectonomagmatic events, as required by the late onset of the Araí Rift and associated sedimentation at ~1.78 Ga, which was related to the Espinhaço rifting event (Pimentel *et al.*, 1991; Chemale Jr. *et al.*, 2012; Santos *et al.*, 2013).

The discussion above highlights the importance of characterizing the Ticunzal Formation, as it constitutes one of the rare examples of organic matter-rich rocks formed during the Lomagundi-Jatuli isotopic event, and future research of this unit could contribute to the understanding of the processes that led to its establishment.

5.6. CONCLUSIONS

The following conclusions can be drawn from the data presented in this work:

- The sediments that gave origin to the Ticunzal Formation were mainly derived from the tonalitic/granodioritic rocks of the Almas-Dianópolis terrane in the northernmost portion of the external zone of the Brasília Fold Belt, with possible minor contributions from mafic-ultramafic units of the Riachão do Ouro Group belonging to the same domain.

- The sedimentation of the Ticunzal Formation is constrained to have taken place between 2.16 and 2.19 Ga based on U-Pb zircon geochronology and field relations with the intrusive Aurumina Suite. Such short-lived sedimentation would have been the result of an early tectonic destabilization, which was accompanied by the Aurumina magmatism and metamorphism.

- Both petrographic and Raman spectroscopy analysis indicate that the carbonaceous matter found in schists of the Ticunzal Formation correspond to high-crystallinity material (*i.e.*, graphite). Metamorphic peak temperatures inferred from the Raman spectroscopy-based geothermometer of Beyssac *et al*. (2002) in graphite are in the range of 620 to 630ºC, consistent with metamorphism at upper-amphibolite facies.

- Trace element geochemical compositions of Ticunzal Formation samples suggest that this sequence was deposited in a continental arc-related basin in the western border of the São Francisco Craton, which is consistent with both the cordilleran hinterland and magmatic arc settings inferred in other works for the Aurumina Suite and units of the Almas-Dianópolis terrane, respectively. The restricted nature of the basin where the Ticunzal Formation was deposited would have been the main factor controlling the occurrence of high amounts of organic matter that were deposited along with the sediments.

- The presence of Rhyacian magmatic and metamorphic units represented by rocks in the Almas-Dianópolis terrane, the Aurumina Suite and the Ticunzal Formation in the external zone of the Brasília Fold Belt provide evidence for the existence of another important Paleoproterozoic mobile belt in the western margin of the São Francisco Craton, in addition to the other well-known Archean-Paleoproterozoic provinces related

to the Mineiro Belt, the Itabuna-Salvador-Curaçá belt and the Serrinha, Jequié and Gavião blocks in the southern and central-eastern portions of the craton, respectively.

5.7. ACKNOWLEDGEMENTS

This work was possible thanks to financial support from the Conselho Nacional de Desenvolvimento Científico e Tecnológico (CNPq) of Brazil under grant 156627/2012-4 to FAC, and INCTET grant to RAF. NFB, RAF and ELD acknowledge CNPq research fellowships. Special thanks are offered to Prof. Sebastião William da Silva of the Physics Institute of the University of Brasília for his guidance during the Raman spectroscopy analyses, and to Prof. Paul Stoddart of the Biotactical Engineering, Industrial Research Institute of the Swinburne University of Technology (Melbourne, Australia) who kindly provided the MATLAB®-based code for the Raman fluorescence background subtraction method of Cadusch *et al*. (2013). Insightful comments from professors Massimo Matteini and Carlos José de Souza Alvarenga, as well as assistance from the technical staff of the geochronology and petrography laboratories of the University of Brasília, are also gratefully acknowledged.

CAPÍTULO 6 - CONCLUSÕES

- Os granitos e tonalitos/granodioritos da Suíte Aurumina foram intrudidos na borda oeste do Cráton São Francisco durante o intervalo compreendido entre 2.11 e 2.16 Ga.

- Dados geoquímicos e isotópicos sugerem que a Suíte Aurumina e unidades metaluminosas/intermediárias associadas, tais como as rochas de Nova Roma, Colinas do Sul e Arraias, representam um contínuo de magmas híbridos que resultaram da reação entre rochas metassedimentares e fundidos basálticos a baixa profunidade na crosta (< 18 km).

- O componente metassedimentar da fonte que deu origem à Suíte Aurumina poderia ser relacionado à mesma fonte que gerou as rochas de 2.2-2.4 Ga no terreno Almas-Dianópolis, ou a material desconhecido mais antigo. Alternativamente, a Formação Ticunzal poderia ter jogado um papel como fonte da Suíte Aurumina, mas com rochas profundas da zona de fonte tendo características diferentes daquelas encontradas na superfície atualmente, e que correspondem às encaixantes da Suíte Aurumina.

- Existem várias semelhanças entre a região estudada neste trabalho e a faixa granítica peraluminosa do Jurássico-Paleógeno do interior cordilheirano da América do Norte, o que sugere um ambiente relacionado a arco semelhante para o magmatismo da Suíte Aurumina.

- Os sedimentos que deram origem à Formação Ticunzal foram derivados principalmente a partir das rochas tonalíticas/granodioríticas do terreno Almas-Dianópolis na porção setentrional da zona externa da Faixa Brasília, com possíveis contribuições menores de rochas máficas-ultramáficas do Grupo Riachão do Ouro no mesmo domínio.

- Segundo dados geocronológicos de U-Pb e as relações de campo com a Suíte Aurumina, a sedimentação da Formação Ticunzal teria acontecido no período compreendido entre

2.16 e 2.19 Ga. A curta duração dessa sedimentação teria sido consequência da desestabilização tectônica precoce que foi acompanhada pelo magmatismo da Suíte Aurumina e o metamorfismo.

- Análises petrográficas e de Raman indicam que a matéria carbonosa encontrada nos xistos da Formação Ticunzal correspondem a material de alta cristalinidade (*i.e.*, grafita). As temperaturas de pico metamórfico inferidas pelo geotermómetro de espectroscopia Raman em grafita proposto por Beyssac *et al*. (2002) oscilam entre 620 e 630ºC, consistente com fácies anfibolito alto.

- A composição geoquímica de elementos traço de amostras da Formação Ticunzal sugere que esta sequência foi depositada em uma bacia relacionada a arco continental na borda oeste do Cráton São Francisco, o que é consistente com o ambiente de interior cordilheirano inferido para a Suíte Aurumina, e o ambiente de arco inferido em outros trabalhos para as unidades do terreno Almas-Dianópolis. A natureza restrita da bacia onde foi depositada a Formação Ticunzal teria sido o principal fator que controlou a ocorrência de grandes quantidades de matéria orgânica que foram depositadas junto com os sedimentos.

- A presença de unidades magmáticas e metamórficas do Rhiaciano na zona externa da Faixa Brasília, representadas por rochas do terreno Almas-Dianópolis, a Suíte Aurumina e a Formação Ticunzal, fornecem evidência para a existência de outra importante faixa móvel Paleoproterozoica na borda oeste do Cráton São Francisco, que é somada às outras bem conhecidas províncias Arqueanas-Paleoproterozóicas relacionadas à Faixa Mineira, a Faixa Itabuna-Salvador-Curaçá, e os blocos Serrinha, Jequié e Gavião nas porções sul e centro-leste do Cráton.

REFERÊNCIAS BIBLIOGRÁFICAS

Alkmim, F.F., Brito-Neves, B.B., Alves, J.A.C. 1993. Arcabouço tectônico do Cráton do São Francisco - uma revisão. In: Dominguez, J.M.L., Misi, A. (Eds.). O Cráton do São Francisco. SBG-SGM-CNPq. Salvador. 45-62 p.

Alkmim, F.F., Noce, C.M. 2006. The Paleoproterozoic record of the São Francisco Craton. In: Alkmim, F.F., Noce, C.M. (Eds.). The Paleoproterozoic Record of the São Francisco Craton. IGCP 509 Field workshop, Bahia and Minas Gerais, Brazil. Field Guide & Abstracts, 114 p.

Almeida, F.F.M. 1967. Origem e evolução da plataforma brasileira. DNPM-DGM. Bulletin 241. Rio de Janeiro. 36 p.

Almeida, F.F.M. 1977. O Cráton do São Francisco. Revista Brasileira de Geociências, 7: 349-364.

Almeida, F.F.M. 1981. O Cráton do Paramirim e suas relações com o do São Francisco. In: Anais do Simpósio sobre o Cráton do São Francisco e suas faixas marginais. CPM-SBG/NBA. Salvador. 1-10 p.

Almeida, F.F.M., Hasui, Y., Brito-Neves, B.B., Fuck, R.A. 1981. Brazilian structural provinces: an introduction. Earth-Science Reviews, 17: 1-29.

Alvarenga, C.J.S., Botelho, N.F., Dardenne, M.A., Lima, O.N.B., Machado, M.A. 2007. Geologia das folhas Monte Alegre de Goiás (SD.23-V-C-III), Cavalcante (SD.23-V-C-V) e Nova Roma (SD.23-V-C-VI), Escala 1:100.000. CPRM-UnB. Sheet memoirs. 67 p.

Anderson, J.L., Rowley, M.C. 1981. Synkinematic intrusion of peraluminous and associated metaluminous granitic magmas, Whipple Mountains, California. Canadian Mineralogist, 19: 83-101.

Armstrong, R.L. 1982. Cordilleran metamorphic core complexes -from Arizona to Southern Canada. Annual Review of Earth and Planetary Sciences, 10: 129-154.

Asmerom, Y., Ikramuddin, M., Kinart, K. 1988. Geochemistry of Late Cretaceous granitoids from northeastern Washington: Implication for genesis of two-mica Cordilleran granites. Geology, 16: 431-435.

Assumpção, M., An, M., Bianchi, M., França, G.S.L., Rocha, M., Barbosa, J.R., Berrocal, J. 2004. Seismic studies of the Brasília fold belt at the western border of the São Francisco Craton, Central Brazil, using receiver function, surface-wave dispersion and teleseismic tomography. Tectonophysics, 388: 173-185.

Assumpção, M., Azevedo, P.A., Rocha, M.P., Bianchi, M.B. 2017. Lithospheric Features of the São Francisco Craton. In: Heilbron, M., Cordani, U.G., Alkmim, F.F. (Eds.). São Francisco Craton, Eastern Brazil: Tectonic Genealogy of a Miniature Continent. Springer International. 15-25 p.

Barbosa, J.S.F., Barbosa, R.G. 2017. The Paleoproterozoic Eastern Bahia Orogenic Domain. In: Heilbron, M., Cordani, U.G., Alkmim, F.F. (Eds.). São Francisco Craton, Eastern Brazil: Tectonic Genealogy of a Miniature Continent. Springer International. 57-69 p.

Barbosa, J.S.F., Cruz, S.C.P., Souza, J.S. 2012. Terrenos metamórficos do embasamento. In: Barbosa, J.S.F. (Ed.). Geologia da Bahia; pesquisa e atualização. Volume 1. CBMP-Companhia Baiana de Pesquisa Mineral. Salvador, Bahia. 101-201 p.

Barbosa, J.S.F., Sabaté, P. 2004. Archean and Paleoproterozoic crust of the São Francisco Craton, Bahia, Brazil: geodynamic features. Precambrian Research, 133: 1-27.

Barker, F., Arth, J.G. 1976. Generation of trondhjemitic-tonalitic liquids and Archean bimodal trondhjemite-basalt suites. Geology, 4(10): 596-600.

Barton, M.D. 1990. Cretaceous magmatism, metamorphism, and metallogeny in the east-central Great Basin. In: Anderson, J.L. (Ed.). The nature and origin of cordilleran magmatism, GSA Memoirs, 174: 283-302.

Batchelor, R.A., Bowden, P. 1985. Petrogenetic interpretation of granitoid rock series using multicationic parameters. Chemical Geology, 48: 43-55.

Berrocal, J., Marangoni, Y., Sá, N.C.D., Fuck, R.A., Soares, J.E.P., Dantas, E., Perosi, F., Fernandes, C. 2004. Deep seismic refraction and gravity crustal model and tectonic deformation in Tocantins Province, Central Brazil. Tectonophysics, 388: 187-199.

Beyssac, O., Goffé, B., Chopin, C., Rouzaud, J.N. 2002. Raman spectra of carbonaceous material in metasediments: a new geothermometer. Journal of Metamorphic Geology, 20: 859-871.

Bhatia, M.R. 1983. Plate tectonics and geochemical composition of sandstones. Journal of Geology, 91(6): 611-627.

Bhatia, M.R., Crook, K.A.W. 1986. Trace element characteristics of graywackes and tectonic setting discrimination of sedimentary basins. Contributions to Mineralogy and Petrology, 92: 181-193.

Bogossian, J. 2012. Mineralizações primárias e supergênicas de urânio do nordeste de Goiás e sudeste de Tocantins: contexto geológico, mineralogia e implicações metalogenéticas. Dissertação de mestrado. Universidade de Brasília. 54 p.

Bond, G.C., Christie-Blick, N., Kominz, M.A., Devlin, W.J. 1985. An early Cambrian rift to post-rift transition in the Cordillera of western North America. Nature, 315: 742-746.

Botelho, N.F. 1992. Les ensembles granitiques subalcalins a peralumineux mineralises en Sn et In de la Sous-Province Paranã, etat de Goiás, Bresil. PhD. Thesis. Université Pierre et Marie Curie (Paris VI). 344 p.

Botelho, N.F., Alvarenga, C.J.S., Menezes, P.R., D'El-Rey-Silva, L.J.H. 1999. Suíte Aurumina: uma suíte de granitos Paleoproterozóicos, peraluminosos e sin-tectônicos na faixa Brasília. VII Simpósio de Geologia do Centro-Oeste e X Simpósio de Geologia de Minas Gerais, Brasília. Abstract volume. p. 17.

Botelho, N.F., Fuck, R.A., Dantas, E.L., Laux, J.H., Junges, S.L. 2006a. The Paleoproterozoic peraluminous Aurumina granite suite, Goiás and Tocantins, Brazil: geological, whole rock geochemistry and U-Pb and Sm-Nd isotopic constraints. In: Alkmim, F.F., Noce, C.M. (Eds.). The Paleoproterozoic record of the São Francisco Craton, Brazil. Field guide and abstracts. IGCP509: Paleoproterozoic Supercontinents & Global Evolution. p. 92.

Botelho, N.F., Moura, M.A., Alvarenga, C.J.S., Dantas, E.L., Dardenne, M.A., Campos, J.E.G., Menezes, P.R., Pereira, A.B. 2002. Granitogênese peraluminosa transamazônica no embassamento da Faixa Brasília e seu significado tectônico. XLI Congresso Brasileiro de Geologia, João Pessoa. Abstract volume. p. 436.

Botelho, N.F., Moura, M.A., Peterson, R.C., Stanley, C.J., Silva, V.G. 2006b. Kalungaite, PdAsSe, a new platinum-group mineral from the Buraco do Ouro goldmine, Cavalcante, Goiás State, Brazil. Mineralogical Magazine, 70(1): 123-130.

Brandon, A.D., Lambert, R.S.J. 1994. Crustal melting in the cordilleran interior: the mid-Cretaceous White Creek Batholith in the southern Canadian Cordillera. Journal of Petrology, 35(1): 239-269.

Brown, M. 2013. Granite: From genesis to emplacement. GSA Bulletin, 125(7/8): 1079-1113.

Brown, M., Rushmer, T. 2005. Introduction. In: Brown, M., Rushmer, T (Eds.). Evolution and differentiation of the continental crust. Cambridge University Press. p. 1-20.

Bühn, B., Pimentel, M.M., Matteini, M., Dantas, E.L. 2009. High spatial resolution analysis of Pb and U isotopes for geochronology by laser ablation multi-collector inductively coupled plasma mass spectrometry (LA-MC-ICP-MS). Anais da Academia Brasileira de Ciências, 81(1): 99-114.

Cadusch, P.J., Hlaing, M.M., Wade, S.A., McArthur, S.L., Stoddart, P.R. 2013. Improved methods for fluorescence background subtraction from Raman spectra. Journal of Raman Spectroscopy, 44: 1587-1595.

Champion, D.C., Bultitude, R.J. 2013. The geochemical and Sr-Nd isotopic characteristics of Paleozoic fractionated S-types granites of north Queensland: implications for S-type granite petrogenesis. Lithos, 162-163: 37-56.

Chappell, B.W., Bryant, C.J., Wyborn, D. 2012. Peraluminous I-type granites. Lithos, 153: 142-153.

Chappell, B.W., White, A.J.R. 1992. I- and S-type granites in the Lachlan Fold Belt. Transactions of the Royal Society of Edinburgh: Earth Sciences, 83: 1-26.

Chappell, B.W., White, A.J.R. 2001. Two contrasting granite types: 25 years later. Australian Journal of Earth Sciences, 48: 489-499.

Chappell, B.W., White, A.J.R., Williams, I.S., Wyborn, D., Wyborn, L.A.I. 2000. Lachlan Fold Belt granites revisited: high- and low-temperature granites and their implications. Australian Journal of Earth Sciences, 47: 123-138.

Chemale Jr., F., Dussin, I.A., Alkmim, F.F., Martins, M.S., Queiroga, G., Armstrong, R., Santos, M.N. 2012. Unravelling a Proterozoic basin history through detrital zircon geochronology: The case of the Espinhaço Supergroup, Minas Gerais, Brazil. Gondwana Research, 22: 200-206.

Clemens, J.D. 2003. S-type granitic magmas—petrogenetic issues, models and evidence. Earth Science Reviews, 61(1-2): 1-18.

Clemens, J.D., Wall, V.J. 1981. Origin and crystallization of some peraluminous (S-type) granitic magmas. Canadian Mineralogist, 19: 111-131.

Collins, W.J., Richards, S.W. 2008. Geodynamic significance of S-type granites in circum-Pacific orogens. Geology, 36(7): 559-562.

Coney, P.J., Harms, T.A. 1984. Cordilleran metamorphic core complexes: Cenozoic extensional relics of Mesozoic compression. Geology, 12: 550-554.

Cordeiro, P.F.O., Oliveira, C.G., Giustina, M.E.S.D., Dantas, E.L., Santos, R.V. 2014. The Paleoproterozoic Campinorte Arc: tectonic evolution of a Central Brazil pre-Columbia orogeny. Precambrian Research, 251: 49-61.

Corfu, F., Hanchar, J.M., Hoskin, P.W.O., Kinny, P. 2003. Atlas of zircon textures. In: Hanchar, J.M., Hoskin, P.W.O. (Eds.). Zircon. Reviews in Mineralogy and Geochemistry, 53: 469–500.

Corrêa, R.S., Oliveira, C.G., Vidotti, R.M., Souza, V.S. 2015. Regional-scale pressure shadow-controlled mineralization in the Príncipe Orogenic Gold Deposit, Central Brazil. Ore Geology Reviews, 71: 273-304.

Costa, J.B.S. 1985. Aspectos lito-estruturais e evolução crustal da região centro-oeste de Goiás. Ph.D. Thesis. Universidade Federal do Pará. 210 p.

CPRM (Brazilian Geological Survey). 2014. Dianópolis geological chart SC.23-Y-C. Scale 1:250.000 (preliminar). http://geobank.cprm.gov.br/.

Cruz, E.L.C.C. 2001. A gênese e o contexto tectônico da mina Córrego Paiol, terreno Almas-Conceição: Um depósito de ouro hospedado em anfibolito do embasamento da Faixa de Dobramentos Brasília. Ph.D. Thesis. University of Brasília, Brazil. 183 p.

Cruz, E.L.C.C., Kuyumjian, R.M. 1996. Chemical characterization of metabasalts and granitoids from the Almas-Dianópolis granite-greenstone terrane, Central Brazil.

In: Symposium on Archaean Terranes of the South American Platform, Brasília. Extended abstracts: 53-54.

Cruz, E.L.C.C., Kuyumjian, R.M. 1998. The geology and tectonic evolution of the Tocantins granite-greenstone terrane: Almas-Dianópolis region, Tocantins state, central Brazil. Revista Brasileira de Geociências, 28(2): 173-182.

Cruz, E.L.C.C., Kuyumjian, R.M., Boaventura, G.R. 2003. Low-K calc-alkaline granitic series of southeastern Tocantins state: chemical evidence for two sources for the granite-gneissic complexes in the Paleoproterozoic Almas-Dianópolis Terrane. Revista Brasileira de Geociências, 33(2): 125-136.

Cumberland, S.A., Douglas, G., Grice, K., Moreau, J.W. 2016. Uranium mobility in organic matter-rich sediments: A review of geological and geochemical processes. Earth-Science Reviews, 159: 160-185.

Cunha, L.M. 2006. Gênese e controle da mineralização de Au e Ag associada a granitos peraluminosos na mina de Aurumina, Goiás. Dissertação de mestrado. Universidade de Brasília. 119 p.

d'Arco, P., Maury, R.C., Westercamp, D. 1981. Geothermometry and geobarometry of a cummingtonite-bearing dacite from Martinique, Lesser Antilles. Contributions to Mineralogy and Petrology, 77: 177-184.

Dardenne, M.A. 2000. The Brasilia Fold Belt. In: Cordani, U.G., Milani, E.J., Thomaz-Filho, A., Campos, D.A. (Eds.). Tectonic evolution of South America. 31th International Geological Congress, Rio de Janeiro. pp. 231-263.

Dardenne M. A., Botelho N. F. 2014. Metalogênese da zona externa da Faixa Brasília. In: Silva M.G., Rocha Neto M.B., Jost H., Kuyumjian R.M. (Eds.). Metalogênese das Províncias Tectônicas Brasileiras, CPRM/Brazilian Geological Survey. 431-454 p.

Debon, F., Le Fort, P. 1982. A chemical-mineralogical classification of common plutonic rocks and associations. Transactions of the Royal Society of Edinburgh, Earth Sciences, (73): 135-149.

De Capitani, L., Liborio, G., Schiavinato, G. 1990. Cummingtonite nelle plutoniti della Val Biandino (Como). Rendiconti Lincei, 1(4): 379-385.

Deer, W.A. 1935. The Cairnsmore of Carsphairn Igneous Complex. Quarterly Journal of the Geological Society, 91: 47-76.

Deniel, C., Vidal, P., Fernández, A., Le Fort, P., Peucat, J.J. 1987. Isotopic study of the Manaslu granite (Himalaya, Nepal): inferences on the age and source of Himalayan leucogranites. Contributions to Mineralogy and Petrology, 96: 78-92.

DePaolo, D.J. 1981. A neodymium and strontium isotopic study of the Mesozoic calc-alkaline granitic batholiths of the Sierra Nevada and Peninsular Ranges, California. Journal of Geophysical Research, 86(B11): 10470-10488.

Driver, L.A., Creaser, R.A., Chacko, T., Erdmer, P. 2000. Petrogenesis of the Cretaceous Cassiar Batholith, Yukon–British Columbia, Canada: Implications for magmatism in the North American Cordilleran Interior. GSA Bulletin, 112(7): 1119-1133.

Elison, M.W. 1995. Causes and consequences of Jurassic magmatism in the northern Great Basin: Implications for tectonic development. In: Miller, D.M., Busby, C. (Eds.). Jurassic Magmatism and Tectonics of the North American Cordillera. GSA Special Paper, 299: 249-265.

Evans, B.W., Ghiorso, M.S. 1995. Thermodynamics and petrology of cummingtonite. American Mineralogist, 80: 649-663.

Evensen, N.M., Hamilton, P.J., O'Nions, R.K. 1978. Rare-earth abundances in chondritic meteorites. Geochimica et Cosmochimica Acta, 42: 1199–1212.

Fernandes, P.E.C.A., Montes, M.L., Braz, E.R.C., Montes, A.S.L., Silva, L.L., Oliveira, F.L.L., Ghignone, J.I., Siga Jr., O., Castro, H.E.F. 1982. I – Geologia. In: Ministério das Minas e Energia (Ed.). Projeto RADAMBRASIL, levantamento de recursos naturais, V. 29, Folha SD.23: Brasília. pp. 25-204.

Filgueiras, B.C. 2015. Depósito vulcanogênico polimetálico (Zn, Pb, Cu ±[Ag-Bi]) Artulândia, arco magmático Paleoproterozoico Campinorte, Brasil central. M.Sc. Dissertation. Universidade de Brasília. 101 p.

Fischel, D.P., Pimentel, M.M., Fuck, R.A., Armstrong, R. 2001. U-Pb SHRIMP and Sm-Nd geochronology of the Silvânia Volcanics and Jurubatuba Granite: juvenile Paleoproterozoic crust in the basement of the Neoproterozoic Brasília Belt, Goiás, central Brazil. Anais da Academia Brasileira de Ciências, 73(3): 445-460.

Floyd, P.A., Shail, R., Leveridge, B.E., Franke, W. 1991. Geochemistry and provenance of Rhenohercynian synorogenic sandstones: implications for tectonic environment discrimination. In: Morton, A.C., Todd, S.P., Haughton, P.D.W. (Eds.). Developments in sedimentary provenance studies. Geological Society Special Publication, 57: 173-188.

Floyd, P.A., Winchester, J.A., Park, R.G. 1989. Geochemistry and tectonic setting of Lewisian clastic metasediments from the Early Proterozoic Loch Maree Group of Gairloch, NW Scotland. Precambrian Research, 45: 203-214.

Frost, B.R., Frost, C.D. 2008. A geochemical classification for feldspathic igneous rocks. Journal of Petrology, 49(11): 1955-1969.

Fuck, R.A., Dantas, E.L., Pimentel, M.M., Botelho, N.F., Armstrong, R., Laux, J.H., Junges, S.L., Soares, J.E., Praxedes, I.F. 2014. Paleoproterozoic crust-formation and reworking events in the Tocantins Province, central Brazil: A contribution for Atlantica supercontinent reconstruction. Precambrian Research, 244: 53–74.

Fuck, R.A., Pimentel, M.M., Alvarenga, C.J.S., Dantas, E.L. 2017. The Northern Brasília Belt. In: Heilbron, M., Cordani, U.G., Alkmim, F.F. (Eds.). São Francisco Craton,

Eastern Brazil: Tectonic Genealogy of a Miniature Continent. Springer International. 205-220 p.

Fuck, R.A., Pimentel, M.M., D'El-Rey-Silva, L.J.H. 1994. Compartimentação tectônica na porção oriental da Província Tocantins. 38° Congresso Brasileiro de Geologia, Balneário Camboriú, SC. Abstract volume, Vol. 1: 215-216.

Geschwind, C.H., Rutherford, M.J. 1992. Cummingtonite and the evolution of the Mount St. Helens (Washington) magma system: An experimental study. Geology, 20: 1011-1014.

Gioia, S.M.C.L., Pimentel, M.M. 2000. The Sm-Nd Isotopic Method in the Geochronology Laboratory of the University of Brasília. Anais da Academia Brasileira de Ciências, 72(2): 219-245.

Giustina, M.E.S.D., De Oliveira, C.G., Pimentel, M.M., De Melo, L.V., Fuck, R.A., Dantas, E.L., Bühn, B. 2009. U–Pb and Sm–Nd constraints on the nature of the Campinorte sequence and related Palaeoproterozoic juvenile orthogneisses, Tocantins Province, central Brazil. In: Reddy, S.M., Mazumder, R., Evans, D.A.D., Collins, A.S. (Eds.). Palaeoproterozoic Supercontinents and Global Evolution. Geological Society, London, Special Publications, 323: 255–269.

Guo, Z., Wilson, M. 2012. The Himalayan leucogranites: constraints on the nature of their crustal source region and geodynamic setting. Gondwana Research, 22: 360-376.

Harris, N., Massey, J. 1994. Decompression and anatexis of Himalayan metapelites. Tectonics, 13(6): 1537-1546.

Hayashi, K.I., Fujisawa, H., Holland, H.D., Ohmoto, H. 1997. Geochemistry of ~1.9 Ga sedimentary rocks from northeastern Labrador, Canada. Geochimica et Cosmochimica Acta, 61(19): 4115-4137.

Herron, M.M. 1988. Geochemical classification of terrigenous sands and shales from core or log data. Journal of sedimentary petrology, 58(5): 820-829.

Holtz, F., Johannes, W., Pichavant, M. 1992. Peraluminous granites: the effect of alumina on melt composition and coexisting minerals. Transactions of the Royal Society of Edinburgh: Earth Sciences, 83: 409-416.

Hyndman, D.W. 1983. The Idaho batholith and associated plutons, Idaho and Western Montana. In: Roddick, J.A. (Ed.). Circum-Pacific Plutonic Terranes. GSA Memoirs, 159: 213-240.

Hyndman, D.W., Foster, D.A. 1988. The role of tonalites and mafic dikes in the generation of the Idaho Batholith. Journal of Geology, 96: 31-46.

Irvine, T.N., Baragar, W.R.A. 1971. A Guide to the chemical classification of the common volcanic rocks. Canadian Journal of Earth Sciences, 8(5): 523-548.

Jackson, S.E., Pearson, N.J., Griffin, W.L., Belousova, E.A. 2004. The application of laser ablation inductively coupled plasma mass spectrometry to in situ U-Pb zircon geochronology. Chemical Geology, (211): 47–69.

Jacobsen, S.B., Wasserburg, G.J. 1980. Sm-Nd isotopic evolution of chondrites. Earth and Planetary Science Letters, (50): 139-155.

Jacobsen, S.B., Wasserburg, G.J. 1984. Sm-Nd isotopic evolution of chondrites and achondrites, II. Earth and Planetary Science Letters, (67): 137-150.

Kapp, J.D.A., Miller, C.F., Miller, J.S. 2002. Ireteba Pluton, El dorado Mountains, Nevada: Late, Deep-Source, Peraluminous Magmatism in the Cordilleran Interior. Journal of Geology, 110: 649-669.

Köksal, S., Göncüoğlu, M.C. 2008. Sr and Nd isotopic characteristics of some S-, I- and A-type granitoids from central Anatolia. Turkish Journal of Earth Sciences, 17: 111-127.

Laux, J.H., Pimentel, M.M., Dantas, E.L., Armstrong, R., Junges, S.L. 2005. Two Neoproterozoic crustal accretion events in the Brasília belt, central Brazil. Journal of South American Earth Sciences, 18: 183–198.

Ledru, P., Corcherie, A., Barbosa, J., Johan, V., Onstott, T. 1994. Ages du métamorphisme granulitique dans le craton du São Francisco (Brésil). Implications sur la nature de l'orogène transamazonien. Comptes Rendus de l'Académie des sciences, Paris, 318(II): 251-257 p.

Lee, S.Y., Barnes, C.G., Snoke, A.W., Howard, K.A., Frost, C.D. 2003. Petrogenesis of Mesozoic, peraluminous granites in the Lamoille Canyon area, Ruby Mountains, Nevada, U.S.A. Journal of Petrology, 44(4): 713-732.

Le Fort, P. 1981. Manaslu leucogranite: a collision signature of the Himalaya. A model for its genesis and emplacement. Journal of Geophysical Research, 86(B11): 10545-10568.

Le Fort, P., Cuney, M., Deniel, C., France-Lanord, C., Sheppard, S.M.F., Upreti, B.N., Vidal, P. 1987. Crustal generation of the Himalayan leucogranites. Tectonophysics, 134: 39-57.

Leventhal, J.A., Reid, M.R., Montana, A., Holden, P. 1995. Mesozoic invasion of crust by MORB-source asthenospheric magmas, U.S. Cordilleran interior. Geology, 23(5): 399-402.

Littke, R. 1993. Deposition, diagenesis and weathering of organic matter-rich sediments. Lecture notes in earth sciences, 47. Springer-Verlag Berlin Heidelberg. 218 p.

Ludwig, K.R. 2012. Isoplot. A Geochronological Toolkit for Microsoft Excel. Ver. 3.75. Berkeley Geochronology Center.

Lugmair, G.W., Marti, K. 1978. Lunar initial $^{143}Nd/^{144}Nd$: Differential evolution of the lunar crust and mantle. Earth Planetary Science Letters, (39): 349-357.

Maniar, P.D., Piccoli, P.M. 1989. Tectonic discrimination of granitoids. GSA Bulletin, (101): 635-643.

Marini, O.J., Botelho, N.F. 1986. A província de granitos estaníferos de Goiás. Revista Brasileira de Geociências, 16(1): 119-131.

Marini, O.J., Fuck, R.A., Danni, J.C.M., Dardenne, M.A., Loguercio, S.O.C., Ramalho, R. 1984a. As faixas de dobramentos Brasília, Uruaçu e Paraguai-Araguaia e o Maciço Mediano de Goiás. In: Schobbenhaus, C., Campos, D.A., Derze, G.R., Asmus, H.E. (Eds.). Geologia do Brasil. DNPM. Brazil. pp. 251-303.

Marini, O.J., Fuck, R.A., Dardenne, M.A., Danni, J.C.M. 1984b. Província Tocantins: setores central e sudeste. In: Almeida, F.F.M., Hasui, Y. (Eds.). O Pré-Cambriano do Brasil. Edgard Blücher Ltd. pp. 205-264.

Marini, O.J., Liberal, G.S., Dos Reis, L.T., Trinidade, C.A.H., De Souza, S.L. 1978. Nova unidade litoestratigráfica do Pré-Cambriano do estado de Goiás. XXX Congresso Brasileiro de Geologia, Recife. Boletim N°1, Resumos das Comunicações. pp. 126-127.

McCulloch, M.T., Chappell, B.W. 1982. Nd isotopic characteristics of S- and I-type granites. Earth and Planetary Science Letters, 58(1): 51-64.

McLennan, S.M., Hemming, S., McDaniel, D.K., Hanson, G.N. 1993. Geochemical approaches to sedimentation, provenance, and tectonics. In: Johnsson, M.J., Basu, A. (Eds.). Processes controlling the composition of clastic sediments. Geological Society of America, Special Paper 284: 21-40.

Melezhik, V.A., Fallick, A.E. 1996. A widespread positive $\delta^{13}C_{carb}$ anomaly at around 2.33-2.06 Ga on the Fennoscandian Shield: a paradox? Terra Nova, 8: 141-157.

Melezhik, V.A., Fallick, A.E. 1997. A widespread positive $\delta^{13}C_{carb}$ anomaly at around 2.33-2.06 Ga on the Fennoscandian Shield - comment and reply. Terra Nova, 9(3): 148-151.

Melezhik, V.A., Fallick, A.E., Martin, A.P., Condon, D.J., Kump, L.R., Brasier, A.T., Salminen, P.E. 2013. The Palaeoproterozoic Perturbation of the Global Carbon Cycle: The Lomagundi-Jatuli Isotopic Event. In: Melezhik, V.A., Prave, A.R., Hanski, E.J., Fallick, A.E., Lepland, A., Kump, L.R., Strauss, H. (Eds.). Reading the Archive of Earth's Oxygenation, volume 3: Global Events and the Fennoscandian Arctic Russia - Drilling Early Earth Project. Springer-Verlag Berlin Heidelberg. 1111-1150 p.

Melezhik, V.A., Fallick, A.E., Medvedev, P.V., Makarikhin, V.V. 1999. Extreme $\delta^{13}C_{carb}$ enrichment in ca. 2.0 Ga magnesite–stromatolite–dolomite–'red beds' association in a global context: a case for the world-wide signal enhanced by a local environment. Earth-Science Reviews, 48: 71-120.

Menez, J., Botelho, N.F. 2016. Ore characterization and textural relationships among gold, selenides, platinum group minerals, and uraninite at the granite-related Buraco do Ouro gold mine, Cavalcante, Central Brazil. Mineralogical Magazine, in press: http://www.ingentaconnect.com/content/minsoc/mag/pre-prints/content-minmag-1156.

Miller, C.F., Barton, M.D. 1990. Phanerozoic plutonism in the Cordilleran Interior, U.S.A. In: Kay, S.M., Rapela, C.W. (Eds.). Plutonism from Antarctica to Alaska. GSA Special Paper 241, 213-231.

Miller, C.F., Barton, M.D., Miller, J., Kapp, J., Loflin, M. 2003. Peraluminous granites of the cordilleran interior, western U.S.A.: hybrid magmas from deep, ancient crust. GSA Abstracts with Programs, 35(4): p. 18.

Miller, C.F., Bradfish, L.J. 1980. An inner Cordilleran belt of muscovite-bearing plutons. Geology, 8: 412-416.

Miller, C.F., Wooden, J.L., Bennett, V.C., Wright, J.E., Solomon, G.C., Hurst, R.W. 1990. Petrogenesis of the composite peraluminous-metaluminous Old Woman-Piute Range Batholith, southeastern California: isotopic constraints. In: Anderson, J.L. (Ed.). The nature and origin of cordilleran magmatism, GSA Memoirs, 174: 99-109.

Nábělek, P.I., Liu, M. 2004. Petrologic and thermal constraints on the origin of leucogranites in collisional orogens. Transactions of the Royal Society of Edinburgh: Earth Sciences, 95: 73–85.

Nockolds, S.R. 1940. The Garabal Hill-Glen Fyne Igneous Complex. Quarterly Journal of the Geological Society, 96: 451-511.

Oliveira, C.G., Oliveira, F.B., Dantas, E.L., Fuck, R.A. 2007. Campinorte - SD.22-Z-B-I, escala 1:100.000: nota explicativa. UnB-CPRM, Brazil. 68 p.

Pallister, J.S., Hoblitt, R.P., Meeker, G.P., Knight, R.J., Siems, D.F. 1996. Magma mixing at Mount Pinatubo: petrographic and chemical evidence from the 1991 Deposits. In: Newhall, C.G., Punongbayan, R.S. (Eds.). Fire and mud: eruptions and lahars of Mount Pinatubo, Philippines. University of Washington Press. 1126 p.

Patiño-Douce, A.E. 1995. Experimental generation of hybrid silicic melts by reaction of high-Al basalt with metamorphic rocks. Journal of Geophysical Research, 100(B8): 15,623-15,639.

Patiño-Douce, A.E. 1999. What do experiments tell us about the relative contributions of crust and mantle to the origin of granitic magmas? In: Castro, A., Fernández, C., Vigneresse, J.L. (Eds.). Understanding Granites: Integrating New and Classical Techniques. Geological Society of London, Special Publications, 168: 55-75.

Patiño-Douce, A.E., Beard, J.S. 1996. Effects of P, $f(O_2)$ and Mg/Fe Ratio on Dehydration Melting of Model Metagraywackes. Journal of Petrology, 37(5): 999-1024.

Patiño-Douce, A.E., Humphreys, E.D., Johnston, A.D. 1990. Anatexis and metamorphism in tectonically thickened continental crust exemplified by the Sevier hinterland, western North America. Earth and Planetary Science Letters, 97: 290-315.

Patiño-Douce, A.E., Johnston, A.D. 1991. Phase equilibria and melt productivity in the pelitic system: implications for the origin of peraluminous granitoids and aluminous granulites. Contributions to Mineralogy and Petrology, 107: 202-218.

Paul, A., Jung, S., Romer, R.L., Stracke, A., Hauff, F. 2014. Petrogenesis of synorogenic high-temperature leucogranites (Damara orogen, Namibia): constraints from U–Pb monazite ages and Nd, Sr and Pb isotopes. Gondwana Research, 25: 1614-1626.

Pearce, J.A., Harris, N.B.W., Tindle, A.G. 1984. Trace element discrimination diagrams for the tectonic interpretation of granitic rocks. Journal of Petrology, 25(4): 956-983.

Pereira, A.B. 2001. Caracterização dos granitos e pegmatitos peraluminosos mineralizados em Sn-Ta de Monte Alegre de Goias. M.Sc. Thesis. Universidade de Brasília. 78 p.

Pietranik, A. 2003. Constraints on cummingtonite crystallization in the Gęsiniec Intrusive (Strzelin Crystalline Massif, Fore Sudetic Block, SW Poland). Journal of the Czech Geological Society, 48: 1-2.

Pimentel, M.M., Fuck, R.A. 1992. Neoproterozoic crustal accretion in central Brazil. Geology, 20: 375-379.

Pimentel, M.M., Fuck, R.A., Botelho, N.F. 1999. Granites and the geodynamic history of the neoproterozoic Brasília belt, Central Brazil: a review. Lithos, 46: 463-483.

Pimentel, M.M., Fuck, R.A., Gioia, S.M.C.L. 2000. The Neoproterozoic Goiás Magmatic Arc, Central Brazil: a review and new Sm-Nd isotopic data. Revista Brasileira de Geociências, 30(1): 35-39.

Pimentel, M.M., Heaman, L., Fuck, R.A., Marini, O.J. 1991. U-Pb zircon geochronology of Precambrian tin-bearing continental-type acid magmatism in central Brazil. Precambrian Research, 52: 321-335.

Pimentel, M.M., Jost, H., Fuck, R.A. 2004. O embasamento da Faixa Brasília e o Arco Magmático de Goiás. In: Mantesso-Neto, V., Bartorelli, A., Carneiro, C.D.R., Brito-Neves, B.B. (Eds.). Geologia do continente Sul-Americano: evolução da obra de Fernando Flávio Marques de Almeida. Ed. Beca. pp. 355-368.

Rapp, R.P., Shimizu, N., Norman, M.D. 2003. Growth of early continental crust by partial melting of eclogite. Nature, 425: 605-609.

Rapp, R.P., Watson, E.B. 1995. Dehydration melting of metabasalt at 8-32 kbar: implications for continental growth and crust-mantle recycling. Journal of Petrology, 36(4): 891-931.

Rapp, R.P., Watson, E.B., Miller, C.F. 1991. Partial melting of amphibolite/eclogite and the origin of Archean trondhjemites and tonalites. Precambrian Research, 51: 1-25.

Roser, B.P., Korsch, R.J. 1986. Determination of tectonic setting of sandstone-mudstone suites using SiO_2 content and K_2O/Na_2O ratio. Journal of Geology, 94(5): 635-650.

Rushmer, T. 1991. Partial melting of two amphibolites: contrasting experimental results under fluid-absent conditions. Contributions to Mineralogy and Petrology, 107: 41-59.

Rutherford, M.J., Devine, J.D. 1996. Preeruption pressure-temperature conditions and volatiles in the 1991 dacitic magma of Mount Pinatubo. In: Newhall, C.G., Punongbayan, R.S. (Eds.). Fire and mud: eruptions and lahars of Mount Pinatubo, Philippines. University of Washington Press. 1126 p.

Saboia, A.M. 2009. O vulcanismo em Monte do Carmo e litoestratigrafia do Grupo Natividade, estado de Tocantins. M.Sc. Thesis. Universidade de Brasília. 76 p.

Santos, M.N., Chemale Jr., F., Dussin, I.A., Martins, M., Assis, T.A.R., Jelinek, A.R., Guadagnin, F., Armstrong, R. 2013. Sedimentological and paleoenvironmental constraints of the Statherian and Stenian Espinhaço rift system, Brazil. Sedimentary Geology, 290: 47-59.

Searle, M.P. 2013. Crustal melting, ductile flow, and deformation in mountain belts: Cause and effect relationships. Lithosphere, 5(6): 547-554.

Searle, M.P., Cottle, J.M., Streule, M.J., Waters, D.J. 2009. Crustal melt granites and migmatites along the Himalaya: melt source, segregation, transport and granite emplacement mechanisms. Transactions of the Royal Society of Edinburgh: Earth Sciences, 100: 219-233.

Sevigny, J.H., Parrish, R.R., Ghent, E.D. 1989. Petrogenesis of peraluminous granites, Monashee Mountains, Southeastern Canadian Cordillera. Journal of Petrology, 30(3): 557-581.

Sial, A.N., Dardenne, M.A., Misi, A., Pedreira, A.J., Gaucher, C., Ferreira, V.P., Silva Filho, M.A., Uhlein, A., Pedrosa-Soares, A.C., Santos, R.V., Egydio-Silva, M., Babinski, M., Alvarenga, C.J.S., Fairchild,T.R., Pimentel, M.M. 2009. The São Francisco Palaeocontinent. In: Gaucher, C., Sial, A.N., Halverson, G.P., Frimmel, H.E. (Eds.). Neoproterozoic-Cambrian Tectonics, Global Change and Evolution: a focus on southwestern Gondwana. Developments in Precambrian Geology, 16: 31-69.

Soares, J.E., Berrocal, J., Fuck, R.A., Mooney, W.D., Ventura, D.B.R. 2006. Seismic characteristics of central Brazil crust and upper mantle: A deep seismic refraction study. Journal of Geophysical Research, 111 (B12302). 31 p.

Sousa, I.M.C., Giustina, M.E.S.D., Oliveira, C.G. 2016. Crustal evolution of the northern Brasília Belt basement, central Brazil: A Rhyacian orogeny coeval with a pre-Rodinia supercontinent assembly. Precambrian Research, 273: 129-150.

Sparrenberger, I., Tassinari, C.C.G. 1999. Subprovíncia do rio Paranã (GO): um exemplo de aplicação dos métodos de datação U-Pb e Pb-Pb em cassiterita. Revista Brasileira de Geociências, 29(3): 405-414.

Spirakis, C.S. 1996. The roles of organic matter in the formation of uranium deposits in sedimentary rocks. Ore Geology Reviews, 11: 53-69.

Stewart, F.H. 1946. The gabbroic complex of Belhelvie in Aberdeenshire. Quarterly Journal of the Geological Society, 102: 465-498.

Stewart, J.H. 1972. Initial deposits in the cordilleran geosyncline: evidence of a Late Precambrian (<850 m.y.) continental separation. GSA Bulletin, 83: 1345-1360.

Stewart, J.H. 1976. Late Precambrian evolution of North America: Plate tectonics implication. Geology, 4(1): 11-15.

Strieder, A.J., Suita, M.T.F. 1999. Neoproterozoic geotectonic evolution of Tocantins Structural Province, Central Brazil. Journal of Geodynamics, 28: 267-289.

Sun, S.S., McDonough, W.F. 1989. Chemical and isotopic systematics of oceanic basalts: implications for mantle composition and processes. In: Saunders, A.D., Norry, M.J. (Eds.). Magmatism in the ocean basins. Geological Society Special Publication, 42: 313–345.

Sylvester, P.J. 1998. Post-collisional strongly peraluminous granites. Lithos, 45: 29-44.

Takahashi, M., Aramaki, S., Ishihara, S. 1980. Magnetite-series/Ilmenite-series vs. I-type/S-type granitoids. Mining Geology Special Issue, 8: 13-28.

Teixeira, W., Figueiredo, M.C.H. 1991. An outline of Early Proterozoic crustal evolution in the São Francisco craton, Brazil: a review. Precambrian Research, 53: 1-22.

Teixeira, W., Oliveira, E.P., Marques L.S. 2017. Nature and evolution of the Archean crust of the São Francisco Craton. In: Heilbron, M., Cordani, U.G., Alkmim, F.F. (Eds.). São Francisco Craton, Eastern Brazil: Tectonic Genealogy of a Miniature Continent. Springer International. 29-56 p.

Tilling, R.I. 1973. Boulder Batholith, Montana: a product of two contemporaneous but chemically distinct magma series. GSA Bulletin, 84: 3879-3900.

Trompette, R.R., Uhlein, A., Silva, M.E., Karmann, I. 1992. O Cráton Brasiliano do São Francisco - uma revisão. Revista Brasileira de Geociências, 22(4): 481-486.

Valeriano, C.M., Pimentel, M.M., Heilbron, M., Almeida, J.C.H., Trouw, R.A.J. 2008. Tectonic evolution of the Brasília Belt, Central Brazil, and early assembly of

Gondwana. In: Pankhurst, R.J., Trouw, R.A.J., Brito-Neves, B.B., De Wit, M.J. (Eds.) West Gondwana: Pre-Cenozoic Correlations Across the South Atlantic Region. Geological Society, London, Special Publications, 294: 197-210.

Verma, S.P., Pandarinath, K., Verma, S.K., Agrawal, S. 2013. Fifteen new discriminant-function-based multi-dimensional robust diagrams for acid rocks and their application to Precambrian rocks. Lithos, 168-169: 113-123.

Verma, S.P., Rivera-Gómez, M.A. 2013. Computer programs for the classification and nomenclature of igneous rocks. Episodes, 36(2): 115-124.

Villaseca, C., Pérez-Soba, C., Merino, E., Orejana, D., López-García, J.A., Billstrom, K. 2008. Contrasting crustal sources for peraluminous granites of the segmented Montes de Toledo Batholith (Iberian Variscan Belt). Journal of Geosciences, 53: 263-280.

Wells, M.L., Hoisch, T.D. 2008. The role of mantle delamination in widespread Late Cretaceous extension and magmatism in the Cordilleran orogen, western United States. GSA Bulletin, 120(5/6): 515-530.

White, A.J.R., Chappell, B.W. 1977. Ultrametamorphism and granitoid genesis. Tectonophysics, 43: 7-22.

White, A.J.R., Clemens, J.D., Holloway, J.R., Silver, L.T., Chappell, B.W., Wall, V.J. 1986. S-type granites and their probable absence in southwestern North America. Geology, 14: 115-118.

Whittington, A.G., Treloar, P.J. 2002. Crustal anatexis and its relation to the exhumation of collisional orogenic belts, with particular reference to the Himalaya. Mineralogical Magazine, 66(1): 53-91.

Wiedenbeck, M., Allé, P., Corfu, F., Griffin, W.L., Meier, M., Oberli, F., Von Quadt, A., Roddick, J.C., Spiegel, W. 1995. Three natural zircon standards for U-Th-Pb, Lu-Hf, trace element and REE analyses. Geostandards Newsletter, 19(1): 1-23.

Wiedenbeck, M., Hanchar, J.M., Peck, W.H., Sylvester, P., Valley, J., Whitehouse, M., Kronz, A., Morishita, Y., Nasdala, L., Fiebig, J., Franchi, I., Girard, J.P., Greenwood, R.C., Hinton, R., Kita, N., Mason, P.R.D., Norman, M., Ogasawara, M., Piccoli, P.M., Rhede, D., Satoh, H., Schulz-Dobrick, B., Skår, Ø., Spicuzza, M.J., Terada, K., Tindle, A., Togashi, S., Vennemann, T., Xie, Q., Zheng, Y.F. 2004. Further characterisation of the 91500 zircon crystal. Geostandards and Geoanalytical Research, 28(1): 9-39.

Winther, K.T. 1996. An experimentally based model for the origin of tonalitic and trondhjemitic melts. Chemical Geology, 127: 43-59.

Wyllie, P.J., Wolf, M.B., van der Laan, S.R. 1997. Conditions for formation of tonalites and trondhjemites: magmatic sources and products. In: De Wit, M.J., Ashwal, L.D. (Eds.). Greenstone Belts. Oxford University Press. pp 256-266.

Yonkee, W.A., Weil, A.B. 2015. Tectonic evolution of the Sevier and Laramide belts within the North American Cordillera orogenic system. Earth-Science Reviews, 150: 531-593.